INVESTIGATING THE GRAPHENE-DIAMOND INTERFACE FOR ELECTRONIC, CHEMICAL AND BIOLOGICAL APPLICATIONS

LIM YI XUAN CANDY HALEY

NATIONAL UNIVERSITY OF SINGAPORE

2013

INVESTIGATING THE GRAPHENE-DIAMOND INTERFACE FOR ELECTRONIC, CHEMICAL AND BIOLOGICAL APPLICATIONS

LIM YI XUAN CANDY HALEY

B. Sc (Hons)

National University of Singapore

A THESIS SUBMITTED

FOR THE DEGREE OF DOCTOR OF PHILOSOPHY

NUS GRADUATE SCHOOL FOR INTEGRATIVE SCIENCES AND ENGINEERING

NATIONAL UNIVERSITY OF SINGAPORE

2013

Declaration

I hereby declare that this thesis is my original work and it has been written by me in its entirety. I have duly acknowledged all the sources of information which have been used in the thesis.

This thesis has also not been submitted for any degree in any university previously.

_____

Lim Yi Xuan Candy Haley

19th September 2013

Acknowledgements

This dissertation would not have been possible without the opportunity offered by NUS Graduate School for Integrative Sciences and Engineering (NGS) and the continuous support, encouragement and inspiration bestowed to me by the following people:

First and foremost, I would like to express my utmost gratitude to my principle supervisor, Professor Loh Kian Ping, who has always been an earnest motivator and mentor since I first attended his class as an undergraduate in NUS. After joining his research group to embark on the journey of research in 2008, I have discovered through him, what it takes to be a true scientist-one who constantly questions and seeks answers in order to satisfy his curiosity and hunger for knowledge. His deep interest, zest and passion for research are truly admirable and inspirational. His enthusiasm for research never fails to rub off me after every discussion we shared. Professor Loh has not only demonstrated to me what it takes to be a real scientist, but has also imparted to me essential life skills that will certainly come in useful in the next phase of my life.

My co-supervisor, Dr Chen Zhi-kuan from Institute of Materials and Engineering (IMRE) has been very helpful towards my work and is always ready for discussion. Dr Chen's positive outlook and approachable nature made him to be exceptionally popular with his students.

It has been an honor to be able to work with remarkable researchers, postdocs and Ph.D students from The Carbon Laboratory, Graphene Research

Centre and BioSystems and Micromechanics unit under the Singapore-MIT Alliance for Research & Technology (SMART). I would like to give special mentions to Dr. Zhong Yulin, Dr. Hoh Huiying, Mr Nai Chang Tai, Dr. Priscilla Ang, Dr. Lena Tang, Dr Goh Bee Min, Mr Jacky Lee, Dr. Bao Qiaoliang, Dr. Alison Tong, Dr. Lu Jiong, Dr. Zheng Yi and Dr. Wang Yu.

I am tremendously blessed to have parents who supported me through all times. My mum constantly showers me with steadfast love and tides me though the difficult periods of my life and sculpted me into who I am today. Yeo Wenwei has been my fantastic boyfriend since high school and has always been very accommodating to me. It has not been an easy task dating a workaholic girlfriend. Despite spending sleepless nights by my side when I wanted to complete my work, he did not utter a word of complaint. Life would not be the same without my best friend, Clarissa Chang. Her little acts of love and service over the past 14 years to me are priceless and irreplaceable.

List of Publications

1. **Lim, C. H. Y. X**., Nesladek, M. & Loh, K. P. Observing high pressure chemistry in graphene bubbles. *Angewande Chemie* (Under review)
2. **Lim, C. H. Y. X**., Sorkins, A., Bao, Q., Ang, L., Zhang, K., Nesladek, M. & Loh, K. P. A hydrothermal anvil made of graphene nanobubbles on diamond. *Nature Communications* (2013)
3. **Lim, C. H. Y. X**., Lee, W. C., Shi, H., Tang, L. A. L., Wang, Y., Lim, C. T. & Loh, K. P. Origin of enhanced stem cell growth and differentiation on graphene and graphene oxide. *ACS Nano* **5**, 7334-7341 (2011).
4. **Lim, C. H. Y. X.**, Zhong, Y. L., Janssens, S., Nesladek, M. & Loh, K. P. Oxygen-terminated nanocrystalline diamond film as an efficient anode in photovoltaics. *Advanced Functional Materials* **20**, 1313-1318 (2010).
5. Jaiswal, M., **Lim, C. H. Y. X.**, C. H., Bao, Q., Toh, C. T., Loh, K. P. & Özyilmaz, B. Controlled hydrogenation of graphene sheets and nanoribbons. *ACS Nano* **5**, 888-896 (2011).
6. Bao, Q., Zhang, H., Wang, B., Ni, Z., **Lim, C. H. Y. X.**, Wang, Y., Tang, D. Y. & Loh, K. P. Broadband graphene polarizer. *Nature Photonics* **5**, 411-415 (2011).
7. Ang, P. K., Jaiswal, M., **Lim, C. H. Y. X.**, Wang, Y., Sankaran, J., Li, A., Lim, C. T., Wohland, T., Barbaros, O. & Loh, K. P. A bioelectronic platform using a graphene-lipid bilayer interface. *ACS Nano* **4**, 7387-7394 (2010).

8. Steenackers, M., Gigler, A. M., Zhang, N., Deubel, F., Seifert, M., Hess, L. H., **Lim, C. H. Y. X.**, Loh, K. P., Garrido, J. A., Jordan, R., Stutzmann, M. & Sharp, I. D. Polymer brushes on graphene. *Journal of the American Chemical Society* **133**, 10490-10498 (2011).
9. Chen, X., Yang, J., **Lim, C. H. Y. X.**., Lu, J., Zhu, F. & Loh, K. P. Towards high efficiency solution processable inverted bulk heterojunction polymer solar cells using modified indium tin oxide cathode. *Organic Electronics: physics, materials, applications* **11**, 1942-1946 (2010).

Table of Contents

Chapter 3: Experimental Techniques

Chapter 4: Charge transfer properties of the graphene-diamond hybrid: Electrical charge transport and photovoltaic

Chapter 5: Binding of graphene and diamond for the formation of graphene nanobubbles as a hydrothermal anvil cell

Chapter 7: Diamond and graphene as biocompatible scaffolds for tissue engineering

Chapter 8: Conclusions

Summary

Although the phases of diamond and graphite are known to coexist in surface-graphitized nanodiamond particles or during the initial nucleation stage of diamond growth, there is no clear insight into how graphene interfaces with diamond both structurally and electronically. The metallic-sp^2 and dielectric-sp^3 interface offer the perfect environment for studying the complex interplay between electronic and lattice degrees of freedom for the creation of new functionalities. Motivated by the superlative properties of graphene and diamond, this thesis seeks to observe novel chemistry and physics by interfacing two different carbon phases.

Using surface spectroscopy and transport measurements, we evaluate the effect of substrate charge imputities on the mobility of CVD graphene. Diamond is investigated as a novel platform for graphene electronics due to its non-polar nature. By tuning the surface terminations of diamond, we evaluate the importance of substrate charge impurities in influencing the mobility of CVD graphene. To construct a hybrid diamond-graphene electrode, we coupled exfoliated graphene flakes to boron doped diamond (BDD) via molecular wire to enable efficient charge transfer. Electrical conductivity of the diamond electrode when coupled to graphene, can be improved with almost no or minimal compromise on its optical transparency as graphene absorbs *ca.* 2.3% of visible light.

Chemical hybridization of graphene and diamond (sp^2-sp^3 carbon carbon interface) by high temperature annealing was carried out to fuse graphene bubbles on diamond, such that strong interfacial bonding and

impermeability of graphene enables the construction of a hydrothermal graphene-diamond anvil cell. This work shows the first example of using an impermeable atomic membrane for trapping fluid at supercritical conditions, where the power of superheated water in corroding diamond is observed.

In addition, we observed high pressure (GPa)-induced conformational changes and cycloaddition reactions in the bench-top hydrothermal anvil cell constructed by trapping liquid medium trapped in graphene nanobubbles formed at the graphene-diamond interface. The nanobubbles that form as a result of thermally induced bonding between graphene and diamond at the interface are highly impermeable and function well as optically transparent, pressurized nanoreactors which allow high pressure chemical reactions to be probed with vibrational spectroscopy. By monitoring the conformational changes of pressure-sensitive molecules, the pressure within the nanobubbles could be tracked as a function of temperature and was found to be at ~ 1 GPa at 600 K. The polymerization of buckministerfullerene (C_{60}), which is symmetrically forbidden under ambient conditions, was observed to proceed in well-defined states in the pressurized nanobuble.

Finally, owing to the biocompatibility of these carbon materials, they were also explored as biomimetic platforms for cell growth. We have demonstrated the potential of using diamond, graphene and its derivatives as supporting platforms for enhanced growth and differentiation of human mesenchymal stem cells. The ability of these carbon based materials to accelerate stem cell growth and differentiation should find diverse applications in tissue engineering and regenerative medicine.

List of Tables

List of Figures

Figure 2.1 Equilibrium structure of graphene supported on the diamond surface from top and side views for (**a,d**) H, (**b,e**) T and (**c,f**) B configurations. Only the topmost bilayer of the diamond surface and second layer of the diamond surface are highlighted in blue, red and orange, respectively. Reproduced with permission from ref. 9. Copyright (1982) American Physical Society.

Figure 2.2 Electronic band structures of graphene-diamond hybrid (a) and (b) in T configuration, (c) and (d) in B configuration and (e) and (f) in H configuration. Orange lines and cyan lines represent spin-up and spin-down states respectively. The horizontal dashed lines indicate the Fermi level. Insert: the gap of graphene near the K point induced by diamond surface. The linear energy dispersion of graphene in the corresponding GDH around the Fermi energy (dotted line) is also plotted for reference. Reproduced with permission from ref. 9. Copyright (1982) American Physical Society.

Figure 2.3 Three dimensional charge density difference plots (a) side and (b) top views. Green and yellow isosurfaces represent charge depletion and accumulation in the space with respect to isolated graphene and diamond surface. Reproduced with permission from ref. 9. Copyright (1982) American Physical Society.

Figure 2.4 Electronic band structure of graphene on cleaned diamond C(111). The Fermi level is set to zero and marked by green dotted lines. Reproduced with permission from ref 12. Copyright (2013) American Institute of Physics.

Figure 2.5 Cut-off frequencies for three different devices at room temperature. Small-signal current gain |h21| versus frequency for device with a gate length of (a) 550 nm, (b) 140 nm and (c) 40 nm at room temperature. Intercepts give the cut-off frequency as 26 GHz. 70 GHz and 155 GHz respectively. Reproduced with permission from ref. 1. Copyright (2011) Nature Publishing Group

Figure 2.6 Temperature dependence of cut-off frequency for different devices. Current gain as a function of frequency at (a) 300 K, (b) 4.3 K. The gate length is 550nm, with V_{ds} of 1.6 V and with V_{gs} varying from -8 to 0 V. (c) Current gain versus frequency for three values of gate length (550 nm, 140 nm, 40 nm) at 4.3 K. The value of f_T is 28 GHz, 70 GHz and 140 GHz, respectively. (d) Summary plot of the temperature dependence of f_T for the three devices. Reproduced with permission from ref. 1. Copyright (2011) Nature Publishing Group

Figure 4.11 Photocurrent response at different applied voltages (versus Ag/AgCl) of P3HT on modified diamond electrodes under 1 sun (100 mWcm-2, AM 1.5G) illumination (top panel) and photocurrent response of respective modified diamond electrodes at 0V (bottom panel).

Figure 5.1 AFM images of GNBs showing their mechanical strength and sizes. (a) Young's modulus map of GNBs on diamond. (b) Topography map corresponding to a. The scale bars shown in a and b are 150 nm.

Figure 5.2 AFM images of GNBs. (a) Topography of G on diamond after transfer. (b) Topography of GNBs on diamond. Scale bar, 500 nm (a and b). (c) Histogram of the diameter and height distribution of GNBs and (d) High-resolution three-dimensional topography representation of GNBs on diamond, Scale bar, 100 nm.

Figure 5.3 AFM images of exfoliated graphene on diamond. a and b via wet transfer technique (a) before heat treatment (b) after heat treatment and c and d via dry transfer technique (c) before heat treatment and (d) after heat treatment . The scale bars in a, c and d are 500 nm while the scale bar in b corresponds to 100 nm.

Figure 5.4 Probing the electronic structure and properties before and after the formation of GNBs. (a) Valence bands of flat G and GNB on diamond. (b) Electrochemical cyclic voltammetry of diamond, graphene-on-diamond and GNBs-on-diamond using $Fe(CN)_6^{3-/4-}$ in 1M KCl. (c) C12 Raman spectra of (i) flat graphene-on-diamond before GNB formation, (ii) GNBs on diamond and (d) C13 Raman spectra of (i) flat graphene-on-diamond and (ii) GNBs on diamond.

Figure 5.5 Cyclic voltammetry recorded for diamond, graphene on diamond and GNBs on diamond (a) 1 M KCl, scan rate: 100 mV s^{-1}. (b) CVs recorded at GNBs on diamond electrode in 1.0 mM $Fe(CN)_6^{3-/4-}$ in 1 M KCl at various scan rates and (c) peak current dependence on the square root of scan rate.

Figure 5.6 Schematic diagram and vibrational spectroscopy of graphene and diamond. (a) Schematic representation showing water cluster in GNB and weakly interacted water molecules underneath flat G on diamond (top panel). Etching of diamond by supercritical water (bottom panel). FTIR spectra showing OH-stretching peak of water measured on (b) diamond, where raising temperature to 373 K results in the desorption of water (c) Flat G on diamond showing peak at 3,650 cm^{-1} due to the presence of trapped, weakly bonded

water molecules (d) (i) Flat G on diamond, (ii)-(vi) After formation of GNB at a range of temperatures and (vii) Cooling own to room temperature.

Figure 5.7 GNB formation, growth and void generation on diamond. (a) Density functional theory simulation of ground electronic state of flat and curved graphene at B3LYP/6-31 G* level. (b,c) MD simulation of the buckling of graphene on diamond (b) Graphene on C(100)-(2X1). (c) Graphene on dihydride-terminated diamond (denoted as 2H C(100) – (2 x1), where bubble formation can be seem after heating (d) AFM topography image of voids generated on diamond and (e) Scanning electron microscope image of etched diamond, and inset is image zoomed in by 20 times. Scale bar, 0.3, 1 and 0.05 μm, respectively (d, e and inset of e, respectively).

Figure 5.8 Raman spectra after formation of diamond cavities as a function of excitation wavelength (i) At diamond cavities (ii) At flat diamond after formation of cavities.

Figure 5.9 AFM topography and surface properties of sapphire,quartz and O-diamond substrates and graphene on respective substrates. (a-c) Surface topography of bare substrates (a) Sapphire, (b) Quartz, (c) O-diamond, (d) Graphene on sapphire and (e) Graphene on quartz. The scale bars in a- e are 500 nm. (f) High resolution 3D topography representation of GNBs on O-diamond. The corresponding scale bar shown is 100 nm and (g) Contact angle images of H-diamond, O-diamond, sapphire and quartz (from left to right).

Figure 6.1. a) High resolution three-dimensional topography representation of GNBs on diamond, Scale bar, 100 nm. b) Histogram of the diameter and height distribution of GNBs.

Figure 6.2 a) FTIR wide spectra of biphenyl in GNB on diamond before and after phase transition, at 298 K, 773 K and cooled back to 298 K. b) FTIR spectra showing out-of-plane modes of biphenyl in GNB on diamond before and after phase transition, at 298 K, 773 K and cooled back to 298 K. c) Molecular structure of biphenyl, twisted (top) and flat (bottom). d) Frequency shifts of three biphenyl vibrational modes, as a function of temperature. e) Pressure as a function of temperature.

Figure 6.3 Schematic structures of a) (I)Pristine C_{60}., (II)dimer formed from [2+2] cycloaddition, (III)orthorhombic structure where each molecule is bonded to the two nearest neighbour along a <110> fcc direction forming parallel chains and (IV) tetragonal structure where each molecule is bonded to

Figure 7.9 Extent of cytoplasmic lipid accumulation assessed by Oil Red O staining after 14 days of induction on (a) PDMS (i) with induction and (ii) without induction, on (b) G (i) with induction and (ii) without induction, and on (c) GO (i) with induction and (ii) without induction. Scale bars are 50 μm. (d) A higher propensity for adipogenic differentiation was observed for the MSCs differentiated on GO, with significantly larger amount of fat accumulation than the MSCs differentiation on G (b(i) and PDMS (a(i)) (*p<0.05; n=4 for each group). In negative controls without any adipogenic induction chemicals, no lipid deposits were observed.

Figure 7.10 (a) Far UV absorption CD spectra of PBS (black), G in PBS (red), GO in PBS (blue) and Insulin in PBS (green) and (b) Far UV absorption CD spectra of (i) Insulin in PBS- Day 0 (black), Day1 (red) and Day3 (blue) and (ii) its corresponding high tension voltage spectra.

List of Abbreviations and Symbols

AFM	Atomic force microscopy
ARUPS	Angle resolved ultraviolet photoelectron spectroscopy
BDD	Boron-doped diamond
BEI	Backscattered electron image
CD	Circular dichroism
CV	Cyclic voltammetry
CVD	Chemical Vapor Deposition
DAC	Diamond anvil cell
DFT	Density functional theory
DLC	Diamond-like carbon
EDX	Energy-dispersive x-ray microanalysis
FTIR	Fourier transform infrared spectroscopy
FWHM	Full width half maximum
G	Graphene
GDH	Graphene-diamond hybrid
GNBs	Graphene nanobubbles
GO	Graphene oxide
H-diamond	Hydrogen terminated diamond
HOMO	Highest occupied molecular orbital
IP	Ionization potential
IR	Infrared
ITO	Indium tin oxide
MD	Molecular dynamic
MOSFET	Metal oxide field-effect transistor

MSCs	Mesenchymal stem cells
NCD	Nanocrystalline diamond
ND	Nanodiamond
NEA	Negative electron affinity
O-diamond	Oxygen terminated diamond
OTE	Optical transparent electrode
P3HT	Poly-3-hexylthiophene
PBS	Phosphaste-buffered saline
PDMS	Polydimethylsiloxane
PEA	Positive electron affinity
PECVD	Plasma enhanced chemical vapour deposition
PMMA	Poly-methylmethacrylate
PSPD	Position sensitive photo-detector
SCD	Single crystalline diamond
SEI	Secondary electron image
SEM	Scanning electron microscopy
SO	Surface optical
TCO	Transparent conducting oxides
TEM	Tunnelling electron microscopy
UNCD	Ultrananocrytalline diamond
UPS	Ultra-violet photoelectron spectroscopy
UV	Ultraviolet
UV/vis	Ultraviolet and visible
XPS	X-ray photoelectron spectroscopy

A	Absorbance
E_{BE}	Binding energy
k_B	Boltzmann constant
ΔE	Change in energy
$N_{(h/e)}$	Charge carrier concentration (hole or electron)
ρ	Charge density
E_{CBM}	Conduction band minimum
f_T	Cut-off frequency
p	Differential pressure
ΔE_D	Dirac point shift
χ	Electron affinity
E_F	Fermi energy
ν_F	Fermi velocity
D	Grain size
γ	Grüneisen parameter
h	height
I	Intensity
E_{KE}	Kinetic energy
μ	Mobility
ε	Molar absorption coefficient or % strain
l	Path length
h	Planck constant
ν	Poisson ratio
r	Radius
ω	Raman frequency
$\hbar$	Reduced planck constant
σ	Stress at the apex

T	Temperature
K	Thermal conductivity
t	thickness
E_{Vac}	Vacuum level
E_{VB}	Valence band maximum
ν	Velocity of light
λ	Wavelength
W	Width
ϕ	Workfunction
E	Young's modulus

Chapter 1

Introduction

1.1 An introduction to carbon materials

Carbon can be considered to be the most important element for all living organisms on Earth since it constitutes the largest percentage of most organic materials. A unique and fascinating aspect of carbon is the possibility to have different carbon allotropes, where the properties are strongly dependent on the extent and type of hybridization they assume. For example, sp^3 hybridized diamond is a wide-bandgap semiconductor while the sp^2 hybridized graphene is a semimetallic material with unprecedented electron mobility approaching 200, 000 $cm^2/(Vs)$ (measured for suspended graphene at liquid-helium temperatures)[1]. With its myriad forms, carbon-based materials offer new and exciting possibilities for both scientific research and practical applications.

1.2 Graphene and its unique properties

Graphene is a monoatomic layer of sp^2 hybridized carbon bonded together to form a honeycomb lattice, resulting in a highly efficient two-dimensional electron conduction platform with charge carriers that behave as massless Dirac fermions. The properties of graphene can be tailored easily through

chemical modification and it has high specific area of 2,630 m^2/g (ref 2). Its fascinating mechanical[3], optical[4] and thermal properties[5] attract the interests of researchers who study the material for a myriad of applications that ranges from electronics[6], sensor[7], biomedical[8,9] application to energy creation[10] and storage[2].

Since graphene is made up of sp^2 hybridized carbon atoms, three of the four valence electrons of the carbon atoms form strong σ bonds with three other neighboring carbon atoms in the basal plane of graphene. These in plane σ bonds of graphene are responsible for its chemical inertness and stability while its high electrical conductivity is generated by the p_z orbital directed perpendicular to the lattice plane. The remaining electrons which do not participate in the orbital hybridization lie in the $2p_z$ orbitals and collectively form the delocalized π electron cloud above and below the basal plane of graphene bestowing it with unprecedented electron mobility. The highest intrinsic mobility of graphene that has been reported exceeds 200,000 $cm^2/(Vs)$ [11,12]. Yet, such values are not easily realized due to the presence of several scattering mechanisms which limit carrier mobility. While the charge scattering mechanisms in graphene have been the subject of several investigations, there is significant lack of consensus on the nature of the scatterers[12,13]. One of the mechanisms proposed include ionic impurity scattering from charged surface impurities or surface adsorbates, ripples originating from intrinsic graphene sheet, acoustic phonon scattering or extrinsic scattering by surface phonons brought about by the underlying substrate[14].

In addition to its intriguing electronic behavior, the unique optical properties of graphene due to its low dimensionality and conical band structure have stimulated much interest. The optical absorption of graphene is determined purely by fundamental physical constants to be about 2% across the visible and infrared (IR) spectrum[15]. Hence, its optical transparency coupled with its excellent electrical conductivity renders graphene an attractive transparent conducting electrode.

It is also worth mentioning that the impermeability of graphene membrane to atoms and molecules has been established by Leenaerts *et al* using first principles density functional theory investigation[16]. A recent study demonstrated the imaging of trapped water between two graphene membranes using high resolution transmission electron microscopy[17] and another group has tested and verified that the atomic membrane is impermeable to even helium gas[18]. Thus, it is envisioned that graphene sealed microchambers can serve as compliant membrane sensors that probe pressure changes in small volumes associated with chemical reactions, photon detection and even phase transitions[19,20].

1.3 Diamond and its unique properties

The term ‘diamond’ originated from a Greek word *adámas,* which means ‘unbreakable’ or ‘unalterable’. Being the hardest material in the world, the applications of this material in the early periods has been closely associated with its distinguished mechanical properties. Little was known about other

properties of diamond due to the high cost and rarity of research samples. It was only after the breakthrough in Chemical Vapor Deposition (CVD) technology in recent decades that research studies on low pressure diamond growth could be conducted[21]. Furthermore, electrical conductivity can be imparted to the originally insulating diamond by doping with boron or nitrogen atoms. The electrical conductivity of diamond can be controlled by the tuning of dopant concentration and it can even be doped to metallic levels to achieve specific resistivity as low as 0.005 Ω. Apart from its excellent mechanical strength and chemical inertness[22], boron-doped diamond (BDD) has excellent thermal conductivity, high carrier mobilities and large electrochemical potential window, these properties have been exploited for applications in heat sinks for high-power lasers[23], transistors[24] and robust corrosion-resistant electrodes[25]. Besides the outstanding bulk properties that diamond is endowed with, its surface properties are even more notable. Due to the wide bandgap of ~5.47 eV of diamond, its conduction band minimum is placed close to the vacuum level, to result in negative electron affinity and high *p*-type surface conductivity.

Electron affinity (χ) is a measurement of how readily a material accepts electrons into its conduction band minimum (E_{CBM}) or the energy barrier for an electron to escape from the E_{CMB} into the vacuum level. Hence, it is determined by the energy difference between the conduction band minimum (E_C) and its vacuum level (E_{Vac}). The E_{CBM} of most materials lie below their E_{Vac} and these materials are deemed to have positive electron affinity (PEA). On the contrary, due to the wide bandgap that diamond possesses, its E_{CBM} is located near to or even above its E_{Vac} to exhibit negative electron affinity

(NEA). In other words, once electrons are excited from the valence band to the conduction band, these electrons can thermalize to the vacuum level and are capable of being emitted without any barrier. Thus, materials with NEA are used to fabricate devices such as photo-cathodes, secondary electron emitters as well as cold cathode photo emitters.

In 1989, Landstrass and Ravi demonstrated that despite being a large bandgap semiconductor, diamond has surprisingly high electrical conductivities[26]. Their work sparked the interest of many researchers to uncover the origin of this unexpected conductivity. More interestingly, it has been discovered that diamond is found to be intrinsically insulating under vacuum environment but acquires surface conductivity upon exposure to ambient conditions[27]. Thus, it has been proposed that at ambient conditions, a thin water layer that adsorbs on diamond surface is responsible for the p-type surface conductivity. This is due to the presence of a hole accumulation layer which arises from electron transfer between the diamond and an aqueous electrochemical redox couple $O_2 + 4H^+ + 4e^- \rightleftharpoons 2H_2O$, which results in the consumption or formation of O_2. The atmosphere provides a source of electrons whose electrochemical potential (Fermi energy) is fixed by the oxygen redox couple and when water film is adsorbed on diamond, electrons will tend to be transferred in the direction equilibrating the Fermi level of diamond to the ambient film[28]. The band line-up in Fig. 1.1 shows the band line-up for hydrogen-terminated diamond in contact with an aqueous phase. The electrochemical potentials of the oxygen redox couple are shown at pH =0 and pH=14.

$$O_2 + 4H^+ + 4e^- \rightleftharpoons 2H_2O$$

dominates at acidic conditions (1.1)

$$O_2 + 2H_2O + 4e^- \rightleftharpoons 4OH^-$$

dominates at basic conditions (1.2)

Since the ambient film adsorbed on diamond contains CO_2, protons which arises from the CO_2-water association bestows acidity to the film, making equation 1.1 to be the dominant reaction occurring at the diamond and water interface.

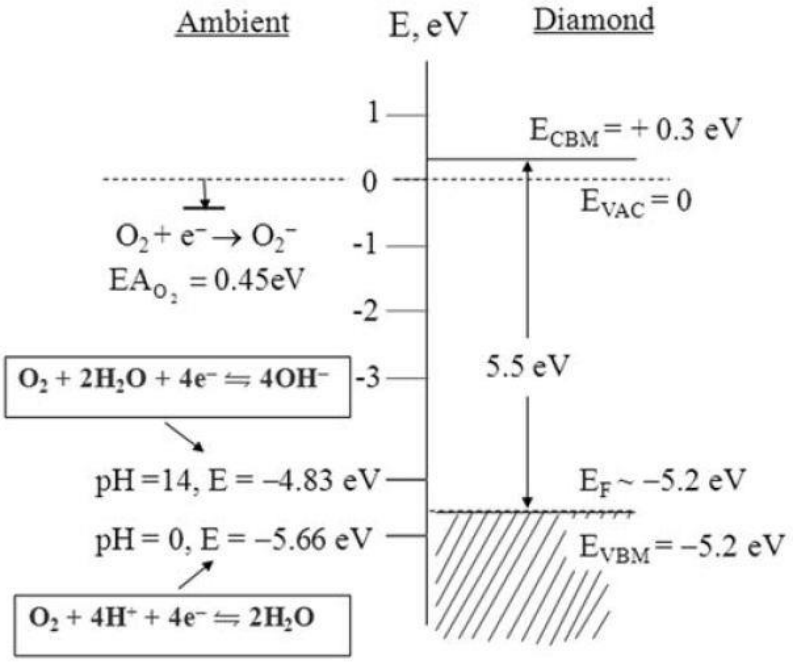

Figure 1.1 Estimated band line-up of hydrogen-terminated diamond in contact with an aqueous solution. The electrochemical potentials of the oxygen redox couple are shown at pH= 0 and pH= 14. The electron affinity of gaseous O_2 is also shown (E= -EA = -0.451 eV). Reproduced with permission from ref. 28 Copyright (2007) Science Publishing Group.

For diamond to be exploited for various applications, strategies have been developed to impart functional groups onto the surface of diamond. Over

the years, methods that have been reported range from using chemical, photochemical to electrochemical to tether functionalities onto the otherwise inert surface of diamond. UV photochemical functionalization is a convenient method allowing the patterning of a substrate surface through the use of a photomask. It has been concluded by Yang *et al*[29] that photochemical functionalization is a surface-mediated photochemical reaction initiated by the photo-ejection of electrons from the H-terminated diamond to the alkene liquid phase reactants as illustrated in the step-by step schematic drawing shown in Fig. 1.2.

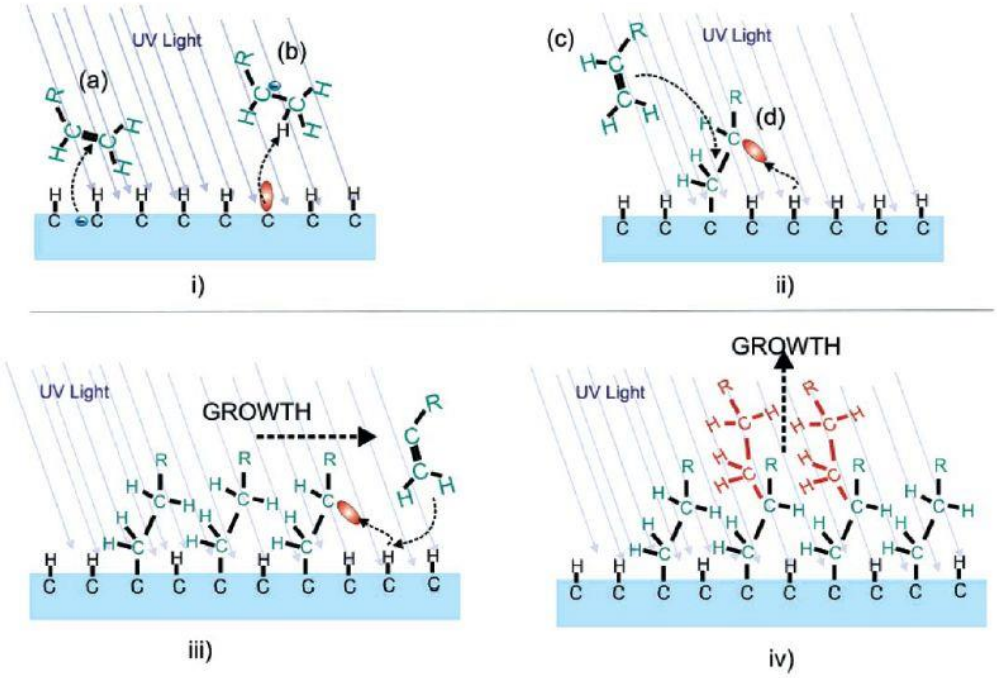

Figure 1.2 Schematic grafting of the diamond surface by amines. (i) The generation of radical anions by electron transfer from diamond to the olefin (a); the nucleophilic properties of the radical causes a hydrogen abstraction (b), which results in a surface carbon dangling bond; (ii) the dangling bond reacts with an olefin molecule to form a diamond-carbon/olefin-carbon bond. (c). This olefin abstracts a hydrogen atom from the diamond surface (d), which is a new site for olefin addition; (iii) the hydrogen abstraction reaction results in a chain reaction; (iv) in the case of extended illumination, a 3D growth sets in, due to cross-polymerization of olefin molecules. Reproduced with permission from ref. 29. Copyright (2007) American Chemical Society.

Although UV photochemical reaction is a convenient method for the surface functionalization of diamond, it is limited to alkyl as the presence of unsaturated bonds opens up non-selective pathways of attachment to the surface with UV activation. To ensure the stability of a molecular device, strong interfacial bonding is essential and a dense organic film will impede water to infiltrate to the interface, thus prohibiting hydrolysis and/or oxidative

cleavage. As such, the coupling of aryl compound is desirable as π-π stacking of the benzene rings will afford denser packing of the layer relative to a layer built from alkyl groups. Moreover, the delocalized electrons of the aryl functionalities enable more efficient charge transfer, which is critical when diamond is applied as an electrode in organic electronics. As such, diazonium grafting chemistry (which is employed for the coupling of graphene to diamond in Chapter 4) has been developed and utilized in many applications fields ranging from molecular electronics to combinatorial chemistry[30].

1.4 Graphene-diamond hybrid

Owing to their unique properties, both graphene and diamond have each established their respective niche as functional materials in various applications. Although the phases of diamond and graphite are known to coexist in surface-graphitized nanodiamond particles or during the initial nucleation stages of diamond growth[31-34], there is no clear insight into how graphene interfaces with diamond both structurally and electronically. The metallic-sp^2 and dielectric-sp^3 interface offer the perfect environment for studying the complex interplay between electronic and lattice degrees of freedom for the creation of new functionalities.

Researchers have recently exploited some of diamond's inherent properties to elicit the hidden intrinsic potential of graphene and vice versa. For example, diamond-like carbon (DLC) has been employed as a substitute of SiO_2 for constructing radio-frequency (r.f.) transistors[35] to mitigate the scattering of

charge carriers associated with low surface phonon energy (59 meV) and large trap density of SiO_2. Figure 1.3 shows top-gated CVD graphene R.F. transistors with gate length scaled down to 40 nm, it is the shortest gate length demonstrated on graphene R.F. devices to date. Cut-off frequencies as high as 155 GHz have been obtained for the 40 nm transistors, and the cut-off frequency was found to scale as 1/(gate length).

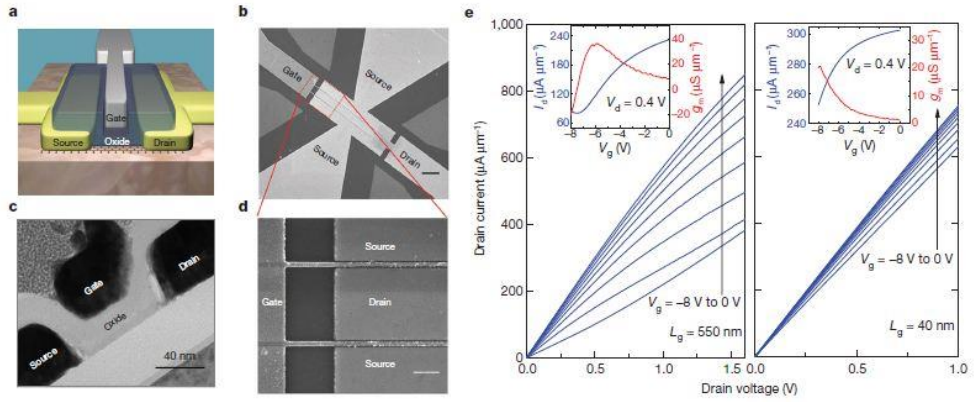

Figure 1.3 Fabrication and output characteristics for graphene r.f. transistors. (a) Schematic view of a top-gated graphene r.f. transistor on DLC substrate. (b) SEM image of a typical top-gated dual channel r.f. device. Scale bar, 3 μm. (c) Cross section TEM image of a graphene transistor with a gate length of 40 nm. Scale bar, 40 nm. (d) SEM image of the 40 nm device. Scale bar, 400 nm. (e) D.C. output characteristics of a 550 nm device (left) and a 40 nm device (right). Insets, transfer characteristics at drain-source voltage V_{ds}= 0.4 V. Reproduced with permission from ref. 35. Copyright (2011) Nature Publishing Group.

DLC has a higher phonon energy (owing to the high phonon energy in diamond (165 meV) as compared to 59 meV of SiO_2 and a lower surface trap density as it is typically non-polar and chemically inert). In addition, diamond has also been selected for its high thermal conduction property for use as a bottom dielectric in graphene devices, as the thermally resistive SiO_2 often acts as the thermal bottleneck, causing the breakdown of graphene devices. It

has been reported that by replacing SiO_2 with synthetic diamond as the underlying substrate, the maximum current-carrying capacity of graphene can be improved by approximately 20 times stemming from more efficient dissipation and propagation of heat from the graphene channel to diamond[36]. This demonstration reveals the potential of using sp^2 carbon on on sp^3 carbon technology for future applications in high-frequency transistors, interconnects and transparent electrodes.

1.5 Graphene and diamond for tissue engineering

With an increasing range of tissue types being studied for tissue engineering, the demand for novel scaffold is growing. The scaffold used for tissue engineering is usually a porous structure that serves as a substrate for tissue regeneration and growth[37]. The scaffold guides and facilitates the development of new biological tissue formation. Different types of biological tissue will require different type and form of scaffold for optimal growth. Therefore, it is crucial that the design of the scaffold for the particular tissue type to be thoroughly considered and design in optimizing tissue regeneration.

The merits of carbon materials, which include unique chemical and physical structure, biocompatibility, large surface area to volume ratio, high chemical stability, are highly suitable for use as scaffolds for tissue engineering. Nanostructured materials are believed to promote preferential adhesion of osteoblasts over other cell types (e.g. fibroblasts, chondrocytes, smooth muscle cells), which could possibly prevent fibrous encapsulation of

bone implant[38,39]. The surface nanostructure of the material has been demonstrated to enhance the strength of cell adhesion, spreading ability and differentiation[40-43] of mesenchymal and osteoprogenitor cells[44].

Due to the high surface area of graphene oxide, it is anticipated that surface phenomena like physical adsorption will play an important role in terms of interaction with small molecules in physiological fluids. Adsorption on carbon surfaces is generally favoured for molecules with low solubility, partial hydrophobicity or molecules that are positively charged (as the oxygen functionalities on graphene oxide are often negatively charged), as well as molecules with unsaturated bonds which are prone to π-π stacking with the basal plane of graphene. In addition, the mechanical properties of graphene such as high elasticity, flexibility and adaptability to its supporting substrate[3,45,46] are advantageous for structural reinforcement, for the increase in tensile strength and elasticity modulus of biocompatible films and other scaffold materials that are frequently used for tissue engineering. However, to date, the toxicological profiles of graphene-based nanomaterials has not yet been well elucidated as the biomedical research is still at its infancy stage. Assessment of toxicological side effects is necessary to pave the way for future development and application of graphene-based nanomaterials in the biomedical field.

Among all carbon materials studied, only nanocrystalline diamond (NCD) has shown excellent biocompatibility and no cytotoxicity in both *in vitro* and *in vivo* studies. Moreover, due to the wide range of unique physiochemical and biological properties, such as mechanical hardness, chemical and thermal resistance, intriguing optical and electrical properties that it exhibits, NCD has

attracted vast attention for use in biomedical research over the past decade. The anticipated beneficial action of these NCD films is not only due to those properties mentioned above but also its surface nanoroughness. Surface nanotopography has been reported to stimulate adhesion, growth and maturation of osteoblasts, as well as differentiation of bone progenitor cells towards the osteoblastic phenotype[38,47]. This favourable cell behavior probably arises due to the nanostructure of the material, which improves the adsorption of extracellular matrix molecules, e.g. fibronectin, vitronectin and collagen from the cell culture serum, which serve as a platform for subsequent cell attachment. Figure 1.4 shows optical images and cell density of MG 63 cells taken at Day 3 after seeding[48]. On day 3 after seeding, the number of viable cells on both flat and rough silicon substrates was measured to be 3,160 ±1,450 cells/cm^2 and 290 ±150 cells/cm^2 respectively. In contrast, the cell number on micro-nanostructured NCD and nanostructured NCD was determined to be 60,200 ± 6,420 cells/cm^2 and 72,020 ± 6,540 cells/cm^2 which attained higher values than the conventional polystyrene culture plate (40,750 ± 2,530 cells/cm^2) and glass (42,840 ± 8,480 cells/cm^2).

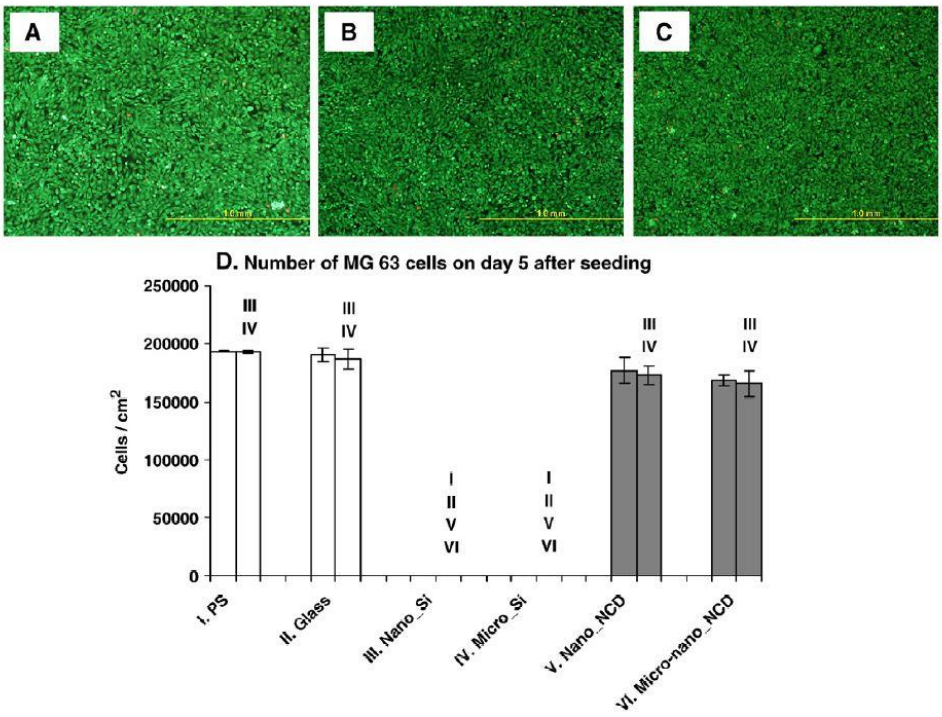

Figure 1.4 A-C: Flureoscence staining of MG 63 cells stained with LIVE/DEAD viability/cytotoxicity kit on day 5 after seeding on (a) Polystyrene culture dishes (b) Nanostructured diamond films (c) Diamond films with hierarchically organized micro- and nanostructure (d). Number of MG 63 cells on day 5 after seeding on (i) Polystyrene culture dishes (PS) (ii) Microscopic glass coverslips (Glass) (iii) Nanostructured silicon substrates (Nano_Si) (iv) Microstructured silicon substrates (Micro_Si) (v) Nanostructured diamond films (Nano_NCD) and (vi) Diamond films with hierarchically organized micro- and nanostructure (Micro-nano_NCD). First column shows: the total cell number, the second column: number of viable cells. Mean ± S.EM. from 3 samples. ANOVA, Student-Newman-Keuls Method. Statistical significance: ^{I,II,III,IV,V,VI}: $p \leq 0.05$ in comparison with the sample of the same Roman number. Reproduced with permission from ref. 48. Copyright (2008) Elsevier.

There have been exciting discoveries from the exploration of carbon materials for biomedical applications over the last few years. Although this research area is still in its infancy, graphene, graphene derivatives and diamond have been demonstrated to be biocompatible substrates for the promotion of adhesion, growth and differentiation of various stem cells. The

tunablity of surface terminations and the chemical stability of the C-C interface advocate the broad potential of these nanomaterials as extracellular scaffolds to enhance growth and induce osteogenesis, adipogenesis and neurite outgrowth among others.

1.6 Overview of objectives and work scope

This work seeks to explore new applications of carbon-based materials by exploiting the superlative properties of graphene and diamond. To gain a better appreciation and understanding of the graphene-diamond hybrid, we will examine how the difference in the degree of interaction (physisorption and chemisorption) between graphene and diamond will result in modifications of their inherent properties in Chapter 2. This is further supplemented with an overview of experimental techniques employed for the study and characterization of the graphene-diamond interface in Chapter 3.

In Chapter 4 of this thesis, transport property at the interface of graphene-diamond (physisorbed) is studied with the aim to investigate the role of the various scattering mechanisms. Due to the non-polar nature of diamond, it can be used as a substrate with reduced density of charge impurities and may potentially enhance the performance of graphene transistors. BDD grown on quartz has been considered a potential alternative in replacing indium tin oxide (ITO) as a transparent anode for photovoltaic applications[49]. Although doping with boron atoms enhances the electrical conductivity of the diamond electrode, the increase in dopant concentration will result in a compromise on

its optical transparency; hence a balance between conductivity and transparency must be achieved for use as a transparent electrode. Since graphene absorbs *ca.* 2% of visible light, we seek to improve the electrical conductivity of the electrode in Chapter 4 by coupling of the graphene membrane to BDD via molecular wire.

In Chapter 5, heat treatment at the graphene-diamond interface produces a high density of graphene nanobubbles (GNBs) which can trap water within. At high temperature, chemical bonding between graphene and diamond is robust enough to allow the hybrid interface to act as a hydrothermal anvil cell due to the impermeablilty of graphene. Interestingly, we discover that when GNBs on diamond is heated to elevated temperature (pressure), water trapped inside these bubbles is transformed into a supercritical fluid, which is highly corrosive and etches diamond. Subsequently, in Chapter 6, we probed the pressure inside GNBs by encapsulating various phenyl molecules whose conformation is sensitive to changes in pressure. After establishing the pressure in the GNB at a given temperature, the GNB was used as a high pressure reaction vessel for ultrahigh pressure chemistry. The different phases in high-pressure induced polymerization of fullerene could be observed. Finally in Chapter 7, diamond and graphene, each displaying their unique physical, chemical and mechanical properties are explored as biocompatible scaffolds for use in tissue engineering and regenerative medicine.

In summary, the findings presented in this dissertation are important for the understanding of the interfacial properties of graphene and diamond. The thesis also examined the binding of graphene and diamond (sp^2-sp^3 carbon carbon interface), where strong interfacial bonding and impermeability of

graphene enable the construction of a hydrothermal graphene-diamond anvil cell. Owing to the biocompatibility of these carbon materials, they were explored for biomedical applications as biomimetic platforms.

1.7 References

1 Du, X., Skachko, I., Barker, A. & Andrei, E. Y. Approaching ballistic transport in suspended graphene. *Nature Nanotechnology* **3**, 491-495 (2008).

2 Stoller, M. D., Park, S., Yanwu, Z., An, J. & Ruoff, R. S. Graphene-Based ultracapacitors. *Nano Letters* **8**, 3498-3502 (2008).

3 Lee, C., Wei, X., Kysar, J. W. & Hone, J. Measurement of the elastic properties and intrinsic strength of monolayer graphene. *Science* **321**, 385-388 (2008).

4 Balapanuru, J. *et al.* A graphene oxide-organic dye ionic complex with DNA-sensing and optical-limiting properties. *Angewandte Chemie - International Edition* **49**, 6549-6553 (2010).

5 Balandin, A. A. *et al.* Superior thermal conductivity of single-layer graphene. *Nano Letters* **8**, 902-907 (2008).

6 Das, A. *et al.* Monitoring dopants by Raman scattering in an electrochemically top-gated graphene transistor. *Nature Nanotechnology* **3**, 210-215 (2008).

7 Dan, Y., Lu, Y., Kybert, N. J., Luo, Z. & Johnson, A. T. C. Intrinsic response of graphene vapor sensors. *Nano Letters* **9**, 1472-1475 (2009).

8 Nayak, T. R. *et al.* Graphene for controlled and accelerated osteogenic differentiation of human mesenchymal stem cells. *ACS Nano* **5**, 4670-4678 (2011).

9 Lee, W. C. *et al.* Origin of enhanced stem cell growth and differentiation on graphene and graphene oxide. *ACS Nano* **5**, 7334-7341 (2011).

10 Wang, Y., Tong, S. W., Xu, X. F., Özyilmaz, B. & Loh, K. P. Interface engineering of layer-by-layer stacked graphene anodes for high-performance organic solar cells. *Advanced Materials* **23**, 1514-1518 (2011).

11 Chen, J. H., Jang, C., Xiao, S., Ishigami, M. & Fuhrer, M. S. Intrinsic and extrinsic performance limits of graphene devices on SiO_2. *Nature Nanotechnology* **3**, 206-209 (2008).

12 Morozov, S. V. *et al.* Giant intrinsic carrier mobilities in graphene and its bilayer. *Physical Review Letters* **100** 016602 (2008).

13 Hwang, E. H., Sensarma, R. & Das Sarma, S. Coulomb drag in monolayer and bilayer graphene. *Physical Review B - Condensed Matter and Materials Physics* **84** 245441(2011).

14 Burghard, M., Klauk, H. & Kern, K. Carbon-based field-effect transistors for nanoelectronics. *Advanced Materials* **21**, 2586-2600 (2009).

15 Bonaccorso, F., Sun, Z., Hasan, T. & Ferrari, A. C. Graphene photonics and optoelectronics. *Nature Photonics* **4**, 611-622 (2010).

16 Leenaerts, O., Partoens, B. & Peeters, F. M. Graphene: A perfect nanoballoon. *Applied Physics Letters* **93** 193107 (2008).

17 Yuk, J. M. *et al.* High-resolution EM of colloidal nanocrystal growth using graphene liquid cells. *Science* **335**, 61-64 (2012).

18 Bunch, J. S. *et al.* Impermeable atomic membranes from graphene sheets. *Nano Letters* **8**, 2458-2462 (2008).

19 Jiang, C., Markutsya, S., Pikus, Y. & Tsukruk, V. V. Freely suspended nanocomposite membranes as highly sensitive sensors. *Nature Materials* **3**, 721-728 (2004).

20 Mueggenburg, K. E., Lin, X. M., Goldsmith, R. H. & Jaeger, H. M. Elastic membranes of close-packed nanoparticle arrays. *Nature Materials* **6**, 656-660 (2007).

21 Yarbrough, W. A. & Messier, R. Current issues and problems in the chemical vapor deposition of diamond. *Science* **247**, 688-696 (1990).

22 Perret, A. *et al.* Electrochemical behavior of synthetic diamond thin film electrodes. *Diamond and Related Materials* **8**, 820-823 (1999).

23 Dyment, J. C. & D'Asaro, L. A. Continuous operation of gaas junction lasers on diamond heat sinks at 200°K. *Applied Physics Letters* **11**, 292-294 (1967).

24 Rezek, B., Watanabe, H., Shin, D., Yamamoto, T. & Nebel, C. E. Ion-sensitive field effect transistor on hydrogenated diamond. *Diamond and Related Materials* **15**, 673-677 (2006).

25 Härtl, A. *et al.* Protein-modified nanocrystalline diamond thin films for biosensor applications. *Nature Materials* **3**, 736-742 (2004).

26 Landstrass, M. I. & Ravi, K. V. Resistivity of chemical vapor deposited diamond films. *Applied Physics Letters* **55**, 975-977 (1989).

27 Maier, F., Riedel, M., Mantel, B., Ristein, J. & Ley, L. Origin of surface conductivity in diamond. *Physical Review Letters* **85**, 3472-3475 (2000).

28 Chakrapani, V. *et al.* Charge transfer equilibria between diamond and an aqueous oxygen electrochemical redox couple. *Science* **318**, 1424-1430 (2007).

29 Yang, N., Uetsuka, H., Watanabe, H., Nakamura, T. & Nebel, C. E. Photochemical amine layer formation on H-terminated single-crystalline CVD diamond. *Chemistry of Materials* **19**, 2852-2859 (2007).

30 Coulon, E., Pinson, J., Bourzat, J. D., Commerçon, A. & Pulicani, J. P. Surface-modified carbon felts: Possible supports for combinatorial chemistry. *Journal of Organic Chemistry* **67**, 8513-8518 (2002).

31 Bundy, F. P. Direct conversion of graphite to diamond in static pressure apparatus. *Science* **137**, 1057-1058 (1962).

32 Irifune, T., Kurio, A., Sakamoto, S., Inoue, T. & Sumiya, H. Materials: Ultrahard polycrystalline diamond from graphite. *Nature* **421**, 599-600 (2003).

33 Khaliullin, R. Z., Eshet, H., Kühne, T. D., Behler, J. & Parrinello, M. Nucleation mechanism for the direct graphite-to-diamond phase transition. *Nature Materials* **10**, 693-697 (2011).

34 Ohfuji, H. & Kuroki, K. Origin of unique microstructures in nano-polycrystalline diamond synthesized by direct conversion of graphite at static high pressure. *Journal of Mineralogical and Petrological Sciences* **104**, 307-312 (2009).

35 Wu, Y. *et al.* High-frequency, scaled graphene transistors on diamond-like carbon. *Nature* **472**, 74-78 (2011).

36 Yu, J., Liu, G., Sumant, A. V., Goyal, V. & Balandin, A. A. Graphene-on-diamond devices with increased current-carrying capacity: Carbon sp 2-on-sp 3 technology. *Nano Letters* **12**, 1603-1608 (2012).

37 Li, X. *et al.* Recent patents on polymeric scaffolds for tissue engineering. *Recent Patents on Biomedical Engineering* **2**, 65-72 (2009).

38 Price, R. L., Ellison, K., Haberstroh, K. M. & Webster, T. J. Nanometer surface roughness increases select osteoblast adhesion on carbon nanofiber compacts. *Journal of Biomedical Materials Research - Part A* **70**, 129-138 (2004).

39 Webster, T. J. & Smith, T. A. Increased osteoblast function on PLGA composites containing nanophase titania. *Journal of Biomedical Materials Research - Part A* **74**, 677-686 (2005).

40 Kim, H. J. *et al.* Varying Ti-6A1-4V surface roughness induces different early morphologic and molecular responses in MG63 osteoblast-like cells. *Journal of Biomedical Materials Research - Part A* **74**, 366-373 (2005).

41 Zhao, G. *et al.* High surface energy enhances cell response to titanium substrate microstructure. *Journal of Biomedical Materials Research - Part A* **74**, 49-58 (2005).

42 Sammons, R. L., Lumbikanonda, N., Gross, M. & Cantzler, P. Comparison of osteoblast spreading on microstructured dental implant surfaces and cell behaviour in an explant model of osseointegration: A

scanning electron microscopic study. *Clinical Oral Implants Research* **16**, 657-666 (2005).

43 Zhao, G. *et al.* Osteoblast-like cells are sensitive to submicron-scale surface structure. *Clinical Oral Implants Research* **17**, 258-264 (2006).

44 Tsai, I. Y. *et al.* Fibroblast adhesion to micro- and nano-heterogeneous topography using diblock copolymers and homopolymers. *Journal of Biomedical Materials Research - Part A* **71**, 462-469 (2004).

45 Frank, I. W., Tanenbaum, D. M., Van Der Zande, A. M. & McEuen, P. L. Mechanical properties of suspended graphene sheets. *Journal of Vacuum Science and Technology B: Microelectronics and Nanometer Structures* **25**, 2558-2561 (2007).

46 Lee, Y. *et al.* Wafer-scale synthesis and transfer of graphene films. *Nano Letters* **10**, 490-493 (2010).

47 Dalby, M. J. *et al.* Osteoprogenitor response to semi-ordered and random nanotopographies. *Biomaterials* **27**, 2980-2987 (2006).

48 Grausova, L. *et al.* Bone and vascular endothelial cells in cultures on nanocrystalline diamond films. *Diamond and Related Materials* **17**, 1405-1409 (2008).

49 Lim, C. H. Y. X., Zhong, Y. L., Janssens, S., Nesladek, M. & Loh, K. P. Oxygen-terminated nanocrystalline diamond film as an efficient anode in photovoltaics. *Advanced Functional Materials* **20**, 1313-1318 (2010).

Chapter 2

Literature review

2.1 Potentials of the graphene-diamond interface

In this chapter, we will examine the interactions of graphene and diamond and how the interaction affects their properties. Studies on the graphene-diamond interface can be classified by the extent of interaction between these two materials. One perspective is to understand how the properties of one material affect the other depending on whether they are weakly interacting (van der Waals forces) or whether they are covalently bonded. The first study on the graphene-diamond interface was only reported in 2011 by Wu *et al.*[1]. High-frequency graphene transistor was constructed on diamond-like carbon for radio-frequency (r.f.) applications. Since then, graphene-diamond hybrid (GDH) system has attracted interests from both the theoreticians and the experimentalists. Diamond has been identified as an inert substrate for graphene due to its high surface phonon energy[2,3] and low surface trap density[3]. The current-capacity of graphene on diamond can be improved by one order of magnitude as compared to graphene on SiO_2/Si devices at ambient conditions[4]. The increased current capacity of graphene can be achieved not only on single-crystal diamond substrates but also on synthetic ultrananocrystalline diamond, which can be industrially scaled up. The high

thermal conductivity of diamond also increases the current-carrying capacity on graphene-on-diamond devices.

There are a few studies on the interface of chemically bound graphene-diamond[5,6]. Tzeng *et al* synthesized graphene nanowalls directly on a diamond film by direct current plasma enhanced chemical vapour deposition and demonstrated that this multi-layer turbostratic graphitic carbon nanostructure has excellent electrochemical durability, low background current and wide electrochemical potential window[7].

2.2 Graphene-diamond: Physisorbed

It has been demonstrated that using a diamond-like carbon (DLC) film grown on SiO_2 as substrate can effectively enhance the performance of graphene radio frequency (r.f.) transistor[1], which has great potential for commercialization. Typically, previous studies on graphene-based transistors are fabricated on silicon dioxide (SiO_2) as the substrate. However, graphene devices built on SiO_2 is faced with the issue of additional scattering which results from the low surface phonon energy of SiO_2 in addition to the large charge trap density in SiO_2, causing inhomogeneity and deteriorating the performance of the device. The energy of the optical phonons in diamond takes a value of 165 meV, which is much larger than SiO_2, 59 meV. The latter can improve the saturation velocity in graphene when it is limited by the surface electron-phonon scattering[2]. Moreover, due to the non-polar and

chemical inert nature of diamond, it is anticipated that the charge traps present on this substrate is very much reduced[3].

2.2.1 Theoretical investigation

Properties of the graphene-diamond hybrid were examined by a series of theoretical efforts. Particularly, density functional calculations were employed to investigate the strength of interaction between graphene and diamond and subsequently how electronic and magnetic properties of graphene will be affected.

The surface of diamond C(111) possessing triangular lattices of C atoms at the topmost layer was selected for investigation as this facet of diamond is anticipated to have the least mismatch with graphene lattice. The surface of diamond (111) is modelled by a slab containing six C bilayers with H passivation on the second surface of the slab. To bring into focus the fundamental properties of graphene adsorbed on diamond, Ma *et al* chose a lateral lattice parameter for triangular lattice a= 4.940 Å that is optimized for isolated graphene[8]. The energetic and electronic structure of graphene was investigated with three different stacking configuration on diamond surface: (1) four C atoms of graphene are placed on the hollow sites of the surface bilayer [H configuration, as shown in Fig. 2.1a and 2.1d]; (2) four C atoms of graphene placed directly above the C atoms of the second layer [T configuration, as shown in Fig. 2.1b and 2.1e]; (3) four C atoms of graphene are placed on the bridge sites of the surface bilayer [B configuration, as shown in Fig. 2.1c and 2.1f]

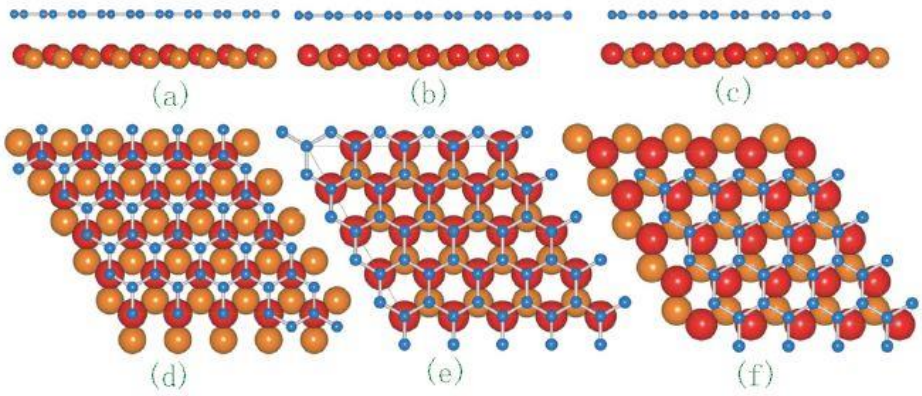

Figure 2.1 Equilibrium structure of graphene supported on the diamond surface from top and side views for (**a,d**) H, (**b,e**) T and (**c,f**) B configurations. Only the topmost bilayer of the diamond surface and second layer of the diamond surface are highlighted in blue, red and orange, respectively. Reproduced with permission from ref. 9. Copyright (1982) American Physical Society.

Figure 2.1 illustrates the optimized geometrical structures of graphene adsorbed on diamond. Graphene was found to maintain an interlayer spacing of 2.957 Å, 2.807 Å and 2.781 Å for H, T and B configurations respectively, without any distortion of its hexagonal network. The interlayer spacing between graphene and diamond for all the configurations above was found to be larger than the typical C-C bond length, indicating the absence of covalent bonding between the graphene and diamond layers. The atomic structures of C(111), with and without the graphene layer were found to be almost unchanged. This is an indication that graphene is loosely bound to the diamond surface. Despite the weak interaction between graphene and diamond, the electronic structure of graphene is found to be altered by diamond. The calculated electronic band structures with H, T and B configurations are illustrated in Fig. 2.2. The total magnetic moments of isolated graphene is zero and isolated graphene placed on H, T and B configurations are non-magnetic.

Spin polarization was induced in graphene by the diamond surface and it must originate from the interfacial proximity with the diamond surface.

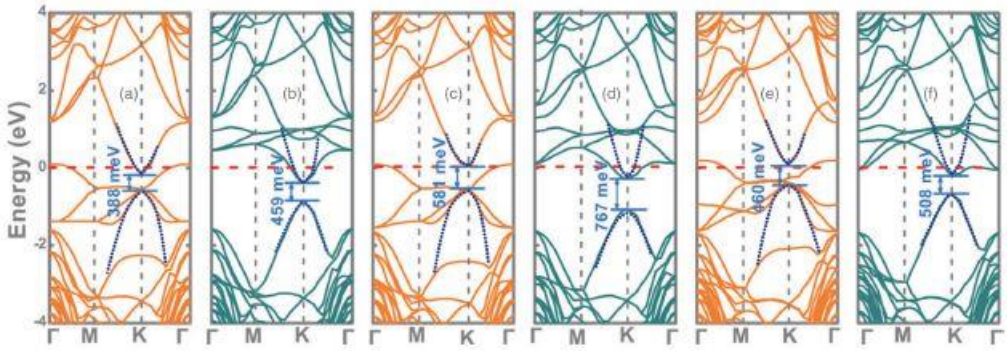

Figure 2.2 Electronic band structures of graphene-diamond hybrid. (a) and (b) in T configuration, (c) and (d) in B configuration, (e) and (f) in H configuration. Orange lines and cyan lines represent spin-up and spin-down states respectively. The horizontal dashed lines represent Fermi level. Insert illustrates the gap of graphene near the K point induced by diamond surface. The linear energy dispersion of graphene in the corresponding GDH around the Fermi energy (dotted line) is also plotted. Reproduced with permission from ref. 9. Copyright (1982) American Physical Society.

It can be seen in Fig. 2.2 that much of the electronic energy band of pristine graphene is still preserved despite its interaction with diamond. However, a finite energy gap at the *K* points is observed due to the repulsion of π and π* bands. As a result, graphene is transformed into a semiconductor material with a small fundamental bandgap, instead of a metallic material with its π and π* bands crossing at the Brillouin zone of the system (*K* points). On the account that graphene-diamond hybrid can create a finite band gap without degrading the electronic properties of graphene, it serves as a promising material for the construction of electronic devices. Moreover, the magnitudes of band gap created are significantly greater than k_BT at room temperature, implying the achievable current on/off ratio is larger than that of freestanding graphene. Creation of a finite band gap in graphene by placing it in the

proximity of diamond can be understood in terms of the π-electron tight-binding approximation of graphene model[8]. Based on this model, the variation in the onsite energy of C atom in graphene induced by the diamond surface disrupts the degeneracy of the π and π* bands at the *K* point, giving rise to its semiconductor character. In order to understand the bonding mechanism, the charge density difference of the hybrid material and the individual phase (graphene and diamond) is examined independently.

$$\Delta\rho = \rho(GDH) - \rho(G) - \rho(D) \qquad \text{(Equation 2.1)}$$

The difference in charge density is derived from subtraction of the calculated electronic charge of the graphene-diamond hybrid from that of the independent graphene and diamond surface (equation 2.1). Figure 2.3 shows that plot of charge density difference for graphene-diamond hybrid in the H configuration and redistribution of charge density within graphene can be seen clearly. Formation of electron-rich and hole-rich regions within graphene is attributed to the inhomogenous planar diamond which drives interlayer electron transfer from diamond surface to graphene. Hence, graphene on diamond surface is slightly n-doped due to the charge transfer. In addition, it can also be seen in Fig. 2.3 that there is a slight but significant accumulation of charges at the interface between graphene and diamond as a result of their interaction.

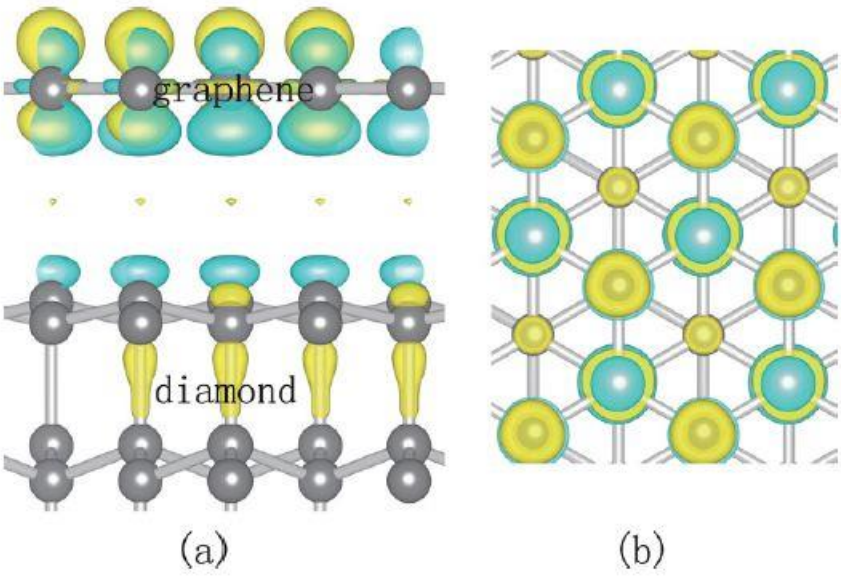

Figure 2.3 Three dimensional charge density difference plots. (a) side and (b) top views. Green and yellow isosurfaces represent charge depletion and accumulation in the space with respect to isolated graphene and diamond surface. (Reproduced with permission from ref. 9. Copyright (1982) American Physical Society.

It should also be noted that when isolated graphene is taken from H, T or B, configurations are non-magnetic. However, when graphene is brought into proximity with diamond, it acquires spin-polarization. This intriguing phenomenon is proposed to arise from the effect of the through-space exchange interaction[8]. This effect causes a material with specific properties to induce similar characteristics on the adjacent material through charge transfer between the two materials. Equation 2.2 represents the path that an electron takes:

$$\beta - \alpha - (\beta - \alpha)_n - \beta (n = 1,2,3 \dots) \qquad \text{(Equation 2.2)}$$

where α and β represent the material with and without specific properties. When the electron returns back to β, the character of α would be transferred to β. Hence, for the graphene-diamond hybrid system, an electron from graphene

tunnels onto diamond surface, is spin polarized and returns back to graphene. This process effectively enhances the spin-polarization strength of graphene.

After examining the interaction of graphene with diamond (111) surface terminated with hydrogen groups, it is worthwhile to consider the well-known Pandey-chain reconstruction that is associated with the C(111) surface[9,10] and if the surface reconstruction of diamond has any impact on graphene. Cleaned diamond (111) surface exhibits a Pandey-chain reconstruction[9,10], in which the top two rows of carbon atoms reconstruct to form zigzag chains rendering the material to be non-magnetic and metallic. The equilibrium adsorption distance of graphene from the surface of cleaned C(111) is 3.34 Å. The equilibrium distance of two clean C(111) gives a distance of 3.35 Å, which agrees closely with the interlayer separation in graphite[11] and bilayer graphene[12,13]. As shown in Fig. 2.4, the electronic structure of graphene around the Dirac point is almost unaffected despite the adsorption of graphene on the surface of cleaned C(111)[14].

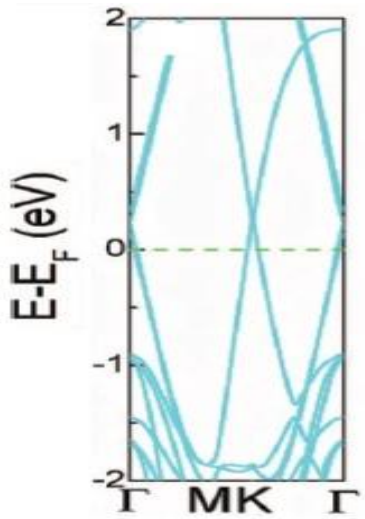

Figure 2.4 Electronic band structure of graphene on cleaned diamond C(111). The Fermi level is set to zero and marked by green dotted lines. Reproduced with permission from ref 14. Copyright (2013) American Institute of Physics.

The slight orbital hybridization between graphene and diamond surfaces induces small bandgap of 5 meV at the Dirac point of graphene on the reconstructed (111) surface. The large discrepancy in the magnitude of band gap induced in graphene by diamond (with and without Pandey chain reconstruction) can be reconciled by difference in the extent of their interaction. When reconstruction of the diamond surface is not considered, it was predicted that graphene interacts strongly with C(111) due to the interactions stemming from the π states on graphene layer and the carbon dangling bonds localized on the surface of diamond. As a result, the equilibrium adsorption distance of graphene layer to non-reconstructed C(111) is smaller (2.78-2.98 Å) and a larger band gap (0.4-0.8 eV) at the Dirac point of graphene were calculated[8-10].

It is also interesting to note that different charge-transfer complexes can be formed at the interfaces between graphene and diamond (111) surfaces by changing the surface terminations of diamond. It was found that cleaned C(111) and hydrogen-terminated C(111) could result in strong p-type and n-type doping of graphene, respectively. This can be explained by the Schottky-Mott model[15]. Since the workfunction of graphene (4.4 eV) is smaller than the workfunction of cleaned C(111) (4.9 eV) but larger than hydrogen-terminated C(111) (3.5 eV), electrons from graphene were transferred to the former while the latter transferred electrons to graphene[16]. Based on the linear dispersion relation close to the Dirac point of graphene[17], the charge carrier (hole or electron) concentration of doped graphene can be estimated by the equation 2.3:[18,19]

$$N_{h/e} = \frac{(\Delta E_D)^2}{\pi(\hbar v_F)^2} \qquad \text{(Equation 2.3)}$$

where ΔE_D is the Dirac point shift relative to the Fermi level. The carrier concentration of graphene adsorbed on cleaned C(111) and hydrogen-terminated C(111) were calculated to be 5 X 10^{12} cm^{-2} and 7 X 10^{12} cm^{-2}, respectively. These values are more than 2 orders of magnitude larger than intrinsic charge carrier density of graphene ($n= \pi k^2_B T^2/6\hbar v_F^2 = 6$ X 10^{10} cm^{-2})[20]. Hence, it can be anticipated by manipulating the surface work function of diamond, charge transfer at the graphene-diamond interface can be controlled effectively, presenting the graphene-diamond hybrid as a potential material for Schottky diodes[21-23].

2.2.2 Experimental investigation

The study of top-gated CVD graphene r.f. transistors with gate length scaled down to 40 nm (shorted gate length demonstrated on graphene r.f. devices so far), exhibited a maximum cut-off frequency of 155 GHz and the cut-off frequency was found to have an inverse relationship with the gate length[1]. Cut-off frequency (f_T) is one of the most important figure-of-merit in evaluating the performance of r.f. devices and is defined as the frequency at which the current gain becomes unity. In Fig. 2.5, the current gain, calculated from the high frequency scattering parameters (S) of graphene, is plotted against frequency (f); a f_T of 26 GHz is determined for the device that is 550 nm of length at room temperature. When length of the gate decreases to 40 nm, the f_T measured gave a value of 155 GHz, which is the highest cut-off frequency achieved on CVD graphene to date.

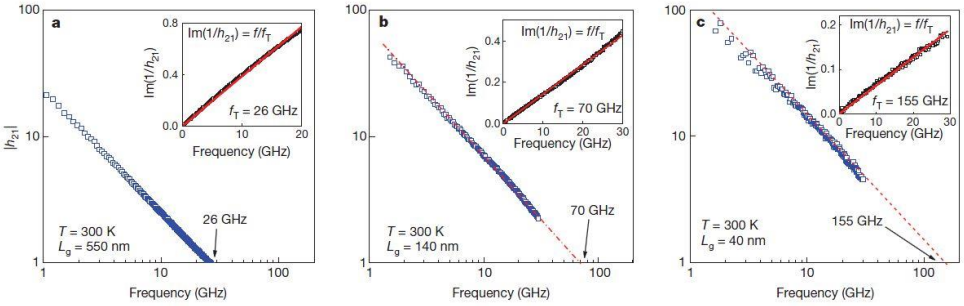

Figure 2.5 Cut-off frequencies for three different devices at room temperature. Small-signal current gain |h21| versus frequency for device with a gate length of (a) 550 nm, (b) 140 nm and (c) 40 nm at room temperature. Intercepts give the cut-off frequency as 26 GHz. 70 GHz and 155 GHz respectively. Reproduced with permission from ref. 1. Copyright (2011) Nature Publishing Group.

Moreover, unlike conventional semiconductor devices, where low-temperature performance is hampered by carrier freeze-out effects and showed strong temperature dependent interface trap density and occupation, the r.f. performace of the graphene device on DLC has little (if any) temperature dependence down to 4.3 K, providing a wider operation window (see Fig 2.6a and 2.6b). Gate biases from -8 to 0 V were applied with a fixed drain bias of 1.6 V in device with gate length of 550 nm. The current gain between 300 K to 4.3 K is found to be inversely related to *f*. This stability with temperature illustrates the high quality DLC substrate, in which the density of charge trap is low, a good candidate for use as the supporting platform in graphene electronics. Figure 2.6c illustrates that all devices of different gate length exhibit a well-defined 1/*f* dependence at room temperature. Unlike the typical carrier freeze out effects observed in Si MOSFETs at cryogenic temperatures[24], the consistent temperature independent results found open up new opportunities for future graphene r.f. applications, such as ultra-low noise or outer-space operations.

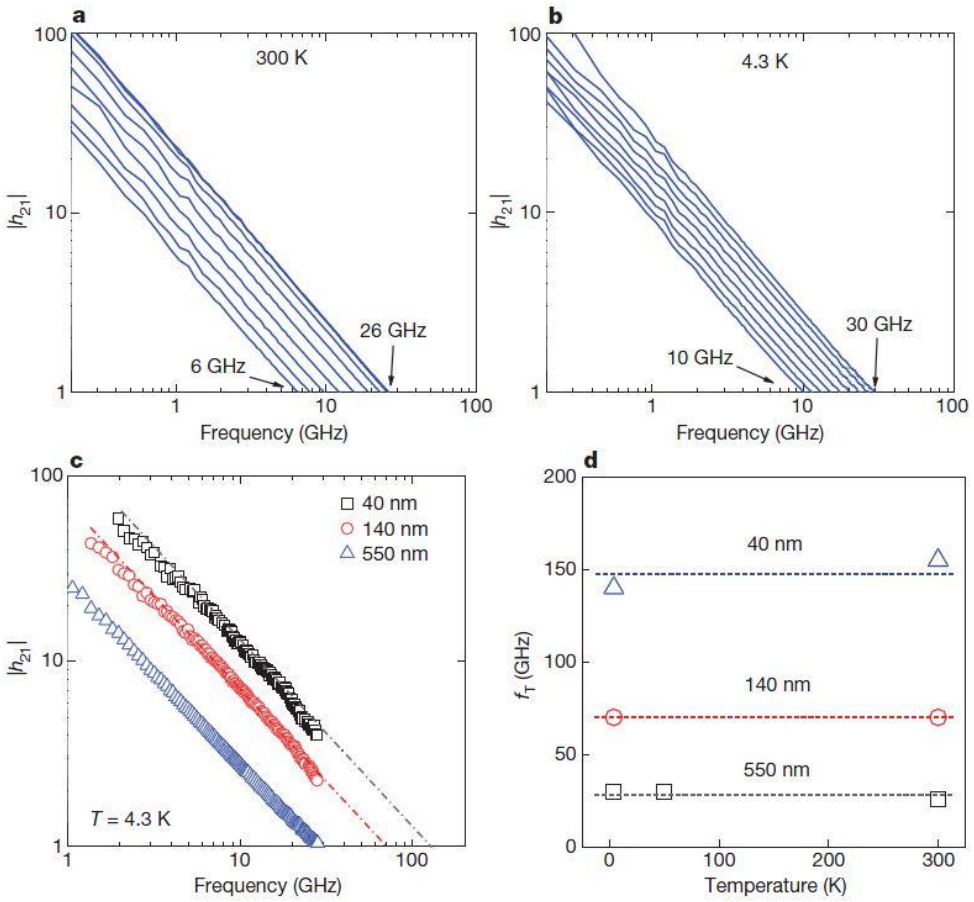

Figure 2.6 Temperature dependence of cut-off frequency for different devices. Current gain as a function of frequency at (a) 300 K, (b) 4.3 K. The gate length is 550nm, with V_{ds} of 1.6 V and with V_{gs} varying from -8 to 0 V. (c) Current gain versus frequency for three values of gate length (550 nm, 140 nm, 40 nm) at 4.3 K. The value of f_T is 28 GHz, 70 GHz and 140 GHz, respectively. (d) Summary plot of the temperature dependence of f_T for the three devices. Reproduced with permission from ref. 1. Copyright (2011) Nature Publishing Group.

Another demonstration of the new planar sp^2-on sp^3 technology (graphene on diamond devices) is the increased current capacity of over one magnitude as compared to typical graphene field-effect transistors and interconnects built on conventional SiO_2/Si substrates. Graphene has an intrinsic thermal conductivity (K) exceeding 2,000 W/mK at room temperature, making it an excellent material for heat conduction[25,26]. In a typical device (field effect transistor or interconnects), since most of the heat propagates

directly below the graphene channel, the underlying substrate is being made into a heat sink[27,28]. When graphene is deposited on SiO_2, the highly thermally resistive SiO_2 layer (K= 0.5-1.4 W/mK) becomes the thermal bottleneck in causing the breakdown of the device by resistive heating[29-32]. Since the thermal conductivity of diamond is ~2,000 W/mK at 300 K, it is a natural candidate to be used as the bottom dielectric in graphene electronics, as it is capable of efficient heat conduction. Synthetic diamond can be produced in a variety of forms ranging from ultrananocrystalline films with small grain size, D, and, correspondingly low K, to single crystalline diamond (SCD) with larger D than UNCD but has higher surface roughness, resulting in higher thermal boundary resistance. Hence studies of graphene on UNCD and SCD were undertaken to represent the extreme cases of in terms of D and K and their impact on the current capacity of graphene were evaluated. It should also be noted that the current carrying ability of graphene is dependent on the length, width, aspect ratio and quality of the graphene channel. For graphene-on-UNCD, a breakdown current of 5×10^8 A/cm^2 was obtained and found to be about 5 times higher than reference graphene-on-SiO_2/Si devices[33-35], while the maximum current achieved on SCD was as high as 1.8×10^9 A/cm^2.

Although diamond can potentially enhance the performance of graphene electronic devices, the major obstacles for the development of graphene on diamond technology include the high surface roughness of synthetic diamond, difficulty of visualization of graphene on diamond and also the problem with top-gate transistor fabrication[4]. Hence, a series of efforts has to be taken to overcome these challenges for commercialization of the planar sp^2-carbon on sp^3 carbon technology.

2.3 Graphene-diamond: Chemisorbed

2.3.1 Theoretical investigation

A graphene nanoribbon sandwiched between diamonds was investigated using first-principles total energy calculations based on density functional theory[36,37] (see Fig. 2.7). The results revealed that this system can serve as a spin-polarized conducting wire in the nano-scale electronic device circuits.

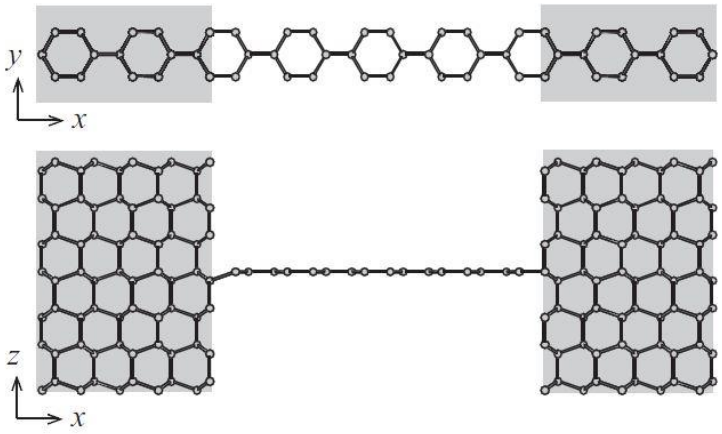

Figure 2.7 Top and side views of graphene-diamond hybrid structures. The shaded area denotes the diamond region. Reproduced with permission from ref. 5. Copyright (2012) American Institute of Physics.

The electronic band for graphene-diamond hybrid, exhibiting a metallic state with highly anisotropic dispersion relation is shown in Fig. 2.8. The blue and red circles denote electronic states of α-spin (majority spin) and β-spin (minority spin) states, respectively. Along the *y*-direction depicted in Fig. 2.8, most of the electron states possess substantial dispersion of a few eV, while

the states show completely flat dispersion relation in the *x* direction. Hence, the graphene-diamond hybrid assumes a one-dimensional metallic nature[5]. This nature is ascribed to the absence of π electrons in diamond, where the sp^3 carbon atoms of diamond effectively terminate the π electrons of the graphitic network in the system, rendering the hybrid a viable candidate for nano-scale conducting wire. Furthermore, through non-equilibrium molecular dynamics simulations performed, the thermal dissipation ability of diamond is further substantiated as heat generated in the graphene nanoribbon is efficiently conducted away through diamond[5] .

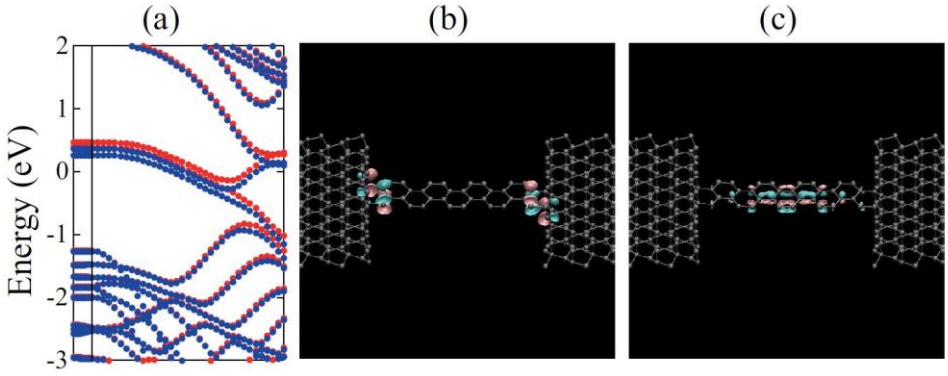

Figure 2.8 (a) Electronic band structure for the high-spin state of the graphene-diamond hybrid system. Energies are measure from that of the Fermi level. Blue and red circles denote the energy dispersion for majority and minority spins, respectively. (b) Distribution of the wavefunction at $J_{\parallel}$ point just above the Fermi level (c) and at the zone center Γ point. Color corresponds to the sign of the wave function Reproduced with permission from ref. 5. Copyright (2012) American Institute of Physics.

2.3.2 Experimental investigation

The interfacial bonding between graphene and nanodiamond leads to large negative magnetoresistance[6,38]. Firstly, the chemical fusion of ND to the graphene lattice created pockets of local defects with robust interfacial bonding. At the regions where ND was bonded, the atoms of graphene follow sp^3-like bonding, and these regions are the conduction bottlenecks for the percolating sp^2 graphene network, leading to insulating behaviour. Charge transport in this system involves a subtle interplay involving both the sp^2 and sp^3 regions. Besides the introduction of localization of charge carriers, detonated NDs are inherently a source of magnetism in the form of trace magnetic impurities. On top of the possibility of carbon magnetism from the attachment of graphene-diamond, it has been speculated that defects within the ND grains induce ferromagnetic order[39].

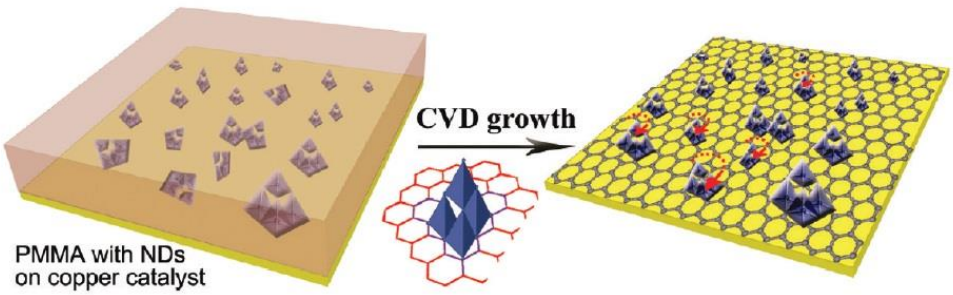

Figure 2.9 Schematic diagram for the growth of the hybrid of graphene and ND. Reproduced with permission from ref. 6. Copyright (2012) American Chemical Society.

2.4 Outlook

Owing to their unique properties, graphene and diamond have each established their respective niche as functional materials in various applications. By bringing the two materials together, the graphene-diamond hybrid has demonstrated to be a good candidate for high frequency r.f transistors. Current capacitiy of graphene on diamond has also been demonstrated to rival the conventional substrate SiO_2. What is more interesting is that through the bonding of the graphene sp^2 and diamond sp^3 interface that unexpected properties are observed. Through the fusion of graphene and diamond, spin and even ferromagentism can be injected into graphene. Investigation of the graphene-diamond interface is still at its infancy: it is likely that there are many more intriguing properties of the hybrid yet to be uncovered.

2.5 References

1 Wu, Y. *et al.* High-frequency, scaled graphene transistors on diamond-like carbon. *Nature* **472**, 74-78 (2011).

2 Meric, I. *et al.* Current saturation in zero-bandgap, top-gated graphene field-effect transistors. *Nature Nanotechnology* **3**, 654-659 (2008).

3 Robertson, J. Diamond-like amorphous carbon. *Materials Science and Engineering: R: Reports* **37** 129-281 (2002).

4 Yu, J., Liu, G., Sumant, A. V., Goyal, V. & Balandin, A. A. Graphene-on-diamond devices with increased current-carrying capacity: Carbon sp^2-on-sp^3 technology. *Nano Letters* **12**, 1603-1608 (2012).

5 Shiga, T. *et al.* Graphene-diamond hybrid structure as spin-polarized conducting wire with thermally efficient heat sinks. *Applied Physics Letters* **100** 233101 (2012).

6 Wang, Y. *et al.* Electronic properties of nanodiamond decorated graphene. *ACS Nano* **6**, 1018-1025 (2012).

7 Tzeng, Y., Chen, W. L., Wu, C., Lo, J.-Y. & Li, C.-Y. The synthesis of graphene nanowalls on a diamond film on a silicon substrate by direct-current plasma chemical vapor deposition. *Carbon* **53**, 120-129 (2013).

8 Ma, Y., Dai, Y., Guo, M. & Huang, B. Graphene-diamond interface: Gap opening and electronic spin injection. *Physical Review B - Condensed Matter and Materials Physics* **85** 235448 (2012).

9 Pandey, K. C. New dimerized-chain model for the reconstruction of the diamond (111)-(2 × 1) surface. *Physical Review B* **25**, 4338-4341 (1982).

10 Iarlori, S., Galli, G., Gygi, F., Parrinello, M. & Tosatti, E. Reconstruction of the diamond (111) surface. *Physical Review Letters* **69**, 2947-2950 (1992).

11 Tuinstra, F. & Koenig, J. L. RAMAN SPECTRUM OF GRAPHITE. *Journal of Chemical Physics* **53**, 1126-1130 (1970).

12 Baskin, Y. & Meyer, L. Lattice Constants of Graphite at Low Temperatures. *Physical Review* **100**, 544-544 (1955).

13 Zacharia, R., Ulbricht, H. & Hertel, T. Interlayer cohesive energy of graphite from thermal desorption of polyaromatic hydrocarbons. *Physical Review B* **69**, 155406 (2004).

14 Hu, W., Li, Z. & Yang, J. Diamond as an inert substrate of graphene. *Journal of Chemical Physics* **138** 54701 (2013).

15 Bardeen, J. Surface States and Rectification at a Metal Semi-Conductor Contact. *Physical Review* **71**, 717-727 (1947).

16 Sque, S. J., Jones, R. & Briddon, P. R. Structure, electronics, and interaction of hydrogen and oxygen on diamond surfaces. *Physical Review B* **73**, 085313 (2006).

17 Castro Neto, A. H., Guinea, F., Peres, N. M. R., Novoselov, K. S. & Geim, A. K. The electronic properties of graphene. *Reviews of Modern Physics* **81**, 109-162 (2009).

18 Chen, Z. *et al.* Surface transfer hole doping of epitaxial graphene using MoO_3 thin film. *Applied Physics Letters* **96** 213104 (2010).

19 Du, A. *et al.* Hybrid graphene/titania nanocomposite: Interface charge transfer, hole doping, and sensitization for visible light response. *Journal of Physical Chemistry Letters* **2**, 894-899 (2011).

20 Ristein, J., Mammadov, S. & Seyller, T. Origin of Doping in Quasi-Free-Standing Graphene on Silicon Carbide. *Physical Review Letters* **108**, 246104 (2012).

21 Tongay, S., Schumann, T. & Hebard, A. F. Graphite based Schottky diodes formed on Si, GaAs, and 4H-SiC substrates. *Applied Physics Letters* **95** 222103 (2009).

22 Chen, C. C., Aykol, M., Chang, C. C., Levi, A. F. J. & Cronin, S. B. Graphene-silicon Schottky diodes. *Nano Letters* **11**, 1863-1867 (2011).

23 Yang, H. *et al.* Graphene barristor, a triode device with a gate-controlled Schottky barrier. *Science* **336**, 1140-1143 (2012).

24 Sze, S. M. & Ng, K. K. in *Physics of Semiconductor Devices* 5-75 (John Wiley & Sons, Inc., 2006).

25 Ghosh, S. *et al.* Dimensional crossover of thermal transport in few-layer graphene. *Nature Materials* **9**, 555-558 (2010).

26 Balandin, A. A. Thermal properties of graphene and nanostructured carbon materials. *Nature Materials* **10**, 569-581 (2011).

27 Freitag, M. *et al.* Energy dissipation in graphene field-effect transistors. *Nano Letters* **9**, 1883-1888 (2009).

28 Subrina, S., Kotchetkov, D. & Balandin, A. A. Heat removal in silicon-on-insulator integrated circuits with graphene lateral heat spreaders. *IEEE Electron Device Letters* **30**, 1281-1283 (2009).

29 Collins, P. G., Hersam, M., Arnold, M., Martel, R. & Avouris, P. Current Saturation and Electrical Breakdown in Multiwalled Carbon Nanotubes. *Physical Review Letters* **86**, 3128-3131 (2001).

30 Tsutsui, M., Taninouchi, Y. K., Kurokawa, S. & Sakai, A. Electrical breakdown of short multiwalled carbon nanotubes. *Journal of Applied Physics* **100** 094302 (2006).

31 Huang, J. Y. *et al.* Atomic-scale imaging of wall-by-wall breakdown and concurrent transport measurements in multiwall carbon nanotubes. *Physical Review Letters* **94** 236802 (2005).

32 Frank, S., Poncharal, P., Wang, Z. L. & De Heer, W. A. Carbon nanotube quantum resistors. *Science* **280**, 1744-1746 (1998).

33 Murali, R., Yang, Y., Brenner, K., Beck, T. & Meindl, J. D. Breakdown current density of graphene nanoribbons. *Applied Physics Letters* **94** 243114 (2009).

34 Yu, T., Lee, E. K., Briggs, B., Nagabhirava, B. & Yu, B. Bilayer graphene system: Current-induced reliability limit. *IEEE Electron Device Letters* **31**, 1155-1157 (2010).

35 Lee, K. J., Chandrakasan, A. P. & Kong, J. Breakdown current density of CVD-grown multilayer graphene interconnects. *IEEE Electron Device Letters* **32**, 557-559 (2011).

36 Hohenberg, P. & Kohn, W. Inhomogeneous Electron Gas. *Physical Review* **136**, B864-B871 (1964).

37 Kohn, W. & Sham, L. J. Self-Consistent Equations Including Exchange and Correlation Effects. *Physical Review* **140**, A1133-A1138 (1965).

38 Lim, C. H. Y. X. *et al.* A hydrothermal anvil made of graphene nanobubbles on diamond. *Nature Communications* **4** 1556 (2013).

39 Talapatra, S. *et al.* Irradiation-Induced Magnetism in Carbon Nanostructures. *Physical Review Letters* **95**, 097201 (2005).

Chapter 3

Experimental Techniques

3.1 Introduction

This chapter examines the techniques employed for the characterization of the works presented in this dissertation. Two main groups of techniques were employed for surface characterization of materials, namely Microscopy and Spectroscopy. Under microscopy, atomic force microscopy (AFM) and scanning electron microscopy (SEM) are discussed while for the branch of spectroscopy, special attention was devoted to Raman spectroscopy, X-ray photoelectron spectroscopy (XPS), Ultra-violet photoelectron spectroscopy (UPS), UV-visible spectroscopy (UV/vis spectroscopy) and Infra-red spectroscopy (IR Spectroscopy),

3.2 Microscopy

Microscopy is the technique of using microscopes to view objects, which dimensions are not within the resolution of the unaided eye. There are three classes of microscopy techniques, namely optical, electron and scanning probe microscopy. While optical and electron microscopy involve the diffraction, reflection, or refraction of electromagnetic radiation interacting

with the sample to produce an image, scanning probe microscopy relies on the interaction between a scanning probe or sharp tip and the surface of the object.

3.2.1 Atomic force microscopy (AFM)

Atomic force microscopy (AFM) relies on the van der Waals interaction between the surface of the samples and an atomically sharp tip for imaging[1]. The typical configuration of the atomic force microscope is shown in Fig. 3.1, which includes a pyramid-shaped pointed tip located at the end of the cantilever, a piezoscanner, a laser source and a position sensitive photo detector, commonly known as the PSPD.

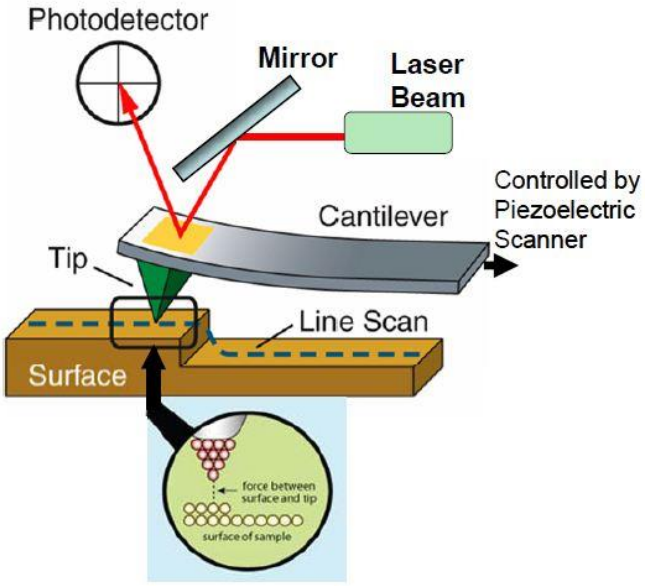

Figure 3.1 Schematic drawing of a typical AFM configuration and setup.

The atomically sharp tip is mounted on a cantilever and the tip is brought into proximity of the sample surface and forces that arise from the interaction between the tip and the sample will cause a deflection of the cantilever according to Hooke's Law. The resultant deflections of the cantilever may be monitored using a laser beam which is reflected from the back of the cantilever onto the PSPD.

There are various modes of AFM and can be categorized accordingly to the strength and nature of interaction force between the tip and the sample surface. Non-contact or tapping modes operate when the tip-sample separation is relatively large, such that there is no overlap in their electron clouds. Attractive forces are dominant in these modes of operation and the cantilever is typically externally oscillated close to its fundamental resonance frequency. Variations in tip-sample distances (forces) will alter the resonant frequency of the tip in tapping mode and changes the resultant resonance frequency, which will correlate to the forces in action used for generating topographic images of the sample surface. Samples which are soft and easily damaged, they are usually measured in the non-contact mode. For contact mode, the tip-sample separation needs to fall in the dimension of a chemical bonding length. In this mode of operation, repulsion forces between the tip and sample dominates. In contact mode, the deflection of the cantilever is sensed and compared in a DC feedback amplifier to some desired value of deflection. When the deflection measured is different from the desired value, the feedback amplifier applies a voltage to the piezo to adjust the sample relative to the cantilever to restore it to the desired value of deflection. Hence, the resulting voltage is used as a measurement of the sample topography. A major problem associated with

contact mode is the excessive tracking forces applied by the probe to the sample. Therefore, samples which are easily damaged, for example polymers, should not be analyzed by contact mode AFM.

3.2.2 Scanning Electron Microscopy

Scanning electron microscopy relies on the interaction of electrons in the sample with a focused high energy electron beam to produce an image. The electron beam is generally scanned in a raster fashion and the position of the beam is combined with the detected signal to generate information about the sample's external morphology (texture), chemical composition and crystalline structure and orientation of materials that makes up the sample. Figure 3.2 shows the typical setup for a scanning electron microscope (SEM).

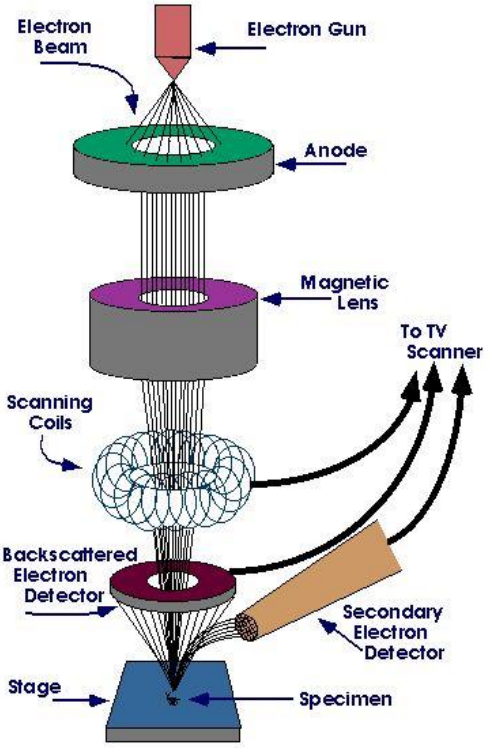

Figure 3.2 Schematic representation of the instrumentation of scanning electron microscopy.

Accelerated electrons in SEM carry significant amounts of kinetic energy and this energy is dissipated as various signals upon electron-sample interaction due to the deceleration of incident electrons. Different types of electron images can be generated and the two most commonly used are secondary electron image (SEI) and backscattered electron image (BEI). SEI is used for imaging fracture surfaces and is capable of producing high resolution images. While the brightness of the image in BEI, is dependent on the atomic number of the specimen, it can be used for the atomic mapping of the specimen surface. Energy-dispersive x-ray microanalysis (EDX) is typically complementary to SEM as it enables the determination of elemental composition of features captured. Upon the interaction of the electron beams

with the sample, x-ray will be generated. Each element typically emits at characteristic energies, thus by measuring the emitted energies, identification and quantification of the elements can be made possible.

3.3 Spectroscopy

Spectroscopy refers to the study of interaction between matter and electromagnetic radiation. Historically, it relates the study of visible light dispersed accordingly to its wavelength by a prism. Subsequently, the concept was expanded and encompassed any interaction of mater with radiative energy as a function of its wavelength or frequency.

3.3.1 X-ray photoelectron spectroscopy (XPS)

X-ray photoelectron spectroscopy (XPS) is one of the most versatile spectroscopic techniques used for studying the elemental composition, empirical formula, chemical state and electronic state of the elements within the specimen[2]. The working principle of XPS relies on the well-known photoelectric effect, that can be considered in terms of a three step model[3]: X-ray excitation of the core electron from the ground state to the final state, transfer of the electron to the surface and the escape of the electron into the vacuum from the surface of the specimen as depicted in Fig 3.3. In other

words, the X-ray photon is absorbed by an atom in a molecule of a solid, leading to ionization and the emission of an inner shell electron.

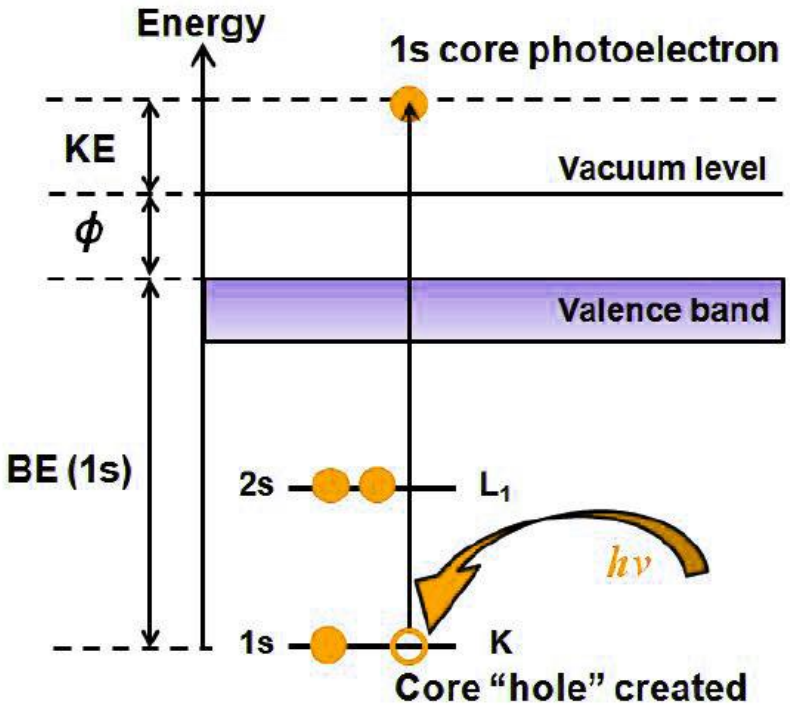

Figure 3.3 Schematic drawing of the X-ray photoemission process of core level electrons.

The X-ray photon energy ($h\nu$) must be greater than the work function of the material for the induction of electron emission from the core levels of surface atoms into the vacuum. According to the law of conversation of energy, the kinetic energy (E_{KE}) of the photoelectron is related to incident energy ($h\nu$), binding (E_{BE}) energy and work function of the spectrometer (ϕ) by the following equation:

$$E_{KE} = h\nu - E_{BE} - \phi \qquad \text{(Equation 3.1)}$$

The work function of a material is defined as the minimum energy required to remove an electron from the highest occupied energy level to the vacuum level. Since each element has its well-defined core level energy, for a fixed *hv*, photoelectrons of characteristic E_{KE} will be emitted and the detected photoelectron can be used to calculate the E_{BE} as *hv* and ϕ are known values. As such, E_{BE} obtained can be used for chemical identification. Besides qualitative determination of the chemical composition of the specimen, quantification can be carried out through the comparison of peak intensity after sensitivity correction of atoms is performed. Furthermore, the chemical shifts (binding energy shifts) is correlated with the chemical environment of the atom and its oxidation state of the surface species[4].

As such, XPS is often used for the characterization of diamond and graphene for the determination of the relative content of carbon atoms bound to oxygen. With deconvolution of the XPS C1s and O1s spectra, the percentage of C-C, C-O and C=O can be determined due to the binding energy that they exhibit respectively.

3.3.2 Ultra-violet photoelectron spectroscopy (UPS)

In Ultra-violet photoelectron spectroscopy (UPS), the source of radiation is typically a noble gas discharge lamp (e.g. He-discharge lamp emitting He I energy of 21.2 eV). In contrast to XPS, this source employed is only capable of ionizing electrons from the outermost levels of the atoms – the valence band. One of the benefits of UPS is that the line width of the UV

source is much narrower as compared to x-ray source. Although valence band structures can also be studied using XPS, the photo-ionization cross section of valence electrons using ultra-violet light is much higher and detailed information such as individual electronic orbital and highest occupied molecular orbital (HOMO) can be obtained. Moreover, UPS is particularly surface sensitive (to 10 nm depth), as the emitted photoelectrons are shorter in range as compared to X-rays. UPS has been mainly used for the studying of electronic structure of solids-using polarized incident light coupled with variable angle of detection, angle resolved UPS (ARUPS) studies that enable the mapping of complete band structure in the k-space. At the same time, probing of the adsorbed species binding interaction and orientation with the specimen surface can be performed.

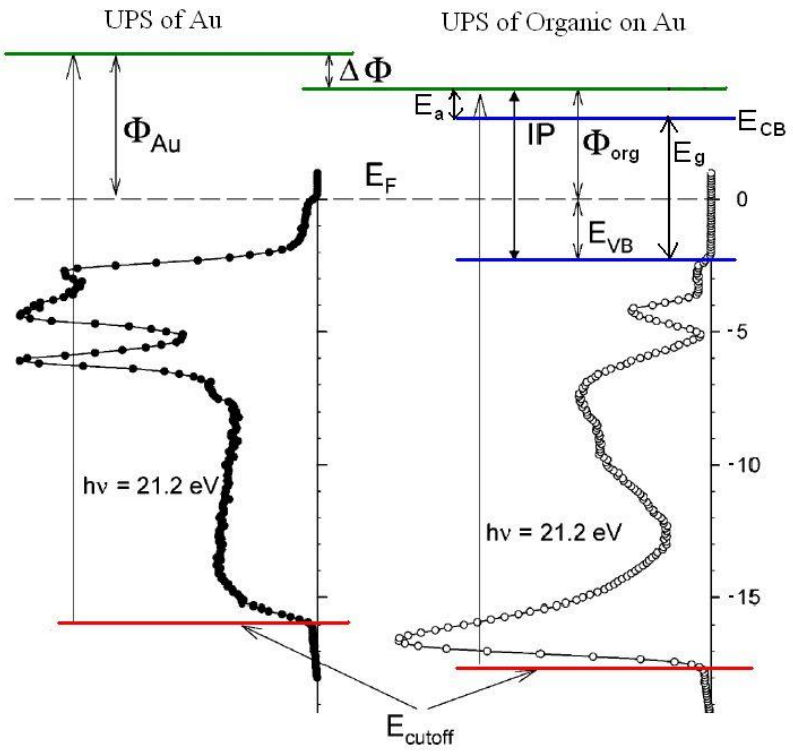

Figure 3.4 Schematic drawing of parameters from UPS and energy alignment of gold substrate and organic layer.

As illustrated in Fig 3.4, UPS can be used for the calculation of the work function (ϕ) and subsequently used for the determination of HOMO of a material by the use of the following equation:

$$\phi = h\upsilon - W \qquad \text{(Equation 3.2)}$$

Where $h\upsilon$ is the energy of the UV source and W is the spectrum width measured (energy difference between the Fermi level (E_F) and the secondary electron cut-off). The full width of the photoelectron spectrum (from the highest kinetic energy/lowest binding energy point to the lowest kinetic energy cutoff) is measured and subtracted from $h\upsilon$ to give ϕ. Since the ionization potential energy (IP) is related to ϕ by:

$$E_{VB} = \phi - IP \qquad \text{(Equation 3.3)}$$

HOMO (valence band maximum, E_{VB}) of the sample can be calculated according to the above equation. If the bandgap, E_g, of the sample is known, the conduction band minimum (E_{CB}) can be calculated by:

$$E_{CB} = E_g + E_{VB} \qquad \text{(Equation 3.4)}$$

The electron affinity, χ can be found by:

$$\chi = \phi - E_{CB} \qquad \text{(Equation 3.5)}$$

In fact, the energy level alignment of an overlaying material on a substrate can be drawn since the Fermi level for the two materials must align when in electrical contact. The difference in their work function is due to the interfacial dipole set up between the two materials. Hence, the relationship between the occupied levels at the heterojunction can be measured, both in with respective to the Fermi level and vacuum level. Typically when UPS is carried out, a negative bias is applied to the sample for the separation of its low energy cutoff from the response of the spectrometer.

3.3.3 Raman Spectroscopy

Predominantly, light is scattered elastically upon contact with air molecules, this mode of scattering is named Rayleigh scattering[5]. However, it is also possible for the incident photons to be scattered inelastically. In other words, the incident photons, upon interaction with the molecules in the

specimen, acquire or lose energy such that the resultant scattered photons are shifted in frequency and the change in energy (ΔE) corresponds to a vibrational and/or rotational transition of the specimen; this effect is known as Raman scattering. Raman spectroscopy is named after Sir C.V. Raman, who discovered this phenomenon in 1928 and was awarded the Nobel Prize for Physics in 1930. If the molecules gains energy, the photon scattered will be at a lower frequency than the incident radiation. This is known as Stokes scattering. Anti-Stokes corresponds to molecules which are originally on the vibrational excited state and the photon scattered will be at a higher frequency relative to the incident light. Since the ground vibrational state is more densely populated at room temperature as compared to a vibrationally excited state, Stokes lines detected are dominantly of higher intensity than anti-Stokes lines[6] (see Fig 3.5).

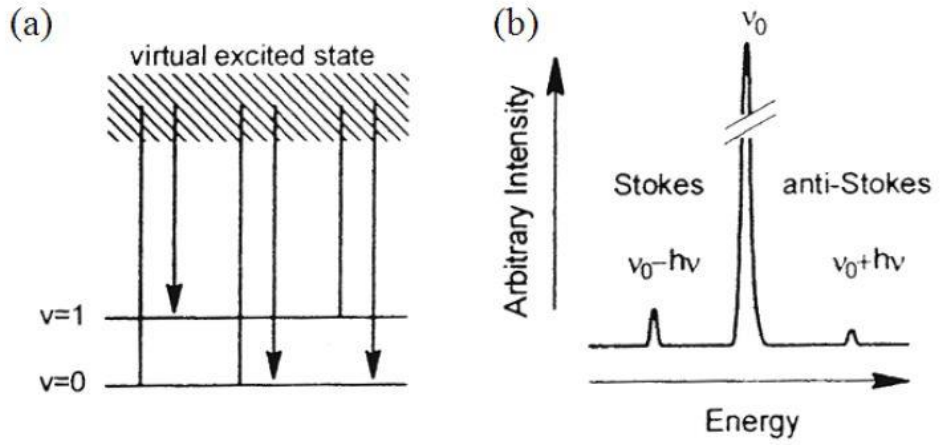

Figure 3.5 (a) Energy levels involved in Raman Spectroscopy. (b) Raman spectrum showing Rayleigh, Stokes, Anti-stokes band.

Raman spectroscopy can be used to characterize both diamond and graphene as their respective peak positions are well-defined and do not

typically overlap. Natural diamond exhibits one main Raman active vibration which manifest itself as a sharp and intense first order peak in the Raman spectrum residing at ~1,332 cm^{-1} and also a weak second order peak[7] at ~2,750 cm^{-1} (see Fig 3.6). The band width of the first order peak of diamond can be used to assess the quality of the crystal. Typically, the first order peak of a pristine monocrystalline (type IIa) diamond can be fitted well with a Lorentzian line shape and its full width at half maximum is approximately ≤ 2 cm^{-1}.

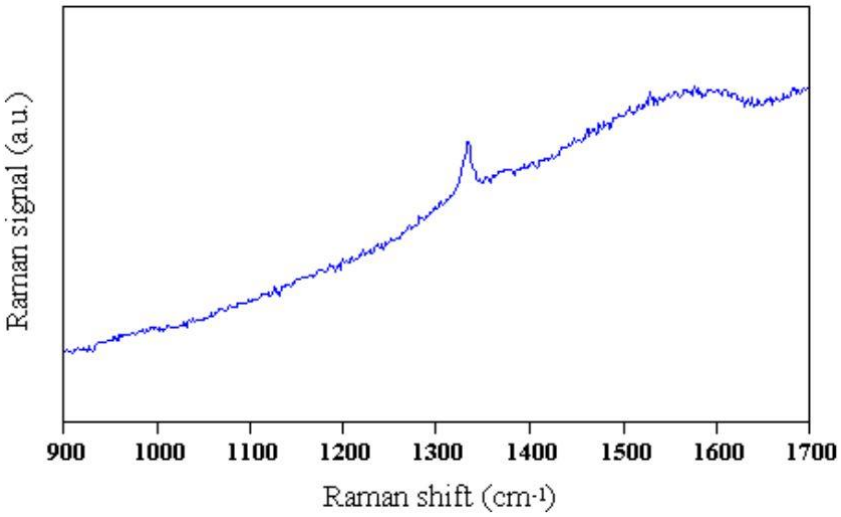

Figure 3.6 Raman spectrum of diamond (type IIa), showing the main Raman active mode at ~ 1,332 cm-1 (excited with 514.5 nm laser).

During the chemical vapor deposition growth of diamond, other forms of carbon may also be incorporated into the diamond film. These carbon forms include graphitic[8,9] and/ or amorphous carbon[9,10]. Both graphite and amorphous carbon have Raman scattering efficiencies greater than diamond, in other words, when identical atoms of the three carbon forms are sampled, diamond would yield a much weaker signal as compared to graphite and

amorphous carbon. The scattering efficiency ratios, relative to diamond have been reported to be ~50 times for graphite[11] and ~233 times for amorphous carbon[12], when measured at 514.5 nm. Raman spectroscopy is particularly useful in characterizing graphene in terms of its structure, number of layers[13], doping concentration[14] and the band position also enables the determination of strain[15] (will be discussed in greater detail in Chapter 5) in graphene lattice. The two most intense characteristic peaks of graphene are the G peak at ca. 1580 cm^{-1} and 2D peak at ca. 2700 cm^{-1} which corresponds to the in-plane vibration of sp^2 carbon atoms and the second order of zone-boundary phonons at the K and Δk points in the Brillouin zone respectively. In the presence of defects, disorder in the crystalline lattice of graphene, the symmetry forbidden peak can be observed at ~1,350 cm^{-1} [13,16]. Hence, Raman spectroscopy is a useful tool in examining the quality of graphene sheets.

3.3.4 Infrared spectroscopy (IR spectroscopy)

Infrared spectroscopy (IR spectroscopy) is a simple and reliable technique widely used in both organic and inorganic chemistry. As the name of the technique suggest, it uses the infrared region of the electromagnetic spectrum and it is the absorption measurement of different IR frequencies by a sample positioned in the path of the IR beam. The covalent bonds in molecules can be liken to stiff springs that can undergo stretching and bending and organic compounds will absorb infrared radiation that corresponds in energy to these vibrations. . In order for a vibrational mode in a molecule to be “IR

active", there must be a change in its dipole. IR spectroscopy is a non-destructive method that can be used for the determination of functional groups in organic materials, molecular composition of surfaces and identification of chromatographic effluents since different functional groups absorb characteristic frequencies of IR radiation at different intensities. In addition, quantification of compounds in mixture, determination of molecular conformation (structural isomers), stereochemistry (geometrical isomers) and molecular orientation (polymers and solutions) can be performed using IR spectroscopy.

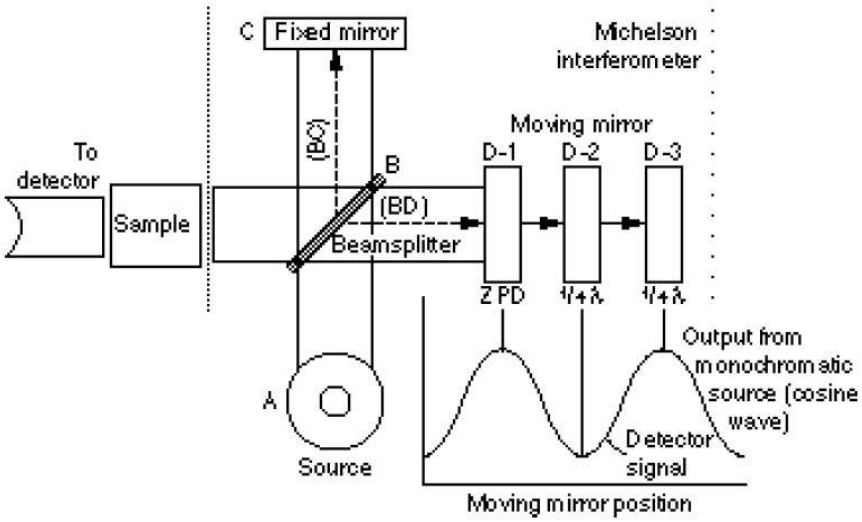

Figure 3.7 Optical layout of a typical FTIR spectrometer.

Fourier transform infrared (FTIR) spectroscopy is a technique that allows the recording of infrared spectra. Using this method, "interferograms" are recorded and these signals actually correspond to the output of light as a function of mirror position. In the FTIR spectrometer, infrared light is guided through an interferometer and then through the sample. A moving mirror

inside this setup alters the distribution of light that passes through the interferometer and interferograms can be obtained (see Fig 3.7). These measured interferograms are then subjected to a data-processing technique, known as Fourier transform in converting the light output as a function of infrared wavelength.

3.35 Ultraviolet-visible spectroscopy (UV/vis spectroscopy)

Similar to IR spectroscopy, Ultraviolet-visible spectroscopy (UV/vis spectroscopy) is also a technique that relies on the absorbance (or reflectance) of electromagnetic radiation but the energy range of absorption spans from ultraviolet (UV) to visible (vis) region of the electromagnetic spectrum[6]. In UV/vis spectroscopy, the π electrons or non-bonding electrons absorb energy in the UV or vis range and gets excited to higher anti-bonding molecular orbitals, when sample molecules are exposed to light having an energy that matches a possible electronic transition within the molecule. Since the transition occurs between electronic levels, UV/vis spectroscopy is sometimes known as “electronic spectroscopy”. Figure 3.8 shows the various kinds of electronic excitation that may occur in an organic molecule.

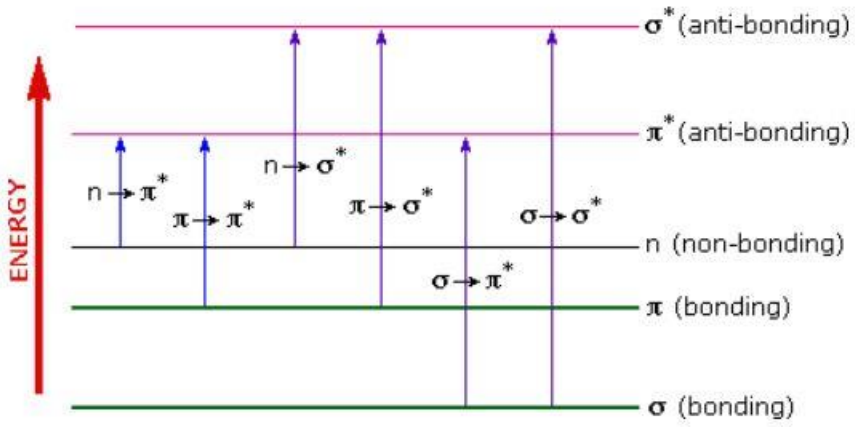

Figure 3.8 Possible electronic transitions in an organic molecule.

Absorbance of the sample in UV/vis spectroscopy follows the Beer-Lambert law.

$$A = \varepsilon cl = log_{10} (I_0/I) \qquad \text{(Equation 3.6)}$$

Where A is the absorbance, ε is the molar absorption coefficient, c is the concentration of the molar concentration of the absorbing species, l is the path length in centimeters, I_0 and I correspond to the intensity of the light transmitted after passing through reference and the sample at a particular wavelength respectively. Hence the absorbance of a specimen is directly proportional to the concentration of the absorbing species and path length (see equation 3.4). Thus, for a fixed path length, UV/vis spectroscopy can be used to determine the concentration of the absorbing species in the specimen.

Typically, molecular moieties possessing π electron functions and heteroatoms possessing non-bonding valence-shell electron pairs are likely to absorb light in the UV-vis range. These light absorbing functional groups are known as chromophores. Some common chromophores which can be identified using UV-vis spectroscopy are listed in the table below.

Table 3.1 Some typical chromophores and their respective electronic transitions.

Chromophore	Example	Excitation	λmax, nm	ε	Solvent
C=C	Ethene	π →π*	171	15,000	Hexane
C≡C	1-Hexyne	π →π*	180	10,000	Hexane
C=O	Ethanal	n→π*	290	15	Hexane
		π →π*	180	10,000	Hexane
N=O	Nitromethane	n→π*	275	17	Ethanol
		π →π*	200	5,000	Ethanol
C-X X=Br, I	Methyl bromide	n→σ*	205	200	Hexane
	Methyl Iodide	n→σ*	255	360	Hexane

UV/vis spectroscopy is useful in the characterization of graphene derivatives, for example graphene oxide as the typical UV-vis spectrum of graphene oxide absorbs at ~230 nm and has a shoulder peak at ~300 nm. These 2 absorption peaks correspond to the π→π* transition of the C=C bonds and the n→π* transition of the C=O bond. As such, quantification of the sample can be made following chemical treatments.

3.4 References

1 Hansma, P. K., Elings, V. B., Marti, O. & Bracker, C. E. Scanning tunneling microscopy and atomic force microscopy: Application to biology and technology. *Science* **241**, 209-216 (1988).

2 Briggs, D. Handbook of X-ray Photoelectron Spectroscopy C. D. Wanger, W. M. Riggs, L. E. Davis, J. F. Moulder and G. E.Muilenberg Perkin-Elmer Corp., Physical Electronics Division, Eden Prairie, Minnesota, USA, 1979. 190 -195 pp.. *Surface and Interface Analysis* **3**, v-v, doi:10.1002/sia.740030412 (1981).

3 Nordling, C., Sokolowski, E. & Siegbahn, K. Precision Method for Obtaining Absolute Values of Atomic Binding Energies. *Physical Review* **105**, 1676-1677 (1957).

4 Egelhoff Jr, W. F. Core-level binding-energy shifts at surfaces and in solids. *Surface Science Reports* **6**, 253-415 (1987).

5 Banwell, C. N. & McCash, E. M. *Fundamentals of molecular spectroscopy*. (McGraw-Hill, 1995).

6 Brisdon, A. K. *Zz Inorganic Spectroscopic Methods Ocp*. (Oxford University Press, 1998).

7 Solin, S. A. & Ramdas, A. K. Raman spectrum of diamond. *Physical Review B* **1**, 1687-1698 (1970).

8 Zhu, W., Randall, C. A., Badzian, A. R. & Messier, R. Graphite formation in diamond film deposition. *Journal of Vacuum Science & Technology A: Vacuum, Surfaces, and Films* **7**, 2315-2324 (1989).

9 Fayette, L., Marcus, B., Mermoux, M., Abello, L. & Lucazeau, G. In-situ Raman investigation of diamond films during growth and etching processes. *Diamond and Related Materials* **3**, 438-442 (1994).

10 Nemanich, R. J., Glass, J. T., Lucovsky, G. & Shroder, R. E. Raman scattering characterization of carbon bonding in diamond and

diamondlike thin films. *Journal of Vacuum Science & Technology A: Vacuum, Surfaces, and Films* **6**, 1783-1787 (1988).

11 Wada, N. & Solin, S. A. Raman efficiency measurements of graphite. *Physica B+C* **105**, 353-356 (1981).

12 Sails, S. R., Gardiner, D. J., Bowden, M., Savage, J. & Rodway, D. Monitoring the quality of diamond films using Raman spectra excited at 514.5 nm and 633 nm. *Diamond and Related Materials* **5**, 589-591 (1996).

13 Ferrari, A. C. *et al.* Raman Spectrum of Graphene and Graphene Layers. *Physical Review Letters* **97**, 187401 (2006).

14 Das, A. *et al.* Monitoring dopants by Raman scattering in an electrochemically top-gated graphene transistor. *Nature Nanotechnology* **3**, 210-215 (2008).

15 Zabel, J. *et al.* Raman spectroscopy of graphene and bilayer under biaxial strain: Bubbles and balloons. *Nano Letters* **12**, 617-621 (2012).

16 Casiraghi, C. *et al.* Raman spectroscopy of graphene edges. *Nano Letters* **9**, 1433-1441 (2009).

Chapter 4

Charge transfer properties of the graphene-diamond hybrid: Electrical charge transport and photovoltaic

Abstract:

Using surface spectroscopy and transport measurements, we evaluate the effect of substrate charged impurities on the mobility of CVD graphene. Diamond is investigated as a novel platform for graphene electronics due to its non-polar nature. Due to its non-polar nature, it was thought to reduce the inherent amount of charge impurities relative to SiO_x used conventionally. In addition, it also serves as an unconventional platform for the investigation of charge scattering mechanisms in graphene. We observe a non-monotonic temperature dependence of resistance for chemical vapor deposition (CVD) graphene transferred on oxygen- and hydrogen-terminated diamond substrates. The important role for surface optical phonons in determining the high-temperature metallic behavior of graphene is confirmed since higher activation energies of SO phonons are associated with the oxygen-terminated diamond surface in comparison to SiO_x.

To construct a hybrid diamond-graphene electrode, we coupled exfoliated graphene flakes to boron doped diamond (BDD) via molecular wire to enable efficient charge transfer. Electrical conductivity of the diamond electrode modified with graphene can be improved with almost no or minimal

compromise on its optical transparency as graphene absorbs *ca.* 2.3% of visible light.

4.1 Modulation of graphene charge transport by diamond substrates

4.1.1 Introduction

Owing to its high intrinsic carrier mobility, graphene has attracted significant attention in recent years[1-4]. In particular, its transport properties have been the key focus of research efforts directed both at the fundamental properties of this system as well as to explore its potential for novel electronic applications. The development of large-area chemical vapor deposited (CVD) graphene was a key step toward the realization of commercialized graphene electronics[5]. The highest intrinsic mobility (μ) of graphene that has been reported exceeds 20 $m^2V^{-1}s^{-1}$ at room temperature[6,7]. Yet, such values are not easily demonstrated on substrate-supported graphene due to the presence of several scattering mechanisms which limit the mobility. Therefore, it is no surprise that the origin of electron scattering mechanisms has been the focus of intensive experimental and theoretical investigations[8,9].

While the charge scattering mechanisms in graphene have been the subject of several experimental investigations, there is a significant lack of consensus on the identification of these scatterers[7,10]. While there exists an agreement on the density-independent contribution of acoustic phonons that contribute to the metallic behavior at high temperature, this electron-phonon

coupling is rather weak and adds only 30 Ω to the room temperature resistivity[1,6]. At low temperatures, there is a quantum suppression of the acoustic phonon scattering and this was experimentally verified recently[11]. The more important contribution to high temperature metallic behavior was originally attributed to surface optical (SO) phonons from the underlying substrate[6]. In the case of SiO_x substrates which are most commonly used in graphene transport experiments, these SO phonons lead to a significant increase in resistance at T > 200 K. This temperature scale is determined by the energy required for the surface lattice vibrations for a given substrate. Subsequent experimental[7] and theoretical[9] work pointed out that a similar temperature dependent metallic behavior can instead be explained by the local out-of-plane deformations of the graphene lattice in the form of quenched-ripples. These deformations are based on the assumption of a weak coupling of the graphene lattice to the substrate and are therefore contradictory to the concept of scattering introduced by substrate SO phonons. In this chapter, transport studies were carried on graphene supported on several different substrates in order to clarify the dominant scatterer that leads to metallic behavior of resistivity.

Furthermore, there is also a lack of consensus on the dominant charge scattering factor for the overall mobility in the typical low mobility samples. Charged impurities on the underlying substrate and on the graphene sheet have been considered as the dominant factor and these break up the energy landscape with the formation of electron-hole puddles[12]. In particular, for CVD graphene charged impurities have been recently attributed to cause the low temperature insulating behavior from a thermally activated process within

the puddles[10]. At the same time, it is well known that defects are usually present in CVD graphene. Experiments involving the controlled introduction of defects can also capture the low temperature insulating behavior[13]. The above lack of consensus on the nature of charge scatterers motivates us to investigate the transport properties of graphene transferred on substrates with different surface properties.

In this work, we seek to modulate the charge transport of graphene by tuning the surface terminations of diamond substrate. Diamond also serves as a novel platform for the investigation of charge scattering mechanism. By oxidizing the diamond substrate, it can be made to acquire higher charge density with simultaneous tuning of its surface phonon frequency[14,15]. The ease of manipulating surface termination groups of diamond and the tunability of its SO phonons makes it a versatile platform for transport studies.

4.1.2 Materials and methods

4.1.2.1 Surface preparation of diamond

Undoped single crystalline diamonds of facets (100) type IIa were purchased from element six. Acid and plasma cleaning were used for all diamond samples. Metallic impurities were first dissolved in hot aqua regia (HNO_3/HCl 1:3), followed by removal of organic contaminants with hot "piranha" solution (H_2O_2/H_2SO_4 1:3) at 90 ^oC for 1 hour. Hydrogen-terminated diamond (H-diamond) was prepared by exposure of diamond

crystal to microwave hydrogen plasma using 800 W microwave power and 300 sccm of hydrogen gas flow for 15 minutes. Oxygen-terminated diamond (O-diamond) was obtained by oxygen plasma treatment using a radio frequency plasma system (Diener electronic-Femto). Oxygen gas flow was maintained at 5 sccm at 70 W for 3 minutes.

4.1.2.2 X-ray photoelectron emission spectroscopy

The bonding environments of H-diamond and O-diamond were investigated prior to the transfer of CVD graphene for device fabrication, using X-ray photoelectron spectroscopy (XPS). It was performed using a non-monochromated Al Kα X-ray source at 1486.6 eV (Thermo VG Scientific) with a Phoibos 100 electron analyzer (SPECS GmbH, Germany) equipped with 5 channeltrons. The pass energy of the hemisphere analyzer was set at 50 eV for wide scan and 20 eV for narrow scan, while the takeoff angle was fixed at normal to the sample.

4.1.2.3 Growth and transfer of CVD graphene

The graphene sheets used in this study were grown by CVD following reported procedures[16]. The process was carried out in a quartz tube at reduced pressure with copper as the catalyst for graphene growth. The copper foil (thickness of 25 mm, purity of 99.8%) was heated at 1,275 K under a 10-sccm

flow of H_2 (~400 mTorr) to reduce the oxide present, increase the grain size and ensure a smooth surface for growth. Next, CH_4 was introduced into the chamber for growth. CH_4 (10 sccm) and H_2 (10 sccm) was maintained at ~750 mTorr for 30 min. Following that, the grown sheet was cooled in an atmosphere of H_2 to room temperature. The graphene on copper foil samples were coated with poly(methyl methacrylate) (PMMA) and transferred onto desired substrates.

4.1.2.4 Fabrication of graphene-diamond device

Graphene was transferred onto diamond substrates according to protocols as described above. Following that, 100 μL 4% poly(methylmethacrylate) (PMMA) (MicroChem, MW: 495 K) anisole solution was spin-coated on substrates at 4,000 rpm and baked at 180 ^{o}C for 2 mins. Arrays of four-terminal devices were patterned by electron beam lithography (FEI/Sirion), and this is followed by the development of PMMA with a methyl isobutyl ketone (MIBK) and isopropyl alcohol (1:1) solution. Thermal evaporation of 5 nm Cr/30 nm Au was followed by lift off in warm acetone. In a subsequent e-beam step, an etch mask was patterned and the graphene was exposed to 20 W, 20 sccm oxygen plasma (RIE NTI-2312) for 20 seconds after resist development. The devices were annealed in 10 % Ar/H_2 for 3 h to reduce the residue. The typical device dimension is 1.7 μm length between inner electrodes and a width of 900 nm. The contact pads of these

samples were wire-bonded with 25 μm-thin Al wire for electrical measurements.

4.1.2.5 Hall measurement

For typical resistivity measurements, a low frequency a.c. (~ 13 Hz), 10-100 nA drive current was applied across the source-drain (S/D) terminals from the internal oscillator output of Stanford SR830 lock-in amplifier and a phase-sensitive detection of the ac voltage across the inner two terminals was done to measure the graphene resistance. The back-gate voltage was applied to the silicon gate using Keithley 6430 sub-femtoamp sourcemeter and the typical gate leakage does not exceed 1-1.5 nA. For Hall measurements, the transverse voltage was measured as a function of applied external magnetic field perpendicular to the plane of the sample. The magnetic field used was 1 Tesla. The carrier density was obtained from the slope of the Hall voltage vs. magnetic field plot. Together with the resistivity (1/Ω) measurement, an estimate for the mobility $\mu = \Omega/ne$ was also obtained.

4.1.2.6 Temperature dependent electrical measurement

For low temperature measurement, the sample was immersed in flow of cold helium gas in a Cryogenics variable temperature cryostat. The Hall data was recorded both at ambient temperature and at T = 4 K to verify that

the density did not change during temperature sweeps. The four-terminal resistivity was measured as a function of temperature in the range T = 4-300 K for all samples.

4.1.3 Results and discussion

4.1.3.1 Characterization of substrates and devices

The deconvoluted XPS spectra of C1s and O1s regions are shown in Fig 4.1. The symmetrical C1s collected from H-diamond, situated at 284.2 eV corresponds to emission from bulk sp^3-hybridised carbon, whereas C1s spectrum collected from O-diamond is asymmetrical. Upon exposure of diamond substrates to oxidative treatments, the XPS spectrum reveals upshifted components at 1.6 and 2.6 eV with respect to the bulk C1s peak, which can be assigned to hydroxyl[17-20] and carbonyl functionalities respectively[17,21,22]. The O1s spectrum reveals the relative amount of oxygen coverage on the surfaces of the respective diamonds and it is apparent that the H-diamond has less polar functionalities, which is capable of manifesting as charge traps, as compared to its oxidized counterpart.

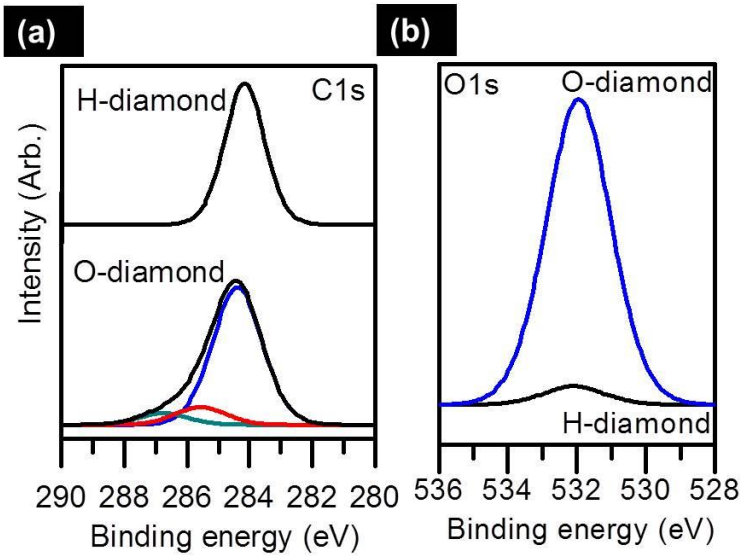

Figure 4.1 XPS measurement of H-diamond and O-diamond as prepared (a) C 1s and (b) O1s spectra.

Arrays of four-terminal devices were patterned by electron-beam lithography and illustrated in Fig 4.2a and b. Typical separation between inner electrodes is 1.7 μm and the width is 900 nm. Chemical vapor deposited (CVD) graphene film is used as the electrical transduction platform due to its large area and high electrical conductivity, which makes it the most possible route of graphene production for commercialization. Atomic force microscopy was used to characterize the surface of the single crystalline diamonds employed for the study, as well as to measure the topography of the surface after the transfer of graphene sheet. The root mean square roughness of the diamond, before deposition of graphene, was measured to be ~0.5nm, which corresponds to a surface of relatively low roughness. In juxtaposition to the smooth surface of bare diamond, wrinkles and foldings that originate from graphene is clearly evident in Fig 4.2d, after the transfer process.

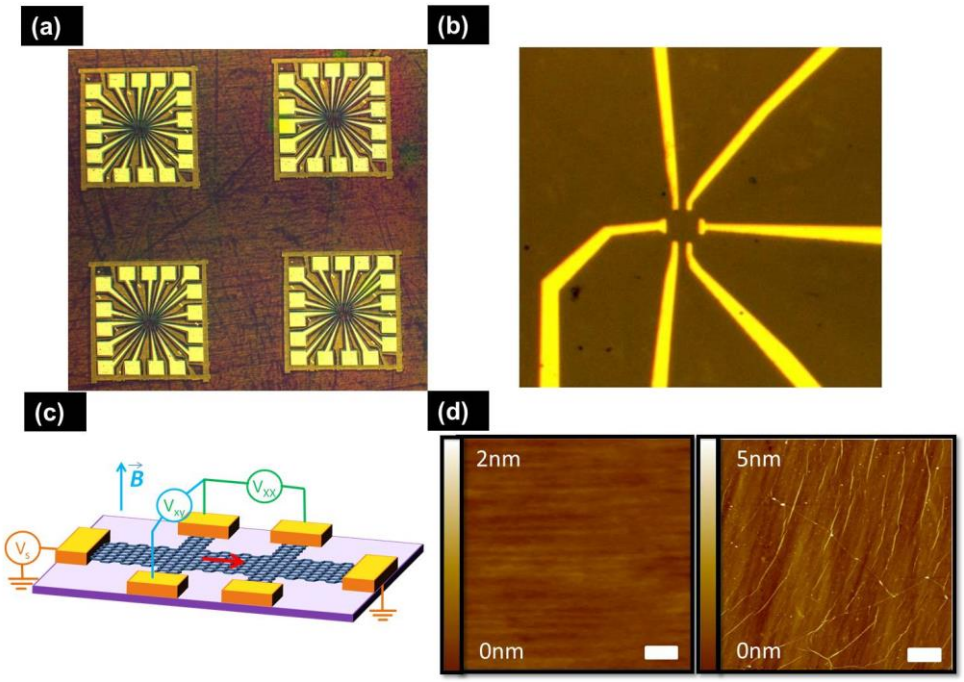

Figure 4.2 Surface characterization of diamond substrates and graphene-diamond devices. (a) Array of devices of graphene on diamond (b) Devices of graphene on diamond. Note that the etched region is only faintly visible due to the poor contrast of graphene on diamond. (c) Schematic representation of graphene on diamond device and (d) AFM images of (i) diamond and (ii) graphene on diamond. Scale bar correspond to 1 μm.

It is well-known that chemically vapor deposited diamond are likely to have impurities, such as graphitic and amorphous carbon. Hence, Raman spectroscopy was used to verify the quality of diamond substrate and layer thickness of CVD graphene film. (see Fig 4.3)

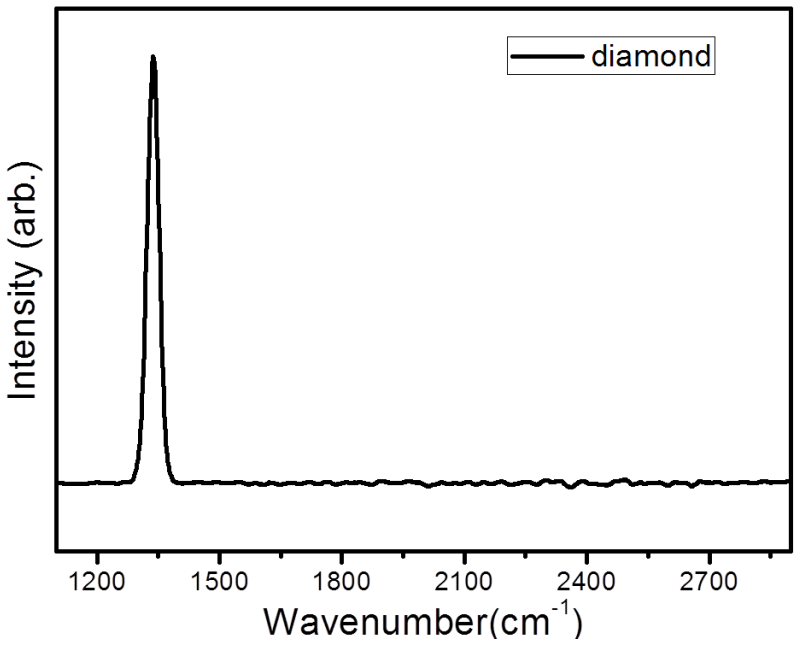

Figure 4.3 Raman spectrum of monocrystalline diamond

The high crystallinity of the diamond employed in this study can be confirmed by the intense peak, which is well-fitted with a Lorentzian line shape, and the absence of signal arising from graphitic and amorphous carbon in the regions between 1,000 to 1,600 cm^{-1}. Both graphite and amorphous carbon have Raman scattering efficiencies greater than diamond. In other words, for the same number of atoms present in the three carbon forms, diamond, graphite and amorphous carbon, diamond would give a much weaker Raman signal as compared to both graphite and amorphous carbon. The Raman scattering efficiencies, relative to diamond, has been reported to be 50 times for graphite[23] and 233 times for amorphous carbon[24]. This further attests to the high quality of diamond sample, as only signal arising from diamond was collected from the sample. The ratio of the integrated intensity

of G band (1,586cm^{-1}) to 2D band (2,678cm^{-1}) of 0.3, suggests the graphene film to be a high quality monolayer[25] (see Fig 4.5).

4.1.3.2 Probing of electrical properties

A top gate dielectric will introduce both additional surface phonon modes as well as possible charged impurities. Therefore for the density-dependent characterization of the graphene/diamond interface we relied on the variations of environmental doping of graphene seen across different samples. For low temperature measurement, the sample is immersed in a flow of cold He gas in a cryogenics variable temperature cryostat. Hall data is recorded both at ambient and T=4 K to verify that carrier density does not change during temperature sweep (4-300 K).

A plot of the normalized resistivity as a function of temperature for 3 devices of graphene on O-diamond devices at carrier densities, with hole densities ranging from n~1.8×10^{12} to 2.7×10^{12} cm^{-2} is shown in Fig 4.4a. It should be noted that despite the difference in the carrier density, all 3 samples have mobility in the 1,000-3,000 cm^2 V^{-1} s^{-1} range. In particular, the O-diamond1 device and O-diamond3 device have similar values of mobility (see Table 4.1).

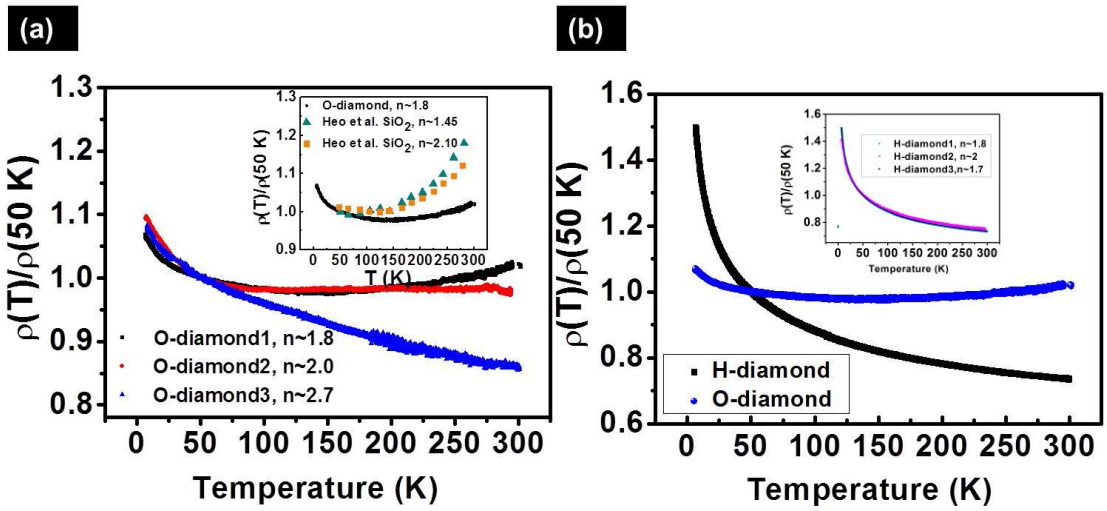

Figure 4.4 Temperature dependent resistivity of graphene. (a) Resistivity against temperature for three graphene on O-diamond devices. Inset compares graphene on O-diamond to graphene on SiO_2 (data of SiO_2 from Heo *et al* [Ref. 10]) (b) Resistivity against temperature of graphene on H-diamond and O-diamond, with similar carrier density. Inset shows three graphene on H-diamond devices.

Table 4.1 Characterization of the three graphene on O-diamond devices, displaying important parameters.

Substrate	Mobility ($cm^2V^{-1}s^{-1}$)	Resistivity (300 K) Ohms	Carrier density (10^{12} cm^{-2}) at 300 K	Carrier density ($10^{12}cm^{-2}$) at 25 K
O-diamond1	3,580	1,018	1.71	1.91
O-diamond2	1,450	2,170	2	2
O-diamond3	3,300	700	2.7	2.7

The temperature dependence of resistivity obtained is non-monotonic, as previously seen for CVD graphene on SiO_x substrates. With increasing carrier density, the high-temperature SO phonon-induced resistivity decreases as a result of screening. Next, we compare the temperature dependence of graphene on O-diamond against the case SiO_2 substrates[10] (see inset of Fig 4.4a). Despite having similar surface functionalities, the trend observed on

these two substrates is significantly different. For comparable values of carrier mobilities and densities, the graphene/O-diamond devices show much weaker metallic behavior ($d\rho/dT > 0$) high temperature resistance. This trend can be rationalized in terms of the difference in their SO phonon frequencies. The lowest significant mode for SO phonon frequency of O-diamond is 155 meV whereas the SO frequency SiO_2 is 59 meV, followed by another mode at 116 meV[10,15,26]. Since the SO phonons of O-diamond can only be activated with higher energy, the weaker high-temperature resistance can be understood.

Table 4.2 Graphene on H-diamond1 and O-diamond1 measured carrier density and mobility.

Substrate	Carrier density (10^{12} cm^{-2}) at 300 K	Mobility ($cm^2V^{-1}s^{-1}$)
H-diamond1	1.87	584
O-diamond1	1.81	3,580

The plot shown in Fig 4.4b compares normalized resistivity as a function of temperature for graphene on H-diamond and O-diamond substrates. It is interesting to note that although devices of similar carrier density were compared, the mobility of charge carriers in graphene is quite different (Table 4.2) (584 and 3,580 cm^2 V^{-1} s^{-1} for H-diamond and O-diamond devices respectively) and a much stronger insulating behavior is observed for graphene on H-diamond.

Raman spectroscopy (Witec CRM200) was employed to estimate the density of charged impurities for the two cases. In order to avoid fabrication

damage and charge transfer, no contacts were fabricated on the samples subjected to Raman study. A comparison of the Raman spectra (see Fig 4.5) reveals that O-diamond dopes graphene to a greater extent relative to H-diamond, as judged by a stiffening of the G band, decrease of both its FWHM (G) and I_{2D}/I_G ratio[27,28] (Table 4.3).

Table 4.3 Table showing FWHM (G peak) and ration of I_{2D}/I_G for graphene on H-diamond and O-diamond**.**

Substrate	FWHM (G peak)	I_{2D}/I_G	Charge impurity concentration
H-diamond	10 cm^{-1}	3.5	0.7 $\times 10^{12}$ cm^{-2}
O-diamond	7 cm^{-1}	1.5	3.5 $\times 10^{12}$ cm^{-2}

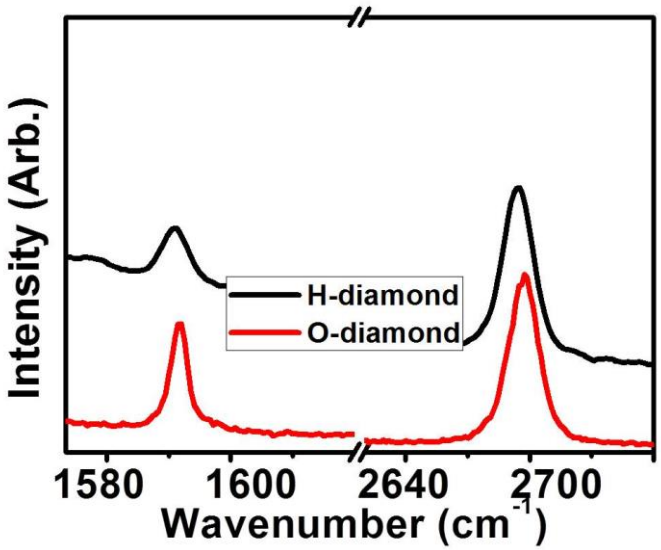

Figure 4.5 Raman spectroscopy of graphene on H-diamond and O-diamond. Inset shows the value of FWHM (G peak) and the ratio of I_{2D}/I_G.

The concentration of charge impurities shown in Table 4.3 are estimated from the blue shift of G band. According to the relation obtained from previous Raman spectroscopy studies[29] the concentration of charged impurities on O-diamond surface is approximately 4 times higher than that for H-diamond. If surface charge transfer was the dominant factor (in this mobility range 1,000 $cm^2 V^{-1} s^{-1}$ regime) in affecting the carrier mobility of graphene, we would expect graphene on H-diamond to demonstrate higher carrier mobility. Yet, such behaviour was not observed in our study. Therefore, this highlights the importance of intrinsic defects of graphene in influencing carrier mobility in the ~1,000 $cm^2 V^{-1} s^{-1}$ regime.

4.1.4 Conclusion

In summary, we have employed diamond as a novel platform towards understanding charge scattering mechanisms in graphene from temperature-dependent resistivity measurements. CVD graphene transferred on oxygen terminated diamond device shows a much weaker high-temperature metallic behavior when compared to CVD graphene on SiO_2 substrates, due to the significantly higher SO phonon frequency modes of the former. With a change in the surface termination of diamond, the charge transport of graphene was significantly modulated. Despite devices of similar carrier density were compared, on H-diamond and O-diamond, the mobility of charge carriers in graphene is 7 times higher on oxidized diamond and a much stronger insulating behavior is observed for graphene on H-diamond.

4.2. Graphene-diamond electrode for enhanced photovoltaic

4.2.1 Introduction

Although indium tin oxide (ITO) is widely used as the transparent and conducting electrode for optoelectronics devices, there are rising concerns over its stability[30]. Alternative candidates electrodes such as transparent conducting oxides (TCOs)[31,32], conducting polymers films[33,34] and graphene films have been considered[35,36], but the issue of chemical stability and low efficiency remains. In addition, ITO is essentially a degenerate *n*-type semiconductor and the hole injection barrier is considerably high for many organic dyes. Whilst ITO has been traditionally used as the anode material in solar cells, it can be envisaged that *p*-type diamond with high conductivity and transparency can perhaps act better as an anode due to its intrinsic hole-acceptor characteristics. It is worth mentioning that the potential of using *p*-doped nanocrystalline diamond as the anode for organic solar cells, because of its outstanding photostability and well-matched energetics, has been demonstrated previously[37].

There has been tremendous progress in the plasma-enhanced chemical vapour deposition (PECVD) of nanocrystalline diamond (NCD) films prepared on large-area glass, quartz, and even polymer substrates at low temperatures (<400 ^{o}C)[38,39], which enabled many engineering applications. In principle, the precursors for the synthesis of these diamond films are inexpensive dilute methane-in-hydrogen mixture gas feeds, thus large-area

coating on glass substrates is commercially viable. Introducing boron (for example, trimethylboron source) into the gas feeds creates acceptor states into the diamond (0.36 eV from the valence band maximum, or metallic states for boron concentration > 5×10^{20} cm^{-3}) film for hole transport in the otherwise insulating material. Two essential properties of an optical transparent electrode (OTE) are its optical transparency and electrical conductivity. Although the electrical conductivity of diamond could be improved by doping with boron atoms, its optical transparency decreases with increasing levels of dopants. Therefore, an optimum level of dopants should be introduced to strike a balance between electrical conductivity and optical transparency for the purpose of an OTE.

One potential advantage of using diamond as the electrode material is the improved interface stability between the organic active layer and itself as compared to the poor interface stability between the organic active layer and inorganic electrode, ITO. The inert surface of diamond prevents reactive interface formation arising from diffusion of impurities, a problem faced by ITO in solid-state inorganic solar cells during the deposition of $Cu(In_{1-x}Ga_x)Se_2$ (ref40). Another unique aspect of diamond is that its surface energy levels can be readily tuned by controlling its surface termination[41], which affords the advantage of tailoring interfacial energy levels for more efficient charge transfer[42]. Moreover, the surface of diamond can be considered as an organic template. A number of functionalization strategies based on chemically robust C-C coupling have been developed over the years, including photochemical[43,44], electrochemical[45], and chemical approaches[46,47] for tethering functional groups on the diamond surface.

Here, we explore a novel way of enhancing the electrical conductivity of diamond electrode by the coupling of graphene sheet via a molecular (nitro-phenyl) wire. Graphene has an unprecedented carrier mobility that has the potential of enhancing the charge transfer between the active organic layer and the electrode. Moreover, a monolayer of graphene absorbs *ca.* 2.3% of visible light. As such, the electrical conductivity of the diamond electrode can be improved with almost no or minimal compromise on its optical transparency. Since the weakest link of a molecular device usually lies in the interface between the organic and the electrode, we specially select the linking of graphene and diamond through the use of an aryl linker (C-C bond) as the presence of π-π stacking allows denser packing of the organic layer to prevent hydrolysis or oxidative cleavage of the interfacial bonds arising from diffusion of water or oxygen to the interface. The coupling of aryl functionalities to diamond surface can be achieved through simple spontaneous grafting of aryldiazonium salt. Moreover, the aryl linkers are also capable of interacting with the electron cloud of graphene to afford greater efficiency in charge transfer. As such, it is envisaged that the interface will be more robust as compared to the conventional device that possesses an inorganic/organic interface.

4.2.2 Materials and methods

4.2.2.1 Preparation of diamond electrodes

Optically transparent diamond electrodes were fabricated by the PECVD in the form of a thin layer of boron-doped diamond film on quartz substrate (160-nm-thick, boron concentration 3×10^{21} cm^{-3}) according to published procedures[38,48]. Acid cleaning and hydrogen plasma cleaning of diamond were used for all diamond samples. Metallic impurities were first dissolved in hot aqua regia (HNO_3/HCl 1:3), followed by removing organic impurities from the diamond samples by hot ‘‘piranha’’ solution (H_2O_2/H_2SO_4 1:3) at 90 ^oC for 1 h. H-termination of diamond samples was performed by microwave hydrogen plasma treatment using 800W microwave power and 300 sccm of hydrogen gas flow for 15 min.

4.2.2.2 Funtionalization of diamond surface

The diamond samples were immersed into 0.100 M 4-nitrobenene diazonium tetrafluoroborate salt (Aldrich 98%) in 0.1M HCl (which was purged with N_2 gas for at least 15 mins, prior to use) for 2 hours. After which, they were sequentially rinsed and sonicated in acetone, isopropyl alcohol (IPA), and Nanopure water and dried under N_2 stream for the removal of weakly adsorbed organic materials on the surface of diamond. CV reduction was carried out with an Autolab PGSTAT30 potentiostat (Eco Chemie B.V.)

in a single compartment Teflon cell with three-electrode configuration system: a diamond working electrode, Ag/AgCl reference electrode (3.0 M KCl) and a Pt mesh counter electrode. A small area (0.07 cm^2) of the diamond substrate was exposed to the 0.100 M KCl in 10% methanol through a Viton O-ring and reduction was carried out by three repeated linear voltage sweeps from -1.0 V to 1.0 V at scan rate of 50 mVs^{-1}. The graphene on copper foil samples were coated with poly(methyl methacrylate) (PMMA) and transferred onto desired substrates. Subsequently, the electrodes were exposed to UV light (254 nm, 1.5 Wcm^{-2}) in air overnight to ensure complete oxidation. Such treatment has been reported to generate free radicals, and thus will enable bonding between the amine group of the molecular wire and graphene[16]. Ultrasonic energy was delivered to the modified electrode to verify and demonstrate the covalent bonding of graphene on diamond via the molecular wire.

4.2.2.3 Photocurrent testing

Photocurrent measurements of the modified BDD electrodes were measured in 0.1M Na_2SO_4 solution containing 5 mM methyl viologen (MV^{2+}) as electron carrier under 1 sun irradiation (100 $mWcm^{-2}$, AM 1.5G) and at 0V bias (versus Ag/AgCl). The diamond electrode was used as a working electrode in a typical three-electrode configuration system. The resistivity of the electrodes was measured in via a four terminal fashion.

4.2.3 Results and Discussion

4.2.3.1 Modification of the diamond electrode

The functionalization scheme of diamond is shown in Fig. 4.6. The first step of the reaction scheme involves the spontaneous grafting of the diazonium salt onto BDD surface. This method of coupling was found to be facile even on insulating diamond substrates.

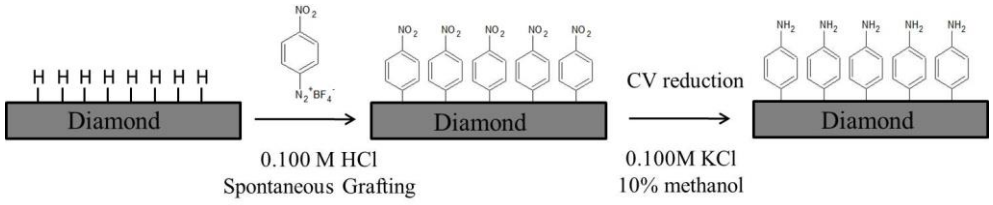

Figure 4.6 Functionalization route using aryldiazonium salt, followed by CV reduction.

Simply by immersion of H-terminated diamond nanocrystalline diamond in 0.100 M 4-nitrobenzene/0.1 M HCl solution for 2 hours, covalently grafted nitrophenyl groups were formed on diamond surface. Based on the grafting mechanism, a phenyl radical is produced directly through an electron transfer from the diamond to the aryldiazonium salt concerted with the cleavage of a dinitrogen[49]. It has been reported that this mode of coupling is only possible when the diamond is terminated with hydrogen groups but the reaction is inhibited in the presence of oxygen functionalities. When diamond is immersed in solution, it attains p-type conductivity due to the surface transfer doping from the oxygen redox pairs[50]. As the conductivity of diamond is

restricted to its surface, the conductive layer is only a few Angstroms thick and the charge transfer is limited by the small density of charge carriers. As a result, the reaction is expected to be self-limiting at monolayer due to the increasing charge resistance across the interface when an organic monolayer is formed.

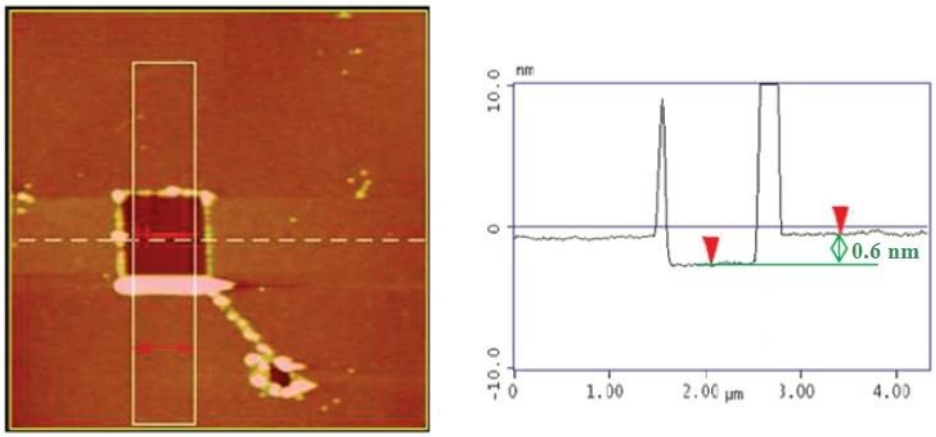

Figure 4.7 AFM image of scratched area of nitrophenyl on diamond.

Verification of thickness of the organic layer was conducted by AFM scratching experiments on single crystal diamond C(100). A large force of *ca.* 120 nN was used for the removal of grafted nitrophenyl groups and imaging was carried out at much reduced force (0.3 nN). To minimize the error by the presence of artifacts, a line profile was drawn through the trench and perpendicular to the tip scanning direction. The AFM line profile in Fig 4.7 shows a height difference of 0.6 (±0.2) nm between the unscratched region and the trench, which agrees closely with the height of a nitrobenzene molecule as predicted by density functional theory (DFT). Subsequently, CV was performed to reduce the nitro terminations to amine functionalities as

evidenced by the change in binding energy of the XPS N1s peaks as shown in Fig 4.8 before and after CV reduction.

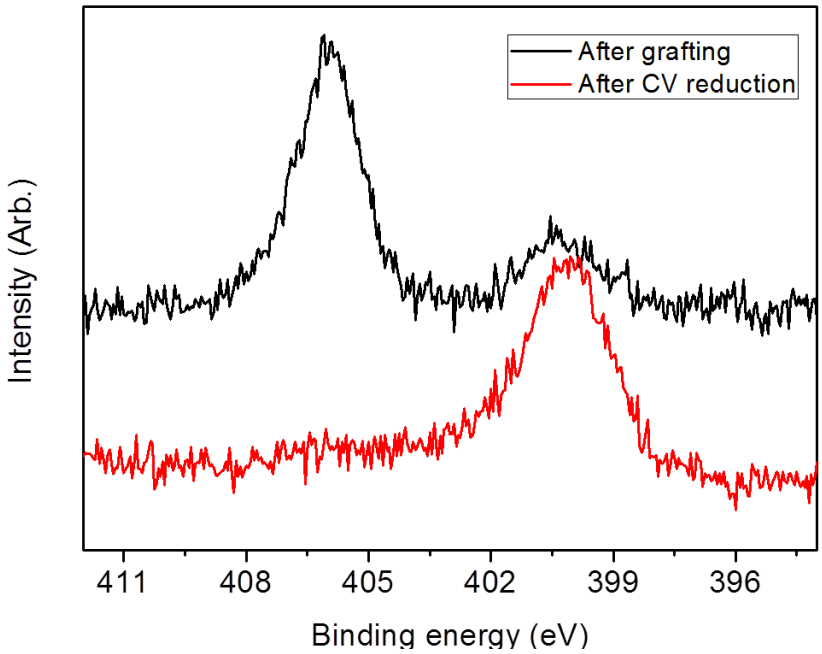

Figure 4.8 XPS spectra illustrating N1s region after grafting and reduction processes.

Graphene sheet was then transferred onto diamond and the photochemical reaction was activated by UV light. This procedure is being depicted by the schematic diagram shown below in Fig 4.9.

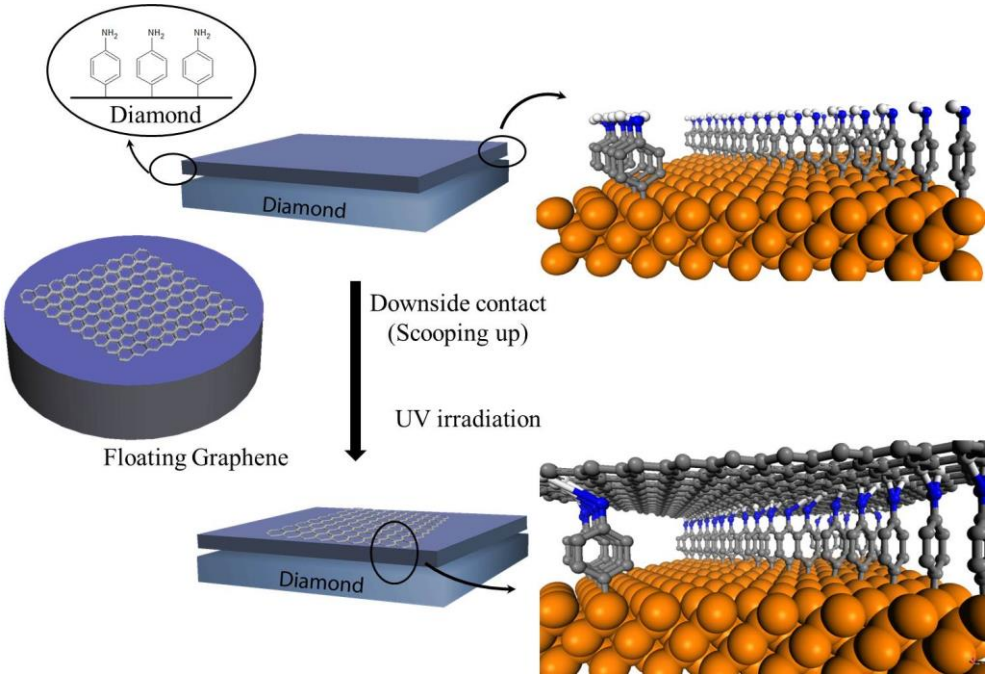

Figure 4.9 Schematic diagram depicting the transfer of graphene and the coupling of graphene process.

To verify that graphene sheet was covalently coupled via molecular wire to the surface of diamond, ultrasonic waves were imparted to the modified diamond electrodes. Since ultrasonic treatment has been used as one of the tools for the exfoliation of graphene from graphite with the use of intercalation agents, it is capable of breaking the van der Waals forces that hold the graphitic layers together. Cavitation implosions generate extremes of temperature and pressure in the liquid and is capable of removing inert organic layers which coat the surface of a sample. Here, an ultrasonic probe, operating at 20 kHz is inserted into a beaker, containing the modified diamond electrode and is filled with distilled water. Energy of 90 kJ was imparted to the respective diamond electrodes that were subjected to different treatments. It can be seen from the

optical images captured that only the graphene that was exposed to UV light on NH_2 modified diamond survives the ultrasonic process (see Fig 4.10).

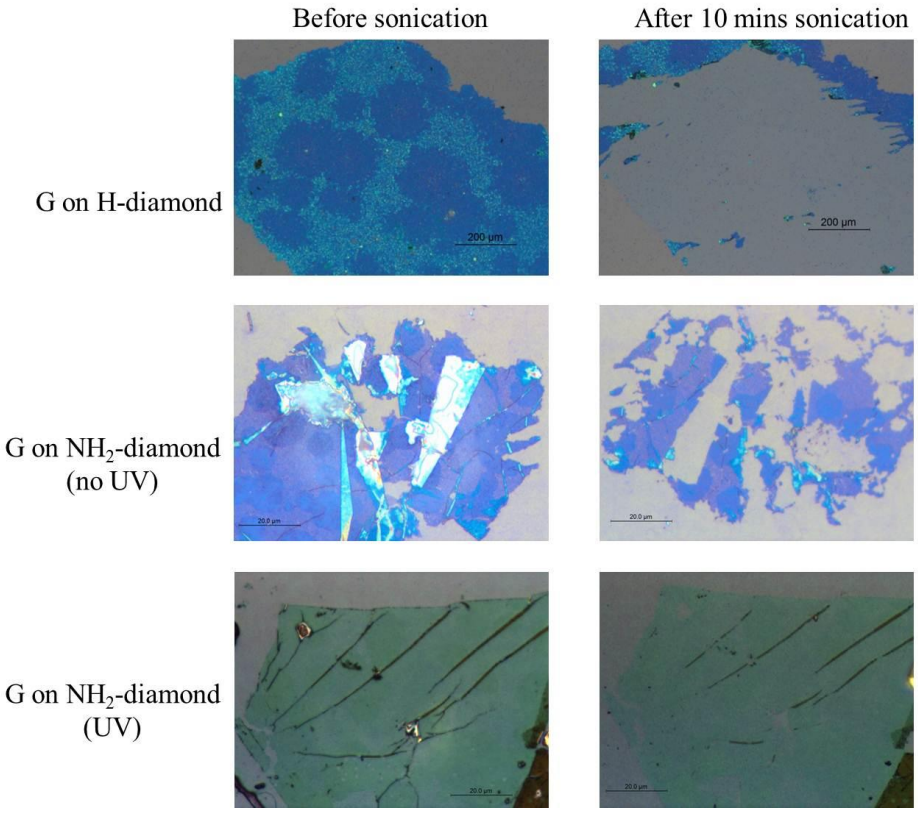

Figure 4.10 Optical images of graphene on H-diamond, NH_2-diamond (without UV treatment) and NH_2-diamond (with UV treatment), before and after ultrasonic treatment.

4.2.3.2 Evaluating the performance of modified diamond electrodes

The diamond modified electrodes were then coated with the commonly used emissive conjugated polymer (poly(3-hexylthiophene), P3HT) and photocurrent measurements were carried out. It can be seen that the photocurrent generated on H-diamond and NH_2-diamond have similar magnitude whereas diamond that has graphene coupled to it (via the molecular

wire) has a decreased sheet resistance and has a 3 fold enhancement of generated photocurrent (see Fig 4.11).

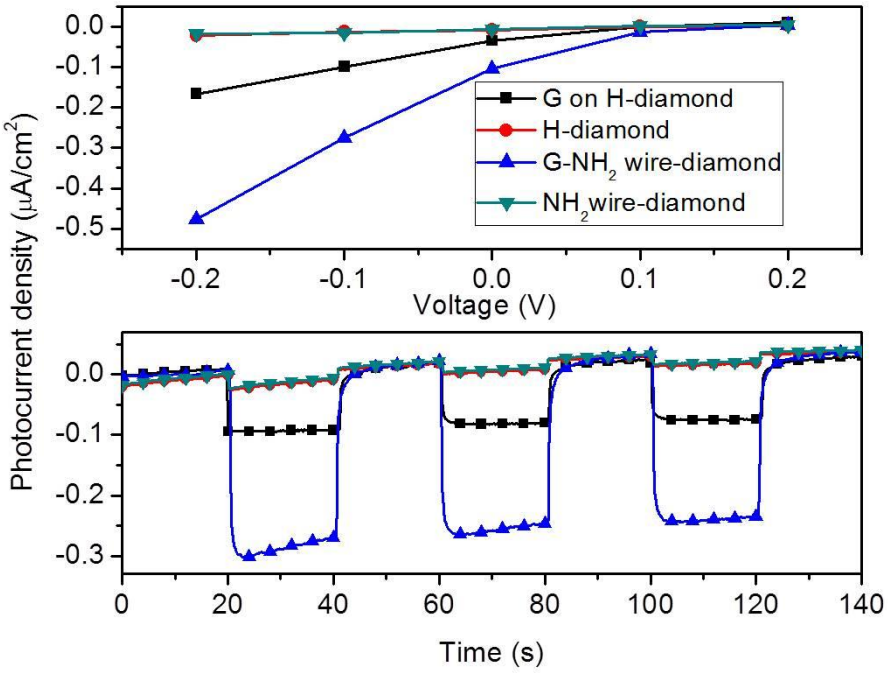

Figure 4.11 Photocurrent response at different applied voltages (versus Ag/AgCl) of P3HT on modified diamond electrodes under 1 sun (100 mWcm-2, AM 1.5G) illumination (top panel) and photocurrent response of respective modified diamond electrodes at 0V (bottom panel).

It is noteworthy to mention that the magnitude of photocurrent generated with the G-NH_2-diamond electrode is 6 times larger relative to the unmodified electrode. Sheet resistance of the electrodes were probed and the sheet resistance of diamond was observed to increase slightly with the grafting of an insulating organic layer onto its surface. However, it can be seen in Table 4.4 that graphene decreases the sheet resistance when it is bound to NH_2-diamond from 7.9 kΩ per square to 1.1 kΩ per square. Even though the sheet resistance of graphene not covalently bound to diamond (G on H-diamond) is similar to

the G-NH_2-diamond sample, the significantly higher photocurrent generated implies more efficient charge transfer from the photoactive layer to the graphene modified diamond electrode via the molecular wire.

Table 4.4 Sheet resistance of respective modified diamond electrodes

Substrate/Conditions	Sheet Resistance/ Ω per square
H-diamond	6340±200
G on H-diamond	1570±140
NH_2-diamond	7910±170
G-NH_2-diamond (with UV)	1130±195

4.2.4 Conclusion

In conclusion, this work demonstrates the potential of using graphene coupled to nanocrystalline diamond for organic solar cell because of its ability to improve the electrical conductivity of the diamond anode with minimum compromise on its optical transparency. Graphene that is covalently coupled by molecular wire to diamond is mechanically robust and can withstand ultrasonication stress. At the same time, despite having comparable sheet resistance, graphene is able to facilitate efficient charge transfer through the covalently bonded molecular wire to diamond electrode as compared to graphene sheet that is physisorbed on diamond surface. This study paves the way for using graphene to modify the electrical conductivity of chemical vapour deposited diamond electrodes that may become a viable alternative to ITO.

4.3 References

1 Avouris, P. Graphene: Electronic and photonic properties and devices. *Nano Letters* **10**, 4285-4294 (2010).

2 Berger, C. *et al.* Electronic confinement and coherence in patterned epitaxial graphene. *Science* **312**, 1191-1196 (2006).

3 Novoselov, K. S. *et al.* Two-dimensional gas of massless Dirac fermions in graphene. *Nature* **438**, 197-200 (2005).

4 Zhang, Y., Tan, Y. W., Stormer, H. L. & Kim, P. Experimental observation of the quantum Hall effect and Berry's phase in graphene. *Nature* **438**, 201-204 (2005).

5 Bae, S. *et al.* Roll-to-roll production of 30-inch graphene films for transparent electrodes. *Nature Nanotechnology* **5**, 574-578 (2010).

6 Chen, J. H., Jang, C., Xiao, S., Ishigami, M. & Fuhrer, M. S. Intrinsic and extrinsic performance limits of graphene devices on SiO_2. *Nature Nanotechnology* **3**, 206-209 (2008).

7 Morozov, S. V. *et al.* Giant intrinsic carrier mobilities in graphene and its bilayer. *Physical Review Letters* **100** 016602 (2008).

8 Hwang, E. H., Adam, S. & Sarma, S. D. Carrier transport in two-dimensional graphene layers. *Physical Review Letters* **98** 186806 (2007).

9 Katsnelson, M. I. & Geim, A. K. Electron scattering on microscopic corrugations in graphene. *Philosophical Transactions of the Royal Society A: Mathematical, Physical and Engineering Sciences* **366**, 195-204 (2008).

10 Heo, J. *et al.* Nonmonotonic temperature dependent transport in graphene grown by chemical vapor deposition. *Physical Review B - Condensed Matter and Materials Physics* **84** 035421 (2011).

11 Pachoud, A., Jaiswal, M., Ang, P. K., Loh, K. P. & Özyilmaz, B. Graphene transport at high carrier densities using a polymer electrolyte gate. *EPL* **92** 27001 (2010).

12 Adam, S., Hwang, E. H., Galitski, V. M. & Das Sarma, S. A self-consistent theory for graphene transport. *Proceedings of the National Academy of Sciences of the United States of America* **104**, 18392-18397 (2007).

13 Jaiswal, M. *et al.* Controlled hydrogenation of graphene sheets and nanoribbons. *ACS Nano* **5**, 888-896 (2011).

14 Michaelson, S. & Hoffman, A. Ambient contamination of poly-crystalline diamond surfaces studied by high-resolution electron energy loss spectroscopy and X-ray photoelectron spectroscopy. *Diamond and Related Materials* **17**, 920-924 (2008).

15 Shpilman, Z., Gouzman, I., Grossman, E., Akhvlediani, R. & Hoffman, A. Hydrogen plasma and atomic oxygen treatments of diamond: Chemical versus morphological effects. *Applied Physics Letters* **92** 234103 (2008).

16 Siraki, A. G. Chapter two- free radical metabolites in arylamine toxicity. *Adv. Mol. Toxicol.* **7**, 39-82 (2013).

17 Ballutaud, D., Simon, N., Girard, H., Rzepka, E. & Bouchet-Fabre, B. Photoelectron spectroscopy of hydrogen at the polycrystalline diamond surface. *Diamond and Related Materials* **15**, 716-719 (2006).

18 Denisenko, A., Pietzka, C., Romanyuk, A., El-Hajj, H. & Kohn, E. The electronic surface barrier of boron-doped diamond by anodic oxidation. *Journal of Applied Physics* **103** 014904 (2008).

19 Kondo, T., Honda, K., Tryk, D. A. & Fujishima, A. Covalent modification of single-crystal diamond electrode surfaces. *Journal of the Electrochemical Society* **152**, E18-E23 (2005).

20 Rutter, M. J. & Robertson, J. Ab initio calculation of electron affinities of diamond surfaces. *Physical Review B - Condensed Matter and Materials Physics* **57**, 9241-9245 (1998).

21 Pehrsson, P. E. & Mercer, T. W. Oxidation of the hydrogenated diamond (100) surface. *Surface Science* **460**, 49-66 (2000).

22 Wilson, J. I. B., Walton, J. S. & Beamson, G. Analysis of chemical vapour deposited diamond films by X-ray photoelectron spectroscopy. *Journal of Electron Spectroscopy and Related Phenomena* **121**, 183-201 (2001).

23 Wada, N. & Solin, S. A. Raman efficiency measurements of graphite. *Physica B+C* **105**, 353-356 (1981).

24 Sails, S. R., Gardiner, D. J., Bowden, M., Savage, J. & Rodway, D. Monitoring the quality of diamond films using Raman spectra excited at 514.5 nm and 633 nm. *Diamond and Related Materials* **5**, 589-591 (1996).

25 Graf, D. *et al.* Spatially resolved raman spectroscopy of single- and few-layer graphene. *Nano Letters* **7**, 238-242 (2007).

26 Wu, Y. *et al.* High-frequency, scaled graphene transistors on diamond-like carbon. *Nature* **472**, 74-78 (2011).

27 Casiraghi, C., Pisana, S., Novoselov, K. S., Geim, A. K. & Ferrari, A. C. Raman fingerprint of charged impurities in graphene. *Applied Physics Letters* **91** 233108 (2007).

28 Das, A. *et al.* Monitoring dopants by Raman scattering in an electrochemically top-gated graphene transistor. *Nature Nanotechnology* **3**, 210-215 (2008).

29 Yan, J., Zhang, Y., Kim, P. & Pinczuk, A. Electric field effect tuning of electron-phonon coupling in graphene. *Physical Review Letters* **98** 166802 (2007).

30 Scott, J. C. *et al.* Degradation and failure of MEH & PPV light emitting diodes. *Journal of Applied Physics* **79**, 2745-2751 (1996).

31 Cui, J. *et al.* Indium tin oxide alternatives - High work function transparent conducting oxides as anodes for organic light-emitting diodes. *Advanced Materials* **13**, 1476-1480 (2001).

32 Purushothaman, K. K., Dhanashankar, M. & Muralidharan, G. Preparation and characterization of F doped SnO_2 films and electrochromic properties of FTO/NiO films. *Current Applied Physics* **9**, 67-72 (2009).

33 Gustafsson, G. *et al.* Flexible light-emitting diodes made from soluble conducting polymers. *Nature* **357**, 477-479 (1992).

34 Zhang, F., Johansson, M., Andersson, M. R., Hummelen, J. C. & Inganäs, O. Polymer photovoltaic cells with conducting polymer anodes. *Advanced Materials* **14**, 662-665 (2002).

35 Wang, X. *et al.* Transparent carbon films as electrodes in organic solar cells. *Angewandte Chemie - International Edition* **47**, 2990-2992 (2008).

36 Eda, G., Fanchini, G. & Chhowalla, M. Large-area ultrathin films of reduced graphene oxide as a transparent and flexible electronic material. *Nature Nanotechnology* **3**, 270-274 (2008).

37 Lim, C. H. Y. X., Zhong, Y. L., Janssens, S., Nesladek, M. & Loh, K. P. Oxygen-terminated nanocrystalline diamond film as an efficient anode in photovoltaics. *Advanced Functional Materials* **20**, 1313-1318 (2010).

38 Williams, O. A., Nesládek, M., Mareš, J. J. & Hubík, P. in *Physics and Applications of CVD Diamond* 13-27 (Wiley-VCH Verlag GmbH & Co. KGaA, 2008).

39 Potocky, S. *et al.* Investigation of nanocrystalline diamond films grown on silicon and glass at substrate temperature below 400 C. *Diamond and Related Materials* **16**, 744-747 (2007).

40 Stotter, J., Show, Y., Wang, S. & Swain, G. Comparison of the electrical, optical, and electrochemical properties of diamond and indium tin oxide thin-film electrodes. *Chemistry of Materials* **17**, 4880-4888 (2005).

41 Stutzmann, M., Garrido, J. A., Eickhoff, M. & Brandt, M. S. Direct biofunctionalization of semiconductors: A survey. *Physica Status Solidi (A) Applications and Materials Science* **203**, 3424-3437 (2006).

42 Morkel, M. *et al.* Flat conduction-band alignment at the CdS/CuInSe2 thin-film solar-cell heterojunction. *Applied Physics Letters* **79**, 4482-4484 (2001).

43 Yang, W. *et al.* DNA-modified nanocrystalline diamond thin-films as stable, biologically active substrates. *Nature Materials* **1**, 253-257 (2002).

44 Härtl, A. *et al.* Protein-modified nanocrystalline diamond thin films for biosensor applications. *Nature Materials* **3**, 736-742 (2004).

45 Zhong, Y. L., Loh, K. P., Midya, A. & Chen, Z. K. Suzuki coupling of aryl organics on diamond. *Chemistry of Materials* **20**, 3137-3144 (2008).

46 Szunerits, S. & Boukherroub, R. Different strategies for functionalization of diamond surfaces. *Journal of Solid State Electrochemistry* **12**, 1205-1218 (2008).

47 Zhong, Y. L. *et al.* Diamond-based molecular platform for photoelectrochemistry. *Journal of the American Chemical Society* **130**, 17218-17219 (2008).

48 Nesládek, M. *et al.* Superconductive B-doped nanocrystalline diamond thin films: Electrical transport and Raman spectra. *Applied Physics Letters* **88** 232111 (2006).

49 Pinson, J. & Podvorica, F. Attachment of organic layers to conductive or semiconductive surfaces by reduction of diazonium salts. *Chemical Society Reviews* **34**, 429-439 (2005).

50 Maier, F., Riedel, M., Mantel, B., Ristein, J. & Ley, L. Origin of surface conductivity in diamond. *Physical Review Letters* **85**, 3472-3475 (2000).

Chapter 5

Binding of graphene and diamond for the formation of graphene nanobubbles as a hydrothermal anvil cell

Abstract:

The hardness and virtual incompressibility of diamond allow it to be used in high-pressure anvil cell. Here we report a new way to generate static pressure by encapsulating single crystal diamond with graphene membrane, the latter is well known for its superior nanoindentation strength and in-plane rigidity. Heating the diamond–graphene interface to the reconstruction temperature of diamond (~1,275 K) produces a high density of graphene nanobubbles that can trap water within. At high temperature, chemical bonding between graphene and diamond is robust enough to allow the hybrid interface to act as a hydrothermal anvil cell due to the impermeability of graphene. Superheated water trapped within the pressurized graphene nanobubbles was observed to etch the diamond surface to produce a high density of square-shaped voids. The molecular structure of superheated water trapped in the bubble was probed using vibrational spectroscopy and dynamic changes in the hydrogen-bonding environment was observed.

5.1 Introduction

Graphene is commonly thought of as a two-dimensional carbon flatland. This ideal picture however is valid only in special cases like suspended graphene[1-3], graphene grown epitaxially on SiC[4] or supported on low surface energy hexagonal boron nitride[5,6]. In fact, monolayer graphene is inclined towards deformation in the third dimension due to its large ratio of in-plane rigidity to bending rigidity. In most cases, the substrate supporting graphene induces buckling under compression and creates ripples and blisters, which sets a limit on the mobility of its charge carriers due to flexural phonons. A recent study by Pan *et al*[7] observed sub-micron bubbles due to the biaxial compressive strain in graphene/ hexagonal boron nitride heterostructure after thermal cyclings. Compressive strain between the lattice-mismatched Ru and graphene creates a buckling instability which manifests as periodic blistering (Moire humps) on the sheet[8,9], these blisters can be sintered to produce geometrically shaped bubbles on the metal[10], giving rise to electrodynamics that is coupled to the strain texture. While the strain properties of the bubbles have been studied using spectroscopic methods, the physical properties of trapped species inside the bubble have not been investigated. One interesting possibility, which has not been considered thus far, is the reactivity of the trapped fluid in the impermeable graphene bubble. The ability of graphene to seal the interface between itself and the supporting platform ensures the mechanical stability of these bubbles and provides a unique anvil cell for probing the dynamics of fluids trapped within this impermeable membrane, at conditions beyond the critical point of the fluid.

In almost all reported cases to date, the occurrence of the bubbles is sporadic over the graphene surface[11,12]. In order to record sufficient signal strength when probing the molecular structure of water trapped within each bubble, a high areal density of nanobubbles is needed. The diamond-graphene interface is selected to meet this requirement. First, the lattice mismatch between diamond and graphene will produce interfacial stress which induces periodic rippling on graphene. Second, covalent bonding between the two phases can occur when the surface of diamond is reconstructed thermally. Although the phases of diamond and graphite are known to coexist in surface-graphitized nanodiamond particles or during the initial nucleation stages of diamond growth[13-16], there is no clear insight into how graphene interfaces with diamond both structurally and electronically. The metallic-sp^2 and dielectric-sp^3 interface offer the perfect environment for studying the complex interplay between electronic and lattice degrees of freedom for the creation of new functionalities. Here, we transfer a chemical vapour deposited (CVD)-grown graphene monolayer onto single crystal diamond (100) and thermally anneal the interface to the reconstruction temperature of diamond in order to study the morphological evolution at the interface. We show that interfacial bonding results in the growth of high density nanobubbles across the graphene sheet. The resultant nanobubble "mat" has a distinct topographical and electronic landscape. Most interestingly, each graphene nanobubble interfacing with diamond acts as a hydrothermal anvil cell: the water entrapped is transformed into compressed, hot water (supercritical) that is highly corrosive to even one of the hardest known materials, diamond.

5.2 Materials and methods

5.2.1 CVD growth and transfer of graphene

The graphene sheets used in this study were grown by CVD following previous reported procedures[17]. The process was carried out in a quartz tube at reduced pressure with copper as a catalyst for G growth. The copper foil (thickness of 25 mm, purity of 99.8%) was heated at 1,275 K under a 10-sccm flow of H_2 (~400 mTorr) to reduce the oxide present, increase the grain size and ensure a smooth surface for growth. Next, CH_4 was introduced into the chamber for growth. CH_4 (10 sccm) and H_2 (10 sccm) was maintained at ~750 mTorr for 30 min. Following that, the grown sheet was cooled in an atmosphere of H_2 to room temperature. The graphene on copper foil samples were coated with poly (methyl methacrylate) (PMMA) and transferred onto desired substrates.

5.2.2 Surface preparation of single-crystal diamond, quartz and sapphire

Type IIa CVD single-crystal diamonds (100) were purchased from Element Six and mechanically polished to give rms ~0.2 nm before use. Acid cleaning and hydrogen-plasma cleaning of diamond were used for all diamond samples. Metallic impurities were first dissolved in hot aqua regia (HNO_3:HCl 1:3), followed by removing organic impurities from the diamond samples by hot ‘piranha’ solution (H_2O_2:H_2SO_4 1:3) at 375 K for 1 h. H termination of

diamond samples was performed by microwave hydrogen-plasma treatment using 800 W microwave power hydrogen gas flow for 15 min. Quartz (Photonics) and sapphire (MTI corporation) substrates of <0.1nm were sequentially rinsed and sonicated in acetone, isopropyl alcohol and Nanopure water, and then dried under N_2 stream before they were used.

5.2.3 Annealing for formation of GNB

The samples were mounted on a Mo sample plate, transferred into a UHV chamber with a base pressure of $<10^{-10}$ torr. Annealing was conducted at 1,275 K for 45 mins by e-beam heating (SPECS GmbH, Germany). Throughout the entire annealing process, it was ensured that the pressure did not rise beyond 10^{-8} Torr.

5.2.4 Atomic Force Microscopy

A Dimension ICON using Nanoscope V controller (Bruker, Santa Barbra, CA) equipped with a diamond probe (DNISP, Bruker AFM Probes, Camarillo, CA) was operated in Peakforce Quantitative Nanomechanical (QNM) mode for simultaneous topography imaging and Young's modulus mapping of the graphene bubbles. In Peakforce QNM mode, the tip is oscillated at a fixed frequency of about 2 kHz and continuously indents into the sample at a small depth of about 1-2 nm while scanning over the surface.

From each indentation force curve, different physical properties such as Young's modulus can be measured simultaneously with topography at each pixel with the same spatial and temporal resolutions (see Fig 5.1).

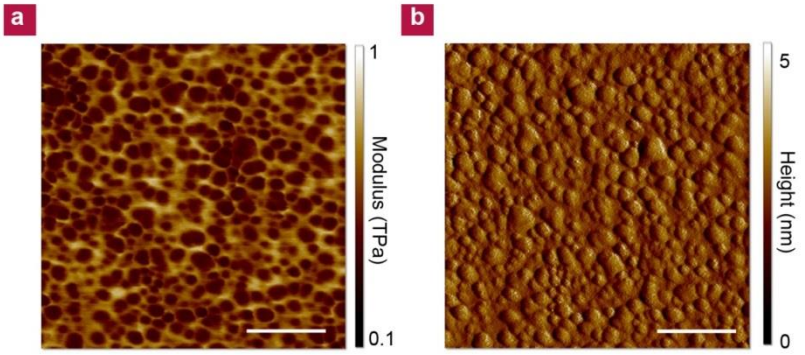

Figure 5.1 AFM images of GNBs showing their mechanical strength and sizes. (a) Young's modulus map of GNBs on diamond. (b) Topography map corresponding to a. The scale bars shown in a and b are 150 nm.

5.2.5 Ultraviolet photoelectron emission spectroscopy

The electronic structures of graphene–diamond were monitored using ultraviolet photoelectron spectroscopy. Measurements were carried out in an ultrahigh vacuum chamber (base pressure of 1 X 10^{-10} Torr). The spectra were calibrated and referenced to the Fermi level gold. No charging effect was observed for all samples. During the mapping of valence band, a -5V bias is applied to the sample to overcome the workfunction of the analyser (~4.4 eV).

5.2.6 Raman Spectroscopy

Raman spectra were obtained with NEOS-SENTERRA (Bruker) AFM-raman spectrometer at room temperature, with an excitation laser source of 532 nm. The laser power was always kept below 0.1 mW to prevent heating of the sample.

5.2.7 FTIR to probe the interaction of water molecules

FTIR of graphene and diamond samples were performed in the reflection mode by using an OPUS/IR PS15 spectrometer (Bruker). The sample was loaded into a high-temperature high pressure FTIR cell evacuated to 1X 10^{-4} Torr. The spectra were the results of 32 coadded interferograms at 4 cm^{-1} resolution between 400 and 6,000 cm^{-1} with collection times of approximately 2min. Each sample was analysed at least three times and results obtained were reproducible. The samples were heated up and spectra were recorded.

5.2.8 Molecular dynamics simulations

Our simulations were carried out with the REBO potential[18,19] for the models containing only carbon and hydrogen atoms and with ReaxFF[20] (reactive force field) for the models which contain oxygen atoms. Both

methods are implemented into LAMMPS (large-scale atomic/molecular massively parallel simulation package[17]). Periodic boundary conditions are applied in all three directions and the MD step was 0.5 fs. Structures obtained by this procedure were visualized with the VMD package[21].

5.3 Results and discussion

5.3.1 Graphene nanobubbles (GNBs) on diamond

A consequence of graphene being a soft membrane is that it can be strain-engineered to become highly corrugated by modifying its adhesion to the substrate. A CVD grown graphene monolayer sheet was transferred onto a diamond (100) crystal. After annealing the graphene-diamond interface at 1,275 K for 45 mins in ultra-high vacuum, GNBs with a density of ~8×10^{10} cm^{-2} (Fig. 5.2) appear. Each GNB measures about ~2 nm in height and has diameters that range from 5 to 30 nm (Fig. 5.2c and d).

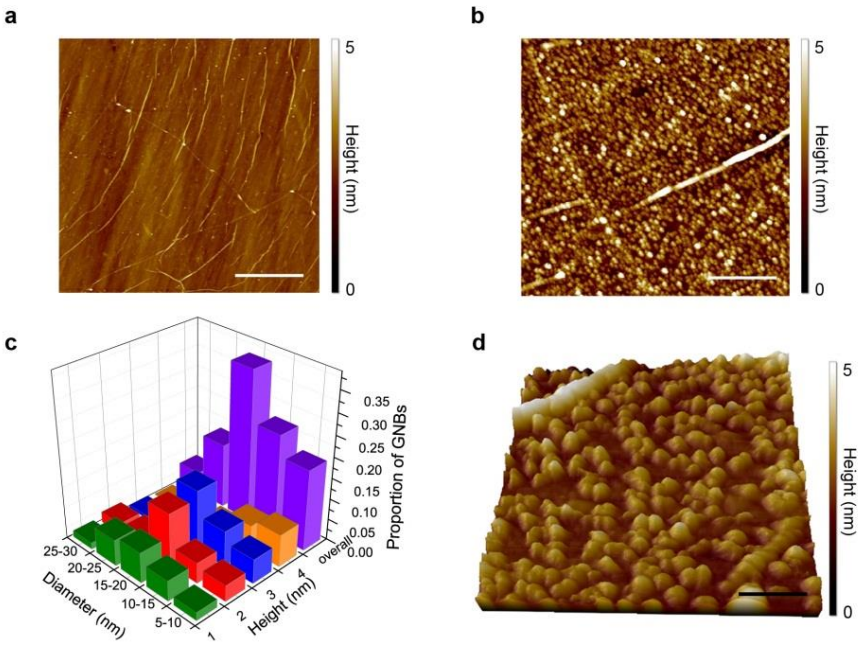

Figure 5.2 AFM images of GNBs. (a) Topography of G on diamond after transfer. (b) Topography of GNBs on diamond. Scale bar, 500 nm (a and b). (c) Histogram of the diameter and height distribution of GNBs and (d) High-resolution three-dimensional topography representation of GNBs on diamond, Scale bar, 100 nm.

The annealing temperature of 1,275K causes the dehydrogenation of the hydrogen-terminated diamond (100). Dangling bonds which are created during dehydrogenation, bond instantaneously with graphene sheet, and the non-bonded part of the graphene sheet buckles to relieve the compressive stress arising from the interfacial bonding. This reconstruction process happens spontaneously once the interface is activated thermally, as can be seen from the molecular dynamics (MD) simulations presented later (Fig 5.6). We have carried out control studies on mechanically exfoliated graphene and found that GNBs of similar size and density can be generated for wet-transferred exfoliated graphene sheet on diamond, thus the bubble formation is not specifically influenced by the grain boundaries since the sizes of

crystalline domains are expected to be quite different in CVD and exfoliated graphene (see Fig 5.3).

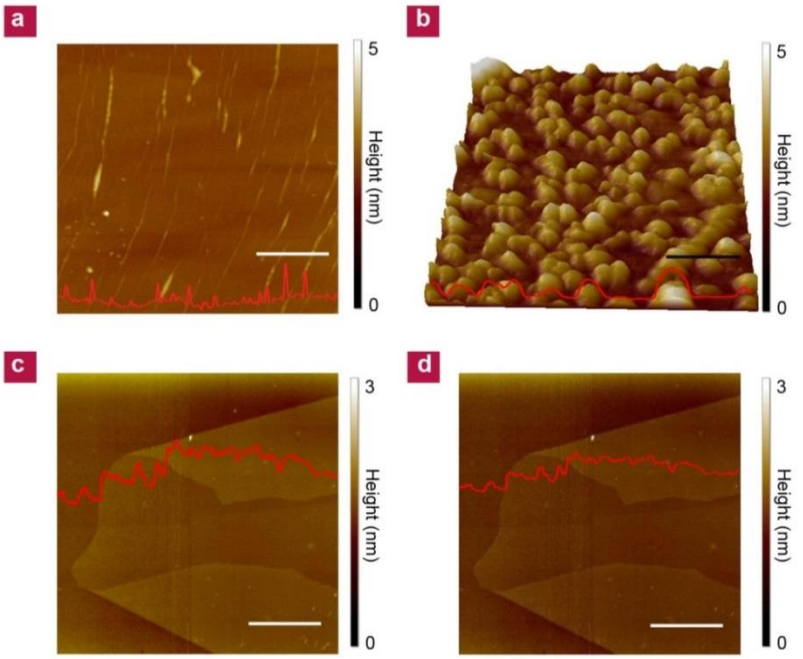

Figure 5.3 AFM images of exfoliated graphene on diamond. a and b via wet transfer technique (a) before heat treatment (b) after heat treatment and c and d via dry transfer technique (c) before heat treatment and (d) after heat treatment . The scale bars in a, c and d are 500 nm while the scale bar in b corresponds to 100 nm.

Valence band spectroscopy in Fig. 5.4a revealed the intensity of the characteristic p orbital peak in graphene was reduced with the formation of GNBs; we deduce that this is due to partial re-hybridization of its molecular orbitals following interfacial bonding with diamond.

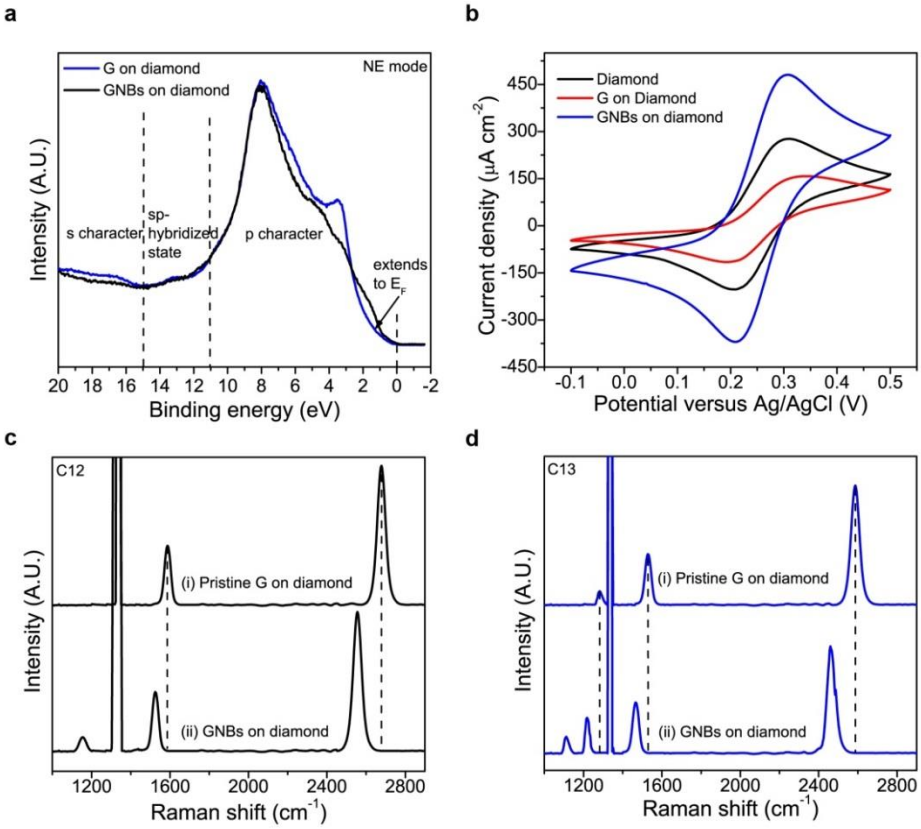

Figure 5.4 Probing the electronic structure and properties before and after the formation of GNBs. (a) Valence bands of flat G and GNB on diamond. (b) Electrochemical cyclic voltammetry of diamond, graphene-on-diamond and GNBs-on-diamond using $Fe(CN)_6^{3-/4-}$ in 1M KCl. (c) C12 Raman spectra of (i) flat graphene-on-diamond before GNB formation, (ii) GNBs on diamond and (d) C13 Raman spectra of (i) flat graphene-on-diamond and (ii) GNBs on diamond.

5.3.2 Strained GNBs

Strain, which affects the phonon frequency and which depends on the anharmonicity of the interatomic potentials, can be studied using Raman spectroscopy[12]. Sp^2 hybridized CVD graphene layer is characterised by its G, D and 2D peaks, which reside at 1,580, 1,360 and 2,680 cm^{-1} respectively[22]. G

peak corresponds to the doubly degenerate E_{2g} phonon at the Brillouin zone center. The 2D peak (second order D peak) originates from a scattering process where momentum conservation is obtained by the participation of two phonons with opposite wavevectors (***q*** and –***q***). The D peak is usually selection-rule forbidden but is activated by lattice defects. Raman spectrum was recorded using a scanning atomic force microscope (AFM)-Raman probe so that the Raman features collected from a region which is covered densely by the GNB can be contrasted with another region where the graphene is relatively flat. Figure 5.4c shows that the Raman spectrum collected from the GNB-covered region is red-shifted as compared to spectrum recorded at the flat regions. This can be explained by the elongation of C-C bonds in the tensile strained GNB. In particular, the G peak position decreases from 1,586 to 1,525 cm^{-1}, while the 2D band shifts from 2,678 to 2,553 cm^{-1} when moving from the flat to curved regions. The full-width-at- half-maximum (FWHM) of the 2D peak remains unchanged at about 30 cm^{-1}. These observations suggest that the lattice of graphene is biaxially strained[23]. Using $d\omega/d\varepsilon$, where ω is the Raman frequency and ε is the % strain applied to CVD graphene[24], the Grüneisen parameter γ was calculated to be γ =1.30 using the equation[25] $\gamma = -1/\omega_o(d\omega/d\varepsilon)$, where ω_o is the Raman frequency with no applied strain. The strain value experienced by GNBs is then calculated to be ~1.5 %. However the strain value probed by Raman spectroscopy here is underestimated due to the large laser spot size of the Raman probe relative to individual nanobubbles. Alternatively, the strain quantification of each individual GNB can be judged from its physical parameters. Since $\sigma = pr^2/2th$, strain is related to stress by $\varepsilon = (1-\nu^2)/E)\sigma$, where σ is the stress experienced at the apex of the graphene

bubble, p is the differential pressure across the membrane responsible for the magnitude of deflection, r is the radius of the GNB, t is the thickness of graphene and h is the height of GNB. Using AFM to determine the mean r and h of the bubbles, ε was estimated to be ~6%.

Besides the commonly observed G and 2D bands in pristine graphene, an unusual peak residing at ~1,150 cm^{-1} is observed to emerge upon the formation of GNBs (Fig. 5.4c). This peak is often recognized as the fingerprint band of nanocrystalline diamond crystals. Ferrari *et al* assigned it to mixed sp^3-sp^2 bonded phases and trans-polyacetylene groups present on the surface and grain boundaries of nanocrystalline diamond[26]. One possibility is the bonding of diamond to graphene breaks the honeycomb sheet into mixed sp^3-sp^2 bonded phases, and trans-polyacetylene domains appear on the modified graphene which is bonded to diamond. At the same time, a widening of the FWHM of the 1,332 cm^{-1} peak (Fig. 5.4c) is observed with the growth of GNBs, and this can be attributed to the increased density of defects following interfacial bonding. To avoid the overlap between the defect peak of graphene and the first order phonon peak of single crystal diamond (situated at 1,332 cm^{-1}), the Raman spectrum of C13-enriched graphene was recorded. The D peak of graphene, which is defect-related, is observed to increase with the formation of GNBs (Fig. 5.4d) and similar downshifting of the G and 2D peaks is also observed for the curved regions of the GNBs.

5.3.3 Unique properties of GNBs

Pristine graphene shows excellent in-plane electrical conductivity. However due to the anisotropic nature of its electron delocalisation, it is known to be electrochemically sluggish for charge transfer in the direction normal to its basal plane[27]. An exception is found however in the case of GNB, since its strained surfaces means the flat lying 2*p* orbitals are distorted, and midgap states will be created to which enhanced charge transfer can occur. The curvature in GNB also causes an asymmetric distribution of π electrons outside and inside graphene sheet[28], bestowing greater electrochemical reactivity on its exterior. Cyclic voltammetry of $Fe(CN)_6^{3-/4-}$ redox couple was selected to examine the heterogenous charge transfer mechanism before and after the formation of GNBs. In this case the graphene sheet is transferred to a conducting, boron-doped diamond crystal. Using an inner sphere redox couple, which is sensitive to both the density of electronic states and surface microstructure, charge transfer kinetics can be calculated from the peak-to-peak separation in the voltammograms (Fig. 5.4b). The results show that the charge transfer rate follows the order of: GNBs on diamond > diamond > flat G-on-diamond, as summarized in Table 5.1. The cathodic and anodic currents of GNBs on boron-doped diamond electrode (Fig 5.5) show a linear relationship with the square root of the scan rated ranging from 25 to 125 mV s^{-1}, which is in good agreement with the Randles Sevcik equation describing reversible reactions controlled by semi-infinite linear diffusion. Boron-doped diamond is known to be a good electrode for electrochemistry, but what is

striking here is the enhanced electrochemical response when its surface is modified by GNBs.

Table 5.1 Calculated apparent heterogeneous electron-transfer rate constants and capacitances.

Electrode	ΔEp (mV)	Rate constant k (cm s^{-1})	Capacitance at 0.3 V (μF cm^{-2})
Diamond	105±21	0.0740±0.005	207.7±18
G on diamond	146±18	0.00277±0.003	34.27±8
GNBs on diamond	89±15	0.0909±0.001	397.4±7

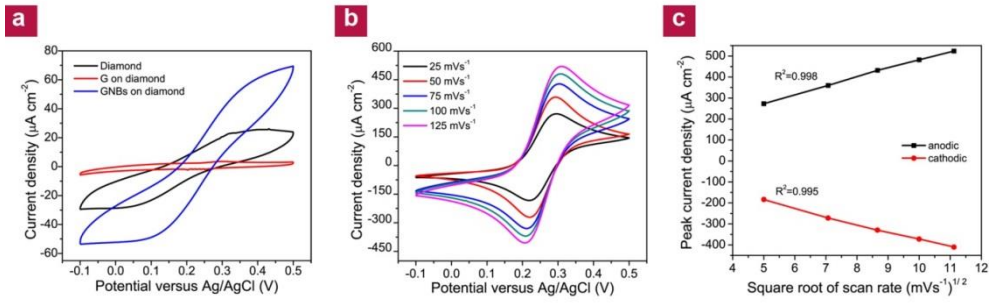

Figure 5.5 Cyclic voltammetry recorded for diamond, graphene on diamond and GNBs on diamond (a) 1 M KCl, scan rate: 100 mV s^{-1}. (b) CVs recorded at GNBs on diamond electrode in 1.0 mM $Fe(CN)_6^{3-/4-}$ in 1 M KCl at various scan rates and (c) peak current dependence on the square root of scan rate.

5.3.4 Insights to the formation of GNBs

The GNB-on-diamond sample was introduced into a Fourier Transform Infrared Spectroscopy (FTIR) in-situ cell evacuated to 1×10^{-4} Torr. FTIR measurements reveals that residual water from the graphene transfer

process is trapped at the GNB-diamond interface due to the impermeability of graphene[29] (Fig 5.6d). Surface physisorbed water typically desorbs readily in vacuum once the sample is heated slightly due to its weak adsorption energies on hydrophobic surface. However we observed that the water-related OH vibrational bands persist up to the highest heating temperature in GNB-on-diamond (>773 K), this is possible only if the water molecules are trapped at the GNB-diamond interface. The observation of trapped water echoes a recent study which demonstrated the imaging of trapped water between two graphene membranes using high resolution transmission electron microscopy[30]. It is worth mentioning also that the impermeablity of the graphene membrane to atoms and molecules has been predicted by Leenaerts *et al* [31] using first-principles density functional theory investigation.

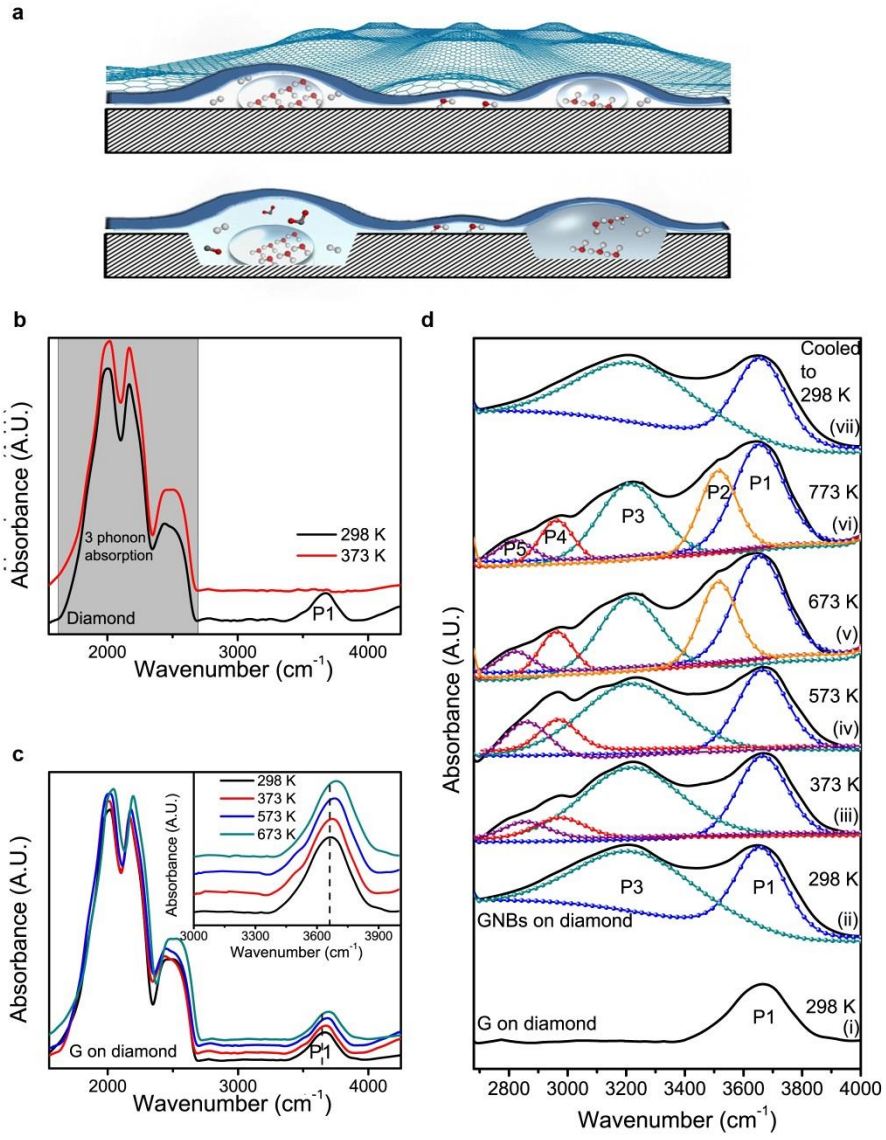

Figure 5.6 Schematic diagram and vibrational spectroscopy of graphene and diamond. (a) Schematic representation showing water cluster in GNB and weakly interacted water molecules underneath flat G on diamond (top panel). Etching of diamond by supercritical water (bottom panel). FTIR spectra showing OH-stretching peak of water measured on (b) diamond, where raising temperature to 373 K results in the desorption of water (c) Flat G on diamond showing peak at 3,650 cm^{-1} due to the presence of trapped, weakly bonded water molecules (d) (i) Flat G on diamond, (ii)-(vi) After formation of GNB at a range of temperatures and (vii) Cooling own to room temperature.

The OH stretch of water presents an extremely broad band between 3,000 to 3,700 cm^{-1}, which is usually described by the four state-model[32] in terms of

the strength of hydrogen bonding. The intra-molecular OH stretch is highly dependent on the hydrogen bond coordination of the proton[33]. A strong hydrogen bonding results in a weakening of the OH oscillator, a red shift in energy and a broadening of the spectral peak. As shown in Fig. 5.6d, a relatively sharp peak labelled as P1 at ~3,650 cm^{-1}, which is characteristic of free OH bond of water molecules, is observed at the bare diamond surface but this peak vanishes upon slight heating, and only the intrinsic 3 phonon absorption signature of diamond[34] (Fig. 5.6b) remain. Thus we can conclude that ambient-absorbed water cannot remain on the surface at elevated temperatures without some form of trapping. Peak P1 is also observed at diamond surface encapsulated by flat graphene sheet (Fig. 5.6c) but it survives even after high temperature annealing, suggesting that trapped water on diamond is sealed by graphene. The persistence of P1 as temperature increases suggests that a large body of water molecules adsorbing on hydrophobic surface have weak hydrogen bonding interactions. In the case of GNB-diamond, it is noteworthy that in addition to P1, a red-shifted broad band (P3) at ~3,220 cm^{-1} which is characteristic of strong hydrogen bonding is present at room temperature. P3 can be assigned to the condensation of water inside the bubbles. When the GNB-diamond sample is heated to increasingly higher temperature, another red-shifted P4 peak at 2,967 cm^{-1} emerges, which is indicative of increased clustering. At 673 K, the intensity of the 3,220 cm^{-1} peak is observed to weaken and a blue shifted sharp peak P2 appears at 3,510 cm^{-1}. At this point, the weakening of the hydrogen bonding can be interpreted as the emergence of supercritical phase in some of the bubbles[35-37]. Previously, Tassaing *et al* observed a broadening of vibrational bands leading to a broad

band with 2 maxima at about 3,650 and 3,550 cm^{-1} and a shoulder at 3,250 cm^{-1} as water approaches critical conditions[36]. The critical temperature of water is 647 K, and the properties of water above 674 K and at pressures higher than 2.21 MPa (critical pressure) differ significantly from those of ambient water. Supercritical water has a density between that of water vapor and liquid at standard conditions, reduced intermolecular bonding and exhibits high gas-like diffusion rates along with high liquid-like collision rates. A significantly reduced dielectric constant[38] (~20) allows it to act as an aggressive solvent for organic material. From the IR spectra, it can be inferred that the trapped water molecules are rather inhomogeneous in its bonding environment; some water molecules trapped in the bubble undergoes clustering as pressure (temperature) increases, as reflected from increasingly stronger hydrogen bonding environment (P4 & P5), while other water molecules, possibly trapped under flat part of the graphene sheet, do not cluster, as judged from the persistence of peak P1. It must be pointed out that peaks P2, P4 and P5 are dynamic features present only at high temperatures, they decrease in intensities once the sample is cooled to room temperature (Fig. 5.6d-vii).

5.3.5 GNBs as high pressure reactors for etching of diamond

After heating the GNB-diamond sample over 1 hour at 1,375 K, numerous nanometer-sized square voids appear on the diamond surface with a density of 9×10^{9} cm^{-2}. Fig. 5.7e shows the scanning electron microscope (SEM) image of these nanovoids which have an average width of ~ 40 nm.

The square etched pits follow the crystallographic expectation of the [100] faceted diamond. The occurrence of etched pits is intriguing as vigorous chemical or physical treatments, in the presence of transition metal catalysts, are usually needed to etch diamond. Control studies where the diamond crystals are heated alone in air or in vacuum at the same temperature fail to reproduce the etched pits in the absence of the graphene membrane. At elevated temperatures, GNBs can be transformed into a hydrothermal reactor due to its impermeability[26,39]. Trapped water molecules inside can be transformed into supercritical fluid, which is highly corrosive to organic medium. For example, supercritical water has been used in the oxidation of methane to produce CO and CO_2 at 25 MPa and temperature above 773 K[40].

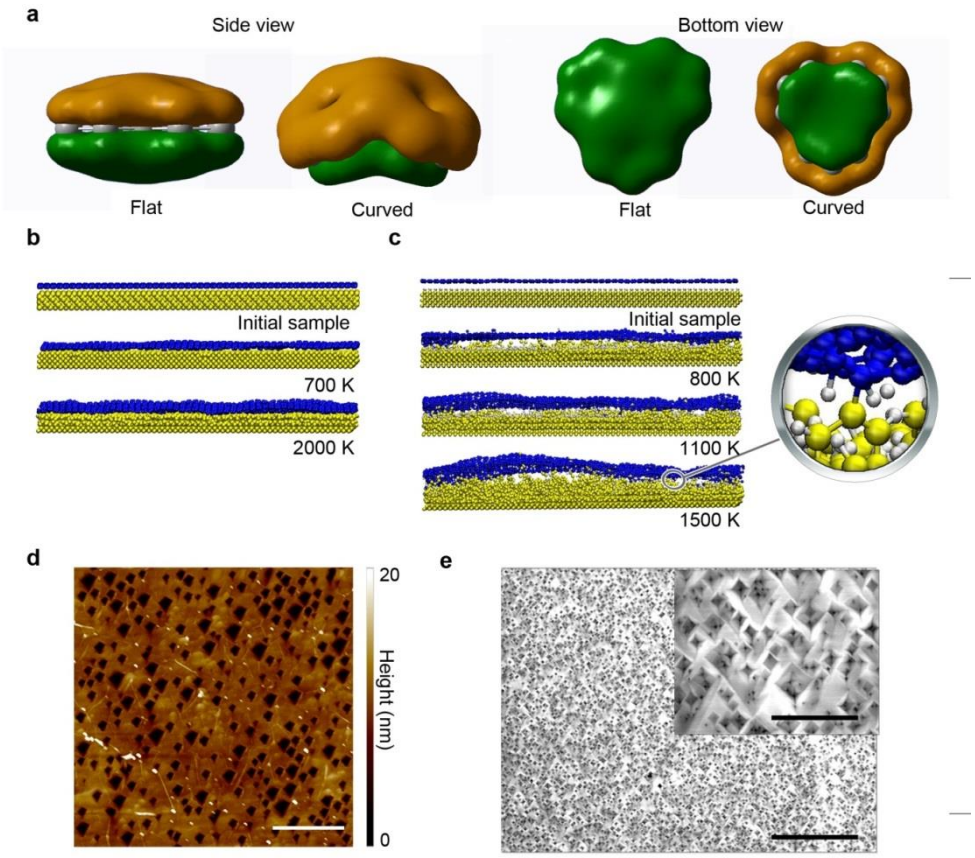

Figure 5.7 GNB formation, growth and void generation on diamond. (a) Density functional theory simulation of ground electronic state of flat and curved graphene at B3LYP/6-31 G* level. (b,c) MD simulation of the buckling of graphene on diamond (b) Graphene on C(100)-(2X1). (c) Graphene on dihydride-terminated diamond (denoted as 2H C(100) – (2 x1), where bubble formation can be seem after heating (d) AFM topography image of voids generated on diamond and (e) Scanning electron microscope image of etched diamond, and inset is image zoomed in by 20 times. Scale bar, 0.3, 1 and 0.05 μm, respectively (d, e and inset of e, respectively).

The pressure inside a GNB can be estimated from its deformation from a flat membrane using Hencky's solution for the geometrically nonlinear response of an isotropic elastic membrane subjected to a pressure difference Δp across the membrane. This solution provides the membrane profile in the form of an infinite series in radial position, and also the relationship between the pressure difference and bubble height, $\Delta p = K(\nu)\ (Eth^3)/r^4$. Here E is the Young's

modulus, ν is Poisson ratio, *t* is the membrane thickness, *r* is the radius of the bubble and *K*(ν) is the coefficient that is dependent on the Poisson ratio. For graphene, we take ν =0.16 and so *K*(ν =0.16) = 3.09 ([41]). The mean h and *r* values derived from AFM imaging are employed for estimation of pressure difference across a typical GNB. The pressure that is built up in a typical GNB of 2 nm in height and 10 nm in radius is calculated to be approximately 1 GPa. Alternatively, by considering a monolayer of water adsorbed on the surface of diamond and trapped within the GNB, the pressure estimated in the bubble using ideal gas law also arrived at a value of *ca.* 1 GPa. This value obtained lies within the pressure-temperature regime where etching of diamond is possible[42]. The etching of diamond octahedrons at 1,375 K and 10^9 Pa has been previously reported with water and oxygen serving as etchants[42,43]. Inside the bubbles, the superheated water is known to have enhanced solubility for non-polar organic materials.

It is interesting to reflect on the chemical robustness of the GNB relative to the diamond which it is encapsulating. Fig. 5.7a shows the p_z orbital isosurface wavefunction (isoval= 0.02 a.u.) of flat and curved graphene calculated using density functional theory (DFT, at B3LYP/6-31G*). In contrast to the evenly distributed electronic density of a flat graphene plane, the curvature in GNB produces an asymmetric distribution of π electrons on its outer and inner surface. Outward rotation of orbitals enhances local density of states and bestows higher reactivity on the outer surface of the GNB. In contrast, orbitals at the inner surface of the GNB (Fig. 5.7a) are rotated inwards to result in a diminished electron cloud, thus resulting in reduced reactivity of concaved graphene surface[44].

With increasing temperature, the GNB bursts finally, and remnants of the torn graphene sheets can be observed using AFM imaging (Fig. 5.7d). Raman spectroscopy of the surface at this point reveals poly-acetylene like fragments on the pit-covered diamond (Fig 5.8).

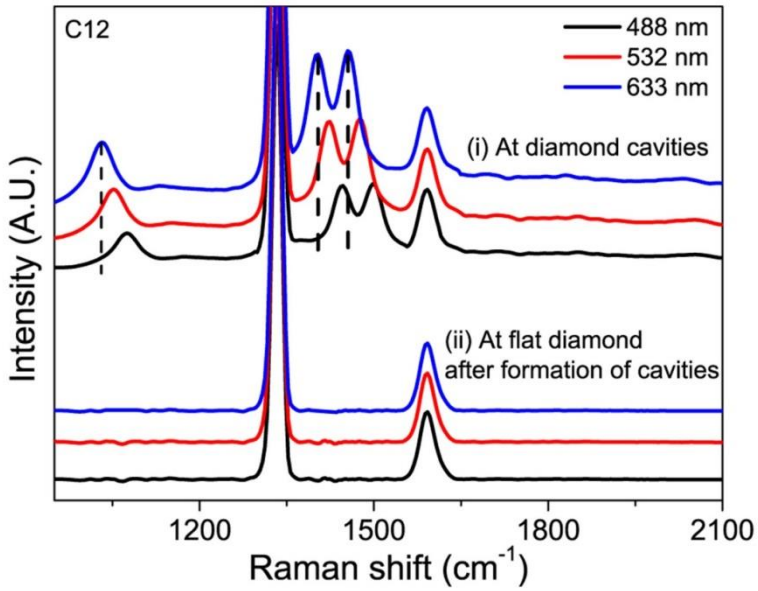

Figure 5.8 Raman spectra after formation of diamond cavities as a function of excitation wavelength (i) At diamond cavities (ii) At flat diamond after formation of cavities.

To obtain an atomistic insight into the formation mechanism of GNBs on diamond, we carried out classical MD simulations using reactive empirical bond-order potential (REBO)[18,19] and ReaxFF[20] (reactive force field). Diamond (C(100) surface atom density : 1.56×10^{15} atoms cm^{-2}) slab (35nm×35 nm×0.45 nm) was built by 6 layers of atoms, each containing 20,000 atoms. Graphene (C(0001) surface atom density: 3.65×10^{15} atoms cm^{-2}) sheet containing 48,720 atoms was placed Z= 2.5 Å away from the surface

of diamond to ensure that graphene and diamond are not covalently bonded at first.

We first test the possibility of bonding interactions between graphene and a bare diamond surface. The bare diamond surface is a reconstructed (100)-(2×1) surface truncated by dimer row formation. No interfacial bonding between diamond and graphene is observed when the system is heated to 700 K, and only a minor rippling of graphene is observed (see Fig. 5.7b at 700 K). The reason of the rippling is the lattice mismatch between diamond (100) and graphene. The amplitude of rippling increases with further heating, however even at 2000 K the height of the ripples does not exceed 5-5.5 Å (Fig. 5.7b at 2,000 K).

A different situation exists when a dihydride-terminated (denoted as 2H: C(100)-(2×1)) diamond surface interacts with graphene (Fig. 5.7c). Upon thermally induced desorption of hydrogen atoms at 1,100 K, MD simulation shows clearly that graphene-diamond bonding occurs instantaneously (Fig. 5.7c). The graphene-diamond bonding produces ripples on graphene sheet. At 1,500 K and higher, part of graphene sheet erupts into bubbles (Fig. 5.7c at 1,500 K) due to pressure by desorbing hydrogen molecules. At elevated pressures, breakage of interfacial C-C bonds between graphene and diamond resulted in the delamination of GNB from diamond surface.

These simulations confirm that the formation of GNB on the diamond surface is initiated by the interfacial bonding between diamond and graphene. Interfacial bonding seals the edges and prevents the graphene sheet from delaminating from diamond, thus desorbed gaseous species are trapped

effectively within the bubbles. Gasification of surface adsorbed species like hydrogen and water create pressure inside the bubble due to impermeability of graphene membrane. It can be appreciated that the size of the bubble will scale with the amount of trapped water molecules, which is confirmed by our experiments on oxygenated diamond surfaces (Fig. 5.9 and Table 5.2). The ability of graphene to undergo out-of-plane bonding with diamond is essential for sealing the edges of the bubble, otherwise on non-bonding substrate, a decohesion of the graphene membrane occurs and no bubble formation occurs (refer to Fig 5.9).

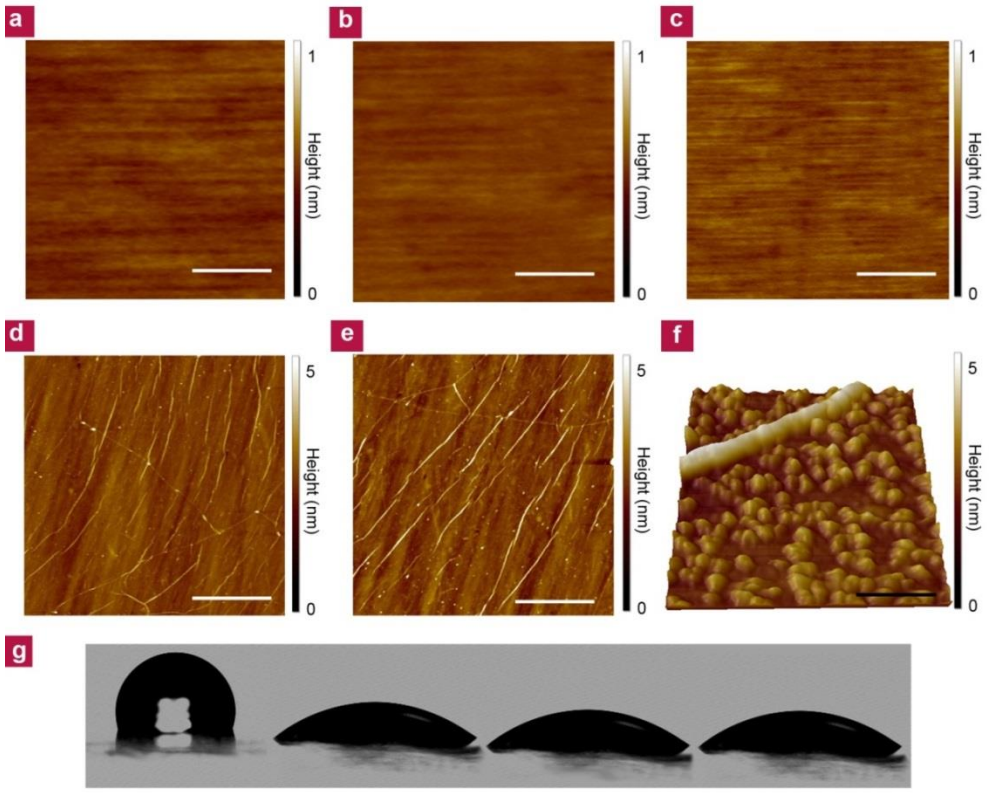

Figure 5.9 AFM topography and surface properties of sapphire,quartz and O-diamond substrates and graphene on respective substrates. (a-c) Surface topography of bare substrates (a) Sapphire, (b) Quartz, (c) O-diamond, (d) Graphene on sapphire and (e) Graphene on quartz. The scale bars in a- e are 500 nm. (f) High resolution 3D topography representation of GNBs on O-diamond. The corresponding scale bar shown is 100 nm and (g) Contact angle images of H-diamond, O-diamond, sapphire and quartz (from left to right).

Table 5.2 Table summarizing the contact angle, interfacial thickness lost after annealing at 623 K and experimentally determined density, diameter and height of GNBs.

Substrate	Contact angle	Inter-facial thickness (nm)	Forma-tion of GNBs	Areal density ($X10^{10}$ cm^{-2})	Diameter of GNBs (nm)	Height of GNBs (nm)
H-diamond	106^{o}	0.1	Yes	8	5-30	~3
O-diamond	35^{o}	0.18	Yes	7	15-40	~5
Sapphire	38^{o}	0.17	No			
Quartz	33^{o}	0.28	No			

The technological implication of the present work extends to supercritical fluid assisted etching of solid surfaces as well as new types of high pressure anvil cell using graphene membrane. Due to the transparency and high thermal conductivity of graphene, it can serve as an optical window for laser-assisted etching where exponential increase in etch rates can be brought about by the synergistic effects of photo-excitation and ultrahigh pressure. Finally, the encapsulation of fluids between graphene bubbles and diamond allow supercritical fluids to be probed spectroscopically using a wide range of radiation from X-ray, infrared light to gamma rays.

5.4 Conclusion

The graphene-diamond interface can be transformed into an undulating sheet of graphene nanobubbles which act as hydrothermal anvil cells. There are several important outcomes. First, the GNB decorated surface shows enhanced electrochemical activity compared to flat graphene, which can be ascribed to its highly strained structure. Second, superheated water trapped inside the GNB is highly corrosive and etches diamond. Vibrational spectroscopy shows that the OH absorption band of the trapped water can be qualitatively considered as the sum of the individual spectra of water clusters. Weakly interacting water molecules adsorb between the flat region of the graphene and diamond, while strongly clustered water molecules occur inside the bubbles. This work shows the first example of using an impermeable

atomic membrane for trapping fluid at supercritical conditions, where the power of superheated water in corroding diamond is observed.

5.5 References

1 Bao, W. *et al.* Controlled ripple texturing of suspended graphene and ultrathin graphite membranes. *Nature Nanotechnology* **4**, 562-566 (2009).

2 Bolotin, K. I., Sikes, K. J., Hone, J., Stormer, H. L. & Kim, P. Temperature-dependent transport in suspended graphene. *Physical Review Letters* **101** 096802 (2008).

3 Meyer, J. C. *et al.* The structure of suspended graphene sheets. *Nature* **446**, 60-63 (2007).

4 Berger, C. *et al.* Electronic confinement and coherence in patterned epitaxial graphene. *Science* **312**, 1191-1196 (2006).

5 Xue, J. *et al.* Scanning tunnelling microscopy and spectroscopy of ultra-flat graphene on hexagonal boron nitride. *Nature Materials* **10**, 282-285 (2011).

6 Dean, C. R. *et al.* Boron nitride substrates for high-quality graphene electronics. *Nature Nanotechnology* **5**, 722-726 (2010).

7 Pan, W. *et al.* Biaxial compressive strain engineering in graphene/boron nitride heterostructures. *Scientific Reports* **2** 893 (2012).

8 Marchini, S., Günther, S. & Wintterlin, J. Scanning tunneling microscopy of graphene on Ru(0001). *Physical Review B - Condensed Matter and Materials Physics* **76** 075429 (2007).

9 Vázquez De Parga, A. L. *et al.* Periodically rippled graphene: Growth and spatially resolved electronic structure. *Physical Review Letters* **100** 056807 (2008).

10 Lu, J., Neto, A. H. C. & Loh, K. P. Transforming moire blisters into geometric graphene nano-bubbles. *Nature Communications* **3** 823 (2012).

11 Stolyarova, E. *et al.* Observation of graphene bubbles and effective mass transport under graphene films. *Nano Letters* **9**, 332-337 (2009).

12 Zabel, J. *et al.* Raman spectroscopy of graphene and bilayer under biaxial strain: Bubbles and balloons. *Nano Letters* **12**, 617-621 (2012).

13 Bundy, F. P. Direct conversion of graphite to diamond in static pressure apparatus. *Science* **137**, 1057-1058 (1962).

14 Irifune, T., Kurio, A., Sakamoto, S., Inoue, T. & Sumiya, H. Materials: Ultrahard polycrystalline diamond from graphite. *Nature* **421**, 599-600 (2003).

15 Khaliullin, R. Z., Eshet, H., Kühne, T. D., Behler, J. & Parrinello, M. Nucleation mechanism for the direct graphite-to-diamond phase transition. *Nature Materials* **10**, 693-697 (2011).

16 Ohfuji, H. & Kuroki, K. Origin of unique microstructures in nano-polycrystalline diamond synthesized by direct conversion of graphite at static high pressure. *Journal of Mineralogical and Petrological Sciences* **104**, 307-312 (2009).

17 Li, X. *et al.* Large-area synthesis of high-quality and uniform graphene films on copper foils. *Science* **324**, 1312-1314 (2009).

18 Brenner, D. W. Empirical potential for hydrocarbons for use in simulating the chemical vapor deposition of diamond films. *Physical Review B* **42**, 9458-9471 (1990).

19 Brenner, D. W. Erratum: Empirical potential for hydrocarbons for use in simulating the chemical vapor deposition of diamond films (Physical Review B (1992) 46, 3). *Physical Review B* **46**, 1948 (1992).

20 Van Duin, A. C. T., Dasgupta, S., Lorant, F. & Goddard Iii, W. A. ReaxFF: A reactive force field for hydrocarbons. *Journal of Physical Chemistry A* **105**, 9396-9409 (2001).

21 Plimpton, S. Fast parallel algorithms for short-range molecular dynamics. *Journal of Computational Physics* **117**, 1-19 (1995).

22 Ferrari, A. C. & Robertson, J. Resonant raman spectroscopy of disordered, amorphous, and diamondlike carbon. *Physical Review B - Condensed Matter and Materials Physics* **64**, 754141-7541413 (2001).

23 Ni, Z. H. *et al.* Tunable stress and controlled thickness modification in graphene by annealing. *ACS Nano* **2**, 1033-1039 (2008).

24 Bissett, M. A., Izumida, W., Saito, R. & Ago, H. Effect of Domain Boundaries on the Raman Spectra of Mechanically Strained Graphene. *ACS Nano* **6**, 10229-10238 (2012).

25 Mohiuddin, T. M. G. *et al.* Uniaxial strain in graphene by Raman spectroscopy: G peak splitting, Grüneisen parameters, and sample orientation. *Physical Review B - Condensed Matter and Materials Physics* **79** 205433 (2009).

26 Ferrari, A. C. & Robertson, J. Origin of the 1150-cm-1 Raman mode in nanocrystalline diamond. *Physical Review B - Condensed Matter and Materials Physics* **63**, 1214051-1214054 (2001).

27 Lim, C. X., Hoh, H. Y., Ang, P. K. & Loh, K. P. Direct voltammetric detection of DNA and pH sensing on epitaxial graphene: An insight into the role of oxygenated defects. *Analytical Chemistry* **82**, 7387-7393 (2010).

28 Yuan, Q. *et al.* Upright standing graphene formation on substrates. *Journal of the American Chemical Society* **133**, 16072-16079 (2011).

29 Bunch, J. S. *et al.* Impermeable atomic membranes from graphene sheets. *Nano Letters* **8**, 2458-2462 (2008).

30 Yuk, J. M. *et al.* High-resolution EM of colloidal nanocrystal growth using graphene liquid cells. *Science* **335**, 61-64 (2012).

31 Leenaerts, O., Partoens, B. & Peeters, F. M. Graphene: A perfect nanoballoon. *Applied Physics Letters* **93** 193107 (2008).

32 Lasagabaster, A., Abad, M. J., Barral, L. & Ares, A. FTIR study on the nature of water sorbed in polypropylene (PP)/ethylene alcohol vinyl (EVOH) films. *European Polymer Journal* **42**, 3121-3132 (2006).

33 Loparo, J. J., Roberts, S. T. & Tokmakoff, A. Multidimensional infrared spectroscopy of water. II. Hydrogen bond switching dynamics. *Journal of Chemical Physics* **125** 194522 (2006).

34 Charles, S. J. *et al.* Characterization of nitrogen doped chemical vapor deposited single crystal diamond before and after high pressure, high temperature annealing. *Physica Status Solidi (A) Applied Research* **201**, 2473-2485 (2004).

35 Jin, Y. & Ikawa, S. I. Near-infrared spectroscopic study of water at high temperatures and pressures. *Journal of Chemical Physics* **119**, 12432-12438 (2003).

36 Tassaing, T., Garrain, P. A., Ḃgú, D. & Baraille, I. On the cluster composition of supercritical water combining molecular modeling and vibrational spectroscopic data. *Journal of Chemical Physics* **133** 034103 (2010).

37 Marcus, Y. Supercritical water: Relationships of certain measured properties to the extent of hydrogen bonding obtained from a semi-empirical model. *Physical Chemistry Chemical Physics* **2**, 1465-1472 (2000).

38 Yoshii, N., Miura, S. & Okazaki, S. A molecular dynamics study of dielectric constant of water from ambient to sub- and supercritical conditions using a fluctuating-charge potential model. *Chemical Physics Letters* **345**, 195-200 (2001).

39 Xu, K., Cao, P. & Heath, J. R. Graphene visualizes the first water adlayers on mica at ambient conditions. *Science* **329**, 1188-1191 (2010).

40 Webley, P. A. & Tester, J. W. Fundamental kinetics of methane oxidation in supercritical water. *Energy & Fuels* **5**, 411-419 (1991).

41 Koenig, S. P., Boddeti, N. G., Dunn, M. L. & Bunch, J. S. Ultrastrong adhesion of graphene membranes. *Nature Nanotechnology* **6**, 543-546 (2011).

42 Yamaoka, S., Kanda, H. & Setaka, N. Etching of diamond octahedrons at high temperatures and pressure with controlled oxygen partial pressure. *Journal of Materials Science* **15**, 332-336 (1980).

43 Kanda, H., Yamaoka, S., Setaka, N. & Komatsu, H. Etching of diamond octahedrons by high pressure water. *Journal of Crystal Growth* **38**, 1-7 (1977).

44 Cortijo, A. & Vozmediano, M. A. H. Electronic properties of curved graphene sheets. *EPL* **77** 47002 (2007).

Chapter 6

Observing high pressure chemistry in graphene bubbles

Abstract:

We observed high pressure (GPa)-induced conformational changes and cycloadditon reactions in a bench-top hydrothermal anvil cell constructed by trapping liquid medium in graphene nanobubbles formed at the graphene-diamond interface. The nanobubbles that form as a result of thermally induced bonding of graphene and diamond at the interface are highly impermeable and function well as optically transparent, pressurized nanoreactors which allow high pressure chemical reactions to be probed with vibrational spectroscopy. By monitoring the conformational changes of pressure-sensitive molecules, the pressure within the nanobubble could be tracked as a function of temperature and was found to be at ~1 GPa at 600 K. The polymerization of buckminsterfullerene (C_{60}), which is symmetrically forbidden under ambient conditions, was observed to proceed in well-defined stages in the pressurized nanobubbles.

6.1 Introduction

Pressure is a fundamental physical property that influences thermodynamic equilibrium, changes kinetics and cause changes in states of matter. Chemical reactions, which are forbidden under normal conditions due to steric hindrance or stereoelectronic factors can be driven by pressure[1]. High pressure modifies the electronic structure of the molecule and affects the regioselectivity of the reactions. The rate and equilibrium of many chemical reactions are influenced when pressure in the range of 1-20 kbar are applied[2]. In general, reactions which are accompanied by a decrease in volume, such as C-C bond formation, are accelerated by pressure (activation volume $\Delta V^{\neq}<0$) and equilibrium is shifted towards the side of the products (reaction volume $\Delta V<0$).

An example of a pressure-sensitive reaction is cycloaddition reaction. The activation $\Delta V^{\neq}$ and reaction volumes ΔV are highly negative (eg. $\Delta V^{\neq} \approx$ -25 to -50 cm^3mol^{-1}) in these reactions[3]. The activation volumes of [2+2] cycloaddition reactions are highly negative ($\Delta V^{\neq} \approx$ -25 to -52 cm^3mol^{-1}). Hence, the application of pressure leads to a considerable acceleration of its reaction rate. For instance, under high pressure conditions (15 kbar), 4-methyl phenyl 1,2-prop-adienyl sulfones and enol ether undergo a regioselective [2+2] cycloaddition to give (3-alkoxycyclobutylidene) methyl 4-methylphenyl sulfones in good yield, while this reaction is forbidden at atmospheric pressure[4].Aben *et al* also reported the reaction involving enol ethers and alkyl 3-aryl-2 cano-2-propenoates at high pressure to give cycloadducts in high yields and stereoselectivities[5]. To enable the study of high pressure chemistry, researchers have developed various types of windowed pressure cells for high

pressure experiments (P>100 GPa) to be carried out in the laboratory. The diamond anvil cell (DAC) is the most widely used due to the transparency of diamond across the electromagnetic spectrum, making the performance of high pressure spectroscopy possible. However, the alignment of the two diamond cutlets is not trivial as they must be placed perfectly parallel for uniform pressure and to prevent cracks.

AFM nanoidentation studies reveal that graphene has an intrinsic breaking strength of 42 Nm^{-1}, capable of withstanding pressures up to hundreds of gigapascals[6]. The impermeability of graphene as well as its huge elastic modulus suggest that it can be used as a barrier for entrapping fluids. However there have been no reports where graphene is used as an observation window and fluid trap in high pressure chemistry. To construct a bench-top hydrothermal anvil cell for high pressure chemical reactions, we encapsulate an optically transparent substrate, diamond, with an atomic layer of graphene and anneal the sample to the reconstruction temperature of diamond for sealing of the graphene-diamond interface. Upon thermal reconstruction, covalent bonds formed between the two dissimilar phases induce interfacial stress and rippling of graphene, since it is the softer phase. Before using the graphene bubbles as a reactor for high pressure chemical reactions, it might be useful to first correlate the pressure within the graphene nanobubble as a function of temperature. However, probing of pressure in a nano-sized bubble using conventional methods such as ruby luminescence is challenging since a ruby crystal has to be encapsulated alongside with the material under study[7].

By using pressure sensitive molecules, we can determine the pressure within the graphene bubble by following the conformation of polyphenyl

molecules spectroscopically. Beyond its critical pressure, the phenyl molecule, originally in its twisted form will flatten[8]. Finally, to test the feasibility of graphene bubbles as a high pressure anvil reactor, the polymerization of buckminsterfullerene (C_{60}) was tested within the cavity since the intermolecular coupling by cycloaddition reactions is symmetry forbidden under normal conditions.

6.2 Materials and methods

6.2.1 CVD growth and transfer of graphene

The graphene sheets used in this study were grown by CVD following previous reported procedures[9]. The process was carried out in a quartz tube at reduced pressure with copper as a catalyst for graphene growth. The copper foil (thickness of 25 μm, purity of 99.8%) was heated at 1,275 K under a 10 sccm flow of H_2 (~400 mTorr) to reduce the oxide present, increase the grain size and ensure a smooth surface for growth. Next, CH_4 was introduced into the chamber for growth. CH_4 (10 sccm) and H_2 (10 sccm) was maintained at ~750 mTorr for 30 min. Following that, the grown sheet was cooled in an atmosphere of H_2 to room temperature. The graphene on copper foil samples were coated with poly (methyl methacrylate) (PMMA) and transferred onto diamond substrates.

6.2.2 Surface preparation of single crystal diamond

Type IIa CVD single- crystal diamonds (100) were purchased from Element Six and mechanically polished to give rms <~0.2 nm before use. Acid cleaning and hydrogen-plasma cleaning of diamond were used for all diamond samples. Metallic impurities were first dissolved in hot aqua regia (HNO_3:HCl 1:3), followed by removing organic impurities from the diamond samples by hot 'piranha' solution (H_2O_2:H_2SO_4 1:3) at 375 K for 1 h. H-termination of diamond samples was performed by microwave hydrogen-plasma treatment using 800 W microwave power and 300 sccm of hydrogen gas flow for 15 min.

6.2.3 Annealing for formation of GNB

The samples were mounted on a Mo sample plate, transferred into a ultrahigh vacuum chamber with a base pressure of $<10^{-10}$ Torr. Annealing was conducted at 1,275 K for 45 min by e-beam heating (SPECS GmbH, Germany). Throughout the entire annealing process, it was ensured that the pressure did not rise beyond 10^{-8} Torr.

6.2.4 Atomic force microscopy

A Dimension ICO using Nanoscope V controller (Bruker, Santa Barbra, CA) equipped with a diamond probe (DNISP; Bruker AFM Probes, Camarillo,

CA) was operated in Peakforce Quantitative Nanomechanical mode for simultaneous topography imaging and Young's modulus mapping of the graphene bubbles.

6.2.5 FTIR for tracking of chemical reactions in GNB

FTIR measurements were conducted in the reflection mode using an OPUS/IR PS15 spectrometer (Bruker). The sample was loaded into a high-temperature high-pressure FTIR cell evacuated to 1×10^{-4} Torr. The spectra were the results of 32 coadded interferograms at 4 cm^{-1} resolution between 400 to 4,000 cm^{-1} with collection times of approximately 2 min. Each sample was analysed at least three times and results obtained were reproducible.

6.3 Results and discussion

6.3.1 Trapped liquid between graphene-diamond interface

Transfer of CVD graphene onto diamond substrate was accomplished using the conventional float-transfer technique where due to surface tension at the air-water interface, CVD graphene film floating on the surface of water entrapped water molecules on its creases and folds, and the latter are trapped when graphene is transferred onto the diamond substrate. The hydrophobicities of diamond and graphene surfaces stimulate an instability of

the planar water interface and the fluctuations of these interfaces formed can destabilize and expel the liquid contained between the hydrophobic surfaces., leading to spontaneous cavitation[10]. At spots where water was expelled, graphene adheres strongly to diamond and traps the clustered water within. Further heating of the graphene-diamond promotes bonding between sp^2 graphene and sp^3 diamond and trap pockets of water within the nanocavities.

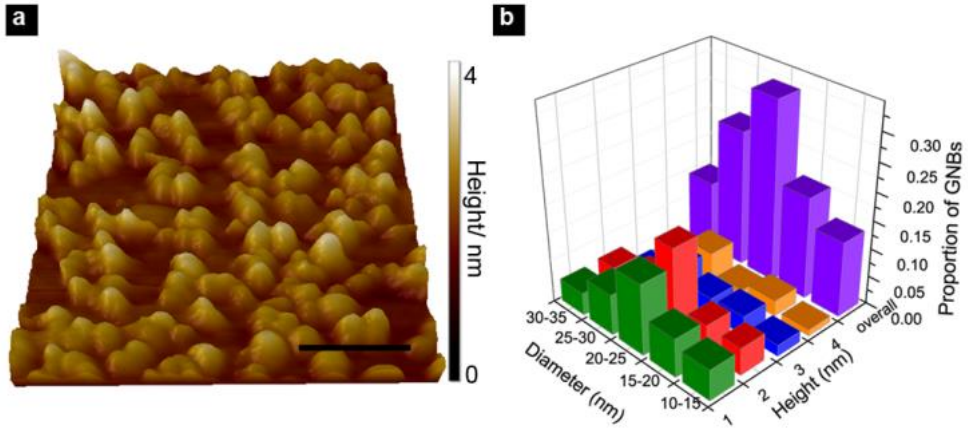

Figure 6.1 a) High resolution three-dimensional topography representation of GNBs on diamond, Scale bar, 100 nm. b) Histogram of the diameter and height distribution of GNBs.

Besides water, other solvents can also be entrapped when graphene floats on them. For example, the organic solvent carbon disulphide (CS_2) which has good solubility for polyphenyls was selected. Its IR transparency makes it a compatible solvent for subsequent *in situ* FTIR studies. The disparity in te density and sizes of the GNBs produced in different liquids is due to the difference in surface tension leading to finer corrugation of the graphene[11]. The polarity index k'of water (9.0) and CS_2 (1.0), respectively. After annealing the graphene-diamond interface at 1,275 K for 45 mins in ultrahigh vacuum, GNBs formed by encapsulating CS_2 has a density of ~5

$\times 10^{10}$ cm^{-2}, while GNBs formed by water is 1.6 times denser. (refer to Fig. 6.1). CS_2 encapsulated GNBs are on average ~ 5nm larger in diameter than water encapsulated GNBs.

6.3.2 Probing of pressure in GNB using pressure sensitive molecules

The GNB-on-diamond, which entrapped the biphenyl molecules together with the solvent CS_2, was introduced into a Fourier transform infrared spectroscopy (FTIR) *in-situ* cell evacuated to 1×10^{-4} Torr. FTIR measurements conducted at room temperature reveal the intrinsic 3 phonon absorption peaks of diamond[12] superimposed on vibrational bands associated with the twisted conformation of biphenyl (see Fig. 6.2a). It must be pointed out that in the absence of the graphene overlayer, any fluid which was introduced onto the diamond surface will evaporate readily in vacuum, which is in accordance with the inertness of the diamond surface. Thus the vibrational bands of the liquid can only be observed when it is trapped at the interface between diamond and graphene. The conformation of the biphenyl molecule at any one time is a result of the balance between the electrostatic repulsion of hydrogen atoms, which tends to twist the rings, and the interaction between π electrons, which tends to planarize the molecule[13,14]. We observed the disappearance of certain peaks in Fig. 6.2b, (these peaks correspond to the out-of-plane motion of hydrogen atoms in which the atomic displacement is perpendicular to the plane of the phenyl ring), when the sample was heated to 373 K and beyond. To obtain a rigorous basis for these

observations. group theory was applied to account for the disappearance of certain vibrational modes. Schematic representations of biphenyl in its twisted and planar form are shown in Fig. 6.2c. The twisted conformation of biphenyl belongs to the D_2 point group and the vibrational modes can be classified as follows:

$\Gamma = 15A \oplus 13B_1 \oplus 16B_2 \oplus 16B_3$.

Modes belonging to the B_1, B_2, or B_3 irreducible representations are IR-active, for a total of 45 IR-active modes. For the planar configuration, biphenyl belongs to the D_{2h} point group and the vibrational modes are given by:

$\Gamma = 11A_g \oplus 4A_u \oplus 3B_{1g} \oplus 10B_{2g} \oplus 6B_{3g}$

$\oplus 10B_{1u} \oplus 6B_{2u} \oplus 10B_{3u}$.

Modes belonging to the B_{1u}, B_{2u},or B_{3u} irreducible representations are IR-active, for a total of 26 IR-active modes. Upon planarization, some of the B_1, B_2 and B_3 modes transform into B_{1g}, B_{2g} and B_{3g} modes. These modes become IR inactive as the dipole moment vectors exactly cancel each other. The disappearance of these IR peaks was echoed in a report by Zhuravlev *et al*[15], who studied the infrared spectra of biphenyl under hydrostatic pressure using a piston-cylinder diamond-anvil cell[16]. Disappearance of similar IR peaks was observed at 0.18 GPa with the phase transition of biphenyl[15,17]. Hence, it can be inferred that the pressure in the GNB has reached the critical pressure of biphenyl when heated to 373 K. The temperature-dependent shifts of several out-of-plane hydrogen bending modes are plotted for biphenyl in Fig. 6.2d. The blue-shifting of the out-of-plane modes at higher temperature indicates the

shortening of intra-molecular C-H bond and the increase in pressure in the GNB.

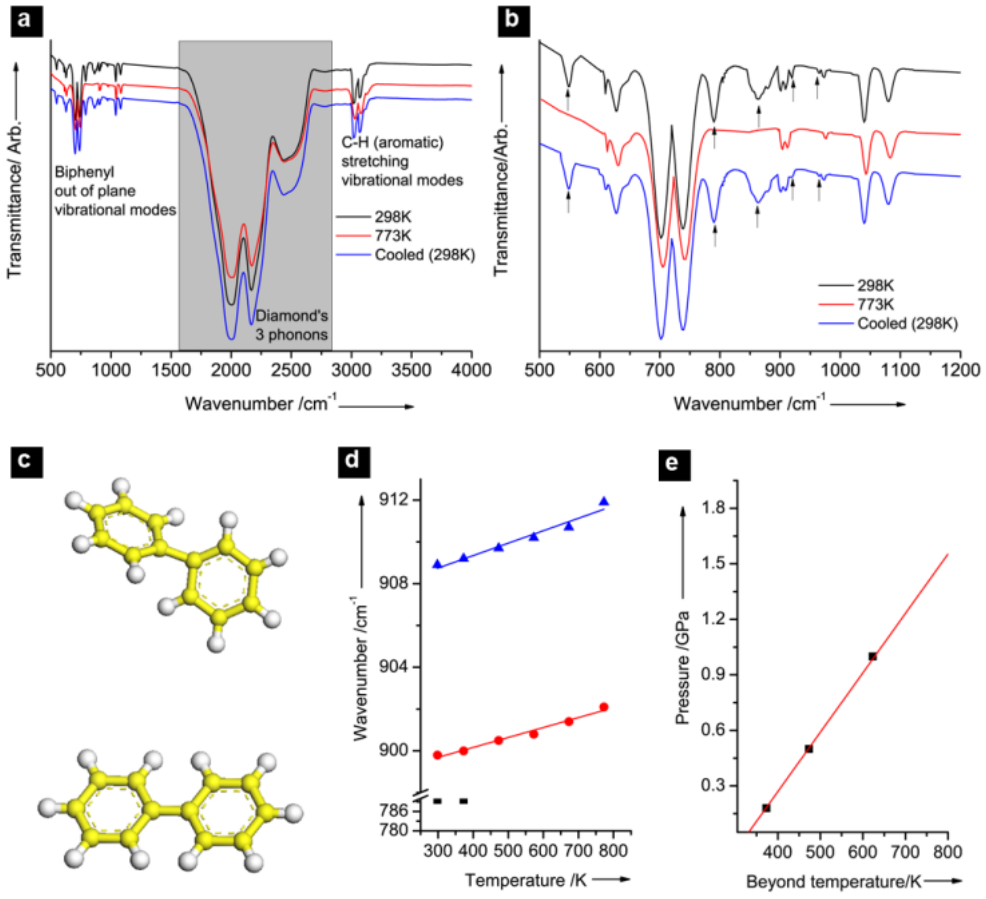

Figure 6.2 a) FTIR wide spectra of biphenyl in GNB on diamond before and after phase transition, at 298 K, 773 K and cooled to 298 K. b) FTIR spectra showing out-of-plane modes of biphenyl in GNB on diamond before and after phase transition, at 298 K, 773 K and cooled back to 298 K. c) Molecular structure of biphenyl, twisted (top) and flat (bottom). d) Frequency shifts of three biphenyl vibrational modes, as a function of temperature. e) Pressure as a function of temperature.

Since the critical pressure at which polyphenyls flatten increases with increasing number of phenyl rings, p-terphenyl and quarterphenyl were also employed to extend the pressure range that can be determined. The flattening of p-terphenyl and quarterphenyl was reported to be observed at *ca.* 0.5 GPa

and 1.0 GPa, respectively[8,18]. The disappearance of the specific IR peaks was observed at 473 K and 623 K for p-terphenyl and quarterphenyl, respectively, this allows us to derive the pressure-temperature relationship curve as depicted in Figure 6.2e.

6.3.3 Polymerization of fullerene in graphene bubbles

To evaluate whether the pressure inside the bubble is effective for driving symmetry-forbidden reaction, we consider the [2+2] cycloaddition of C_{60} molecules. The oligomerization of C_{60} is a model reation for testing the pressure inside the GNB since the progressive stages of coupling from dimerization to trimerzation *etc*, exhibit well defined Pressure-Temperature (P-T) phase boundaries. The [2+2] cycloaddition of C_{60} is not favourable due to the mismatch of molecular orbital. However, this reaction can be activated photochemically via triplet excited states[19-22]. Polymerization of C_{60} has also been obtained by irradiation with electrons or ions[23], plasma treatment[23], alkali metal doping[24,25], direct chemical synthesis[26] and even mechanical milling[27]. Finally, pressure can be used to compress C_{60} molecules and to drive intermolecular coupling.

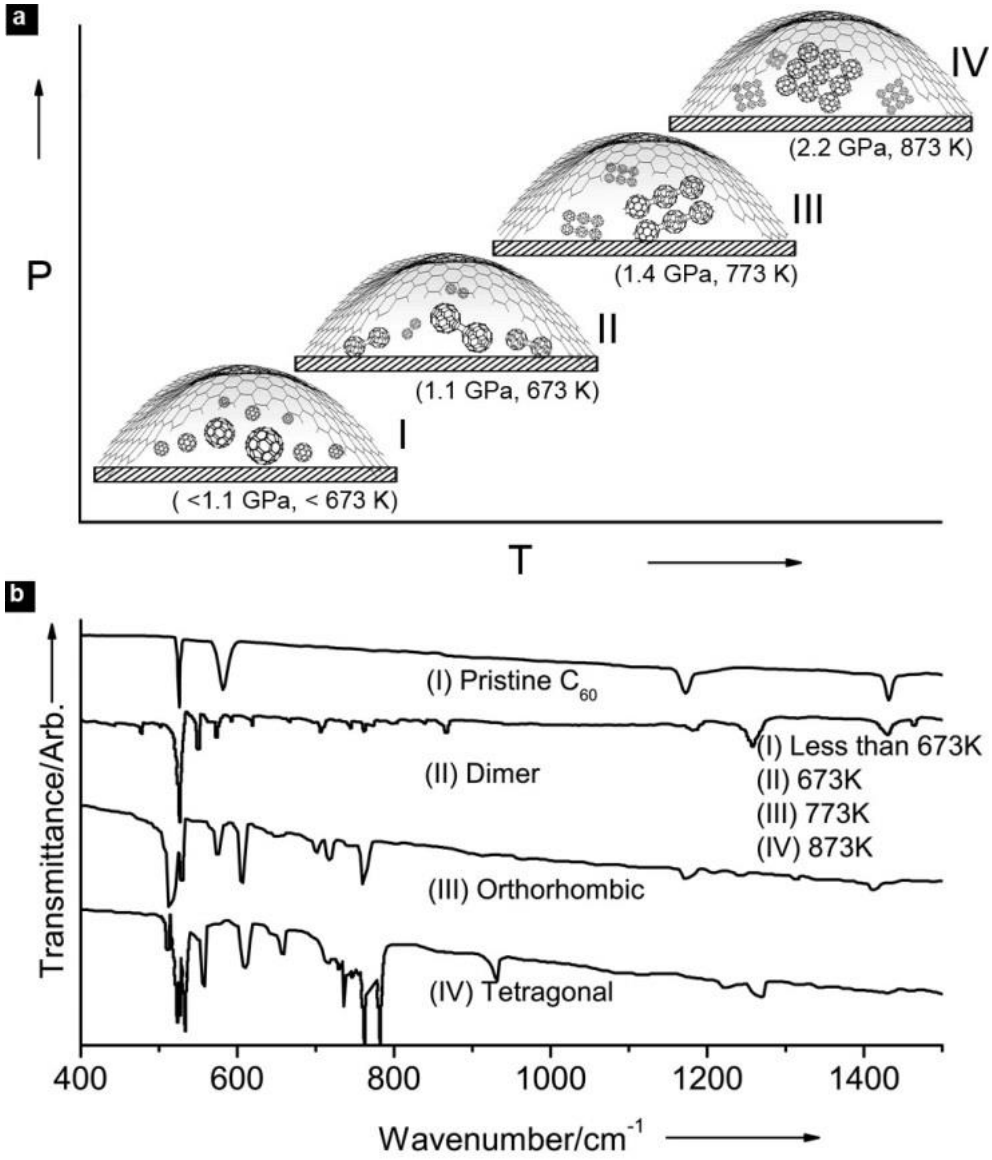

Figure 6.3 Schematic structures of a) (I)Pristine C_{60}., (II)dimer formed from [2+2] cycloaddition, (III)orthorhombic structure where each molecule is bonded to the two nearest neighbour along a <110> fcc direction forming parallel chains and (IV) tetragonal structure where each molecule is bonded to four nearest neighbours in a <100> fcc plane. (left to right) b) IR spectra of pristine, dimer, orthorhombic and tetragonal phases of C_{60} (top to bottom).

The molecular nature of C_{60} molecule is apparent in its exceptionally simple vibrational spectrum, which exhibits four sharp IR modes, as expected for an isolated cage of icosahedral symmetry (see Fig. 6.3b (i)) [28,29]. These vibrational properties change dramatically when the weak van der Waals

forces among the fullerene molecules are replaced by covalent bonds[20,30]. Formation of inter-cage covalent bonds vigorously reduces the molecular symmetry and gives rise to pronounced changes of the vibrational spectra[31,32]. Such a lowering of symmetry activate the silent I_h modes of C_{60} to result in appropriate splitting of the degenerate T_{1u} and H_g vibrational modes, giving rise to new bands at different stages of the polymerisation[30,33-35]. The IR spectra in Fig. 6.3b illustrates the phase transformation of C_{60} in GNB under various temperatures (pressures). According to group theoretical analysis, more than 300 modes in the $(C_{60})_2$ dimer (D) molecule and 150 vibrations of the distorted C_{60} cage in the orthorhombic (O) and tetragonal (T) polymers are predicted to be distributed between the IR and Raman spectra[31]. Yet, the typical IR and Raman spectra observed experimentally consist of only tens of well distinguished bands. This discrepancy is due to the low intensity of the certain vibration modes. Features characteristic of pressure-polymerized forms of C_{60} are observed in the 600-700 cm^{-1} spectra region. The strong blue shifted bands at 615 (D), 605 (O) and 609 (T), which originate from the H_u (2) parent mode is a clear indication of the modification of the fullerene cage. Several fingerprint bands due to individual distinct oligomer are observed. In the spectra of the dimer, the moderate band at 770 cm^{-1} and the sharp line at 762 cm^{-1}correspond to the activation of H_g (4) and F_{2g}(2) icosahedral even modes, respectively. The presence of a unique 1,464 cm^{-1} band in the spectrum of the dimer (Fig. 6.3b (ii)), assignable to the A_g(2) derivative is a clear indication of the loss of inversion center by the C_{60} moiety. In addition, the peak at 1,455cm^{-1} with medium can also be used to identify $(C_{60})_2$ dimer from other polymeric forms[31]. The F_{2u}(2) mode in the polymeric species splits into

doublets (711/716 cm^{-1} in the O and 709/719 cm^{-1} in T phases) with different relative intensities. Besides the $G_u(2)$ mode triplet splitting (730/741/747 cm^{-1}) in the spectra of tetragonal polymers, we also observed strong narrow lines at 759 (O) and 762 (T) which originate from the $G_u(3)$ mode of C_{60}. A sharp band at 932 cm-1 is observed in the fingerprint region of the tetragonal phase when the sample is heated to 873 K, it can be inferred that a sharp phase transition has occurred at this temperature. It is noteworthy to mention that the oligomerization reaction of C_{60} is irreversible, the distinctive spectroscopic signatures of the oliogomerized phases remained even after the samples were cooled to room temperature.

6.4 Conclusion

In summary, we have shown that GNB can be used as a bench-top anvil for the investigation of high pressure chemistry. The advantage of using the graphene-diamond anvil cell is that pressure is exerted isotropically on the sample, whereas in conventional cells, the axial force of the squeezer tends to deform the samples of interest. The anisotropy of some crystals and carbon phases obtained from C_{60} fullerite under high pressure has been attributed to the additional pressure component that occurs in the quasi-hydrostatic experimental conditions in the conventional anvil cell[36,37]. Due to the transparency of graphene, it should be possible to study photochemical reactions in the trapped fluids by directing lasers on the GNB. Finally, such graphene bubbles can be used as adaptive focus lenses by combining the

approaches of the fluidic lens and liquid-crystal lens. The change in curvature of the bubbles induced by expanding liquid can result in focal length changes due to changes in refractive indexes, which can be deployed in optical bistability-based control schemes.

6.5 References

1 Jenner, G. Correlation between pressure and steric interactions in organic reactions. *Tetrahedron* **61**, 3621-3635 (2005).

2 Atkins, P., De Paula, J. & Walters, V. *Physical Chemistry, Volume 1: Thermodynamics and Kinetics*. (Macmillan Higher Education, 2006).

3 Matsumoto, K., Hamana, H. & Iida, H. Compendium of cycloaddition reactions under high pressure. *Helvetica Chimica Acta* **88**, 2033-2234 (2005).

4 Aben, René W. M., Braverman, S. & Scheeren, Hans W. High Pressure-Promoted [2+2] Cycloaddition Reactions of 4-Methylphenyl 1,2-Propadienyl Sulfone with Enol Ethers. *European Journal of Organic Chemistry* **2003**, 894-897 (2003).

5 Aben, René W. M., de Gelder, R. & Scheeren, Hans W. High-Pressure Promoted Cycloadditions of Enol Ethers and 3-Aryl-2-cyano-2-propenoates. *European Journal of Organic Chemistry* **2002**, 3126-3132 (2002).

6 Lee, C., Wei, X., Kysar, J. W. & Hone, J. Measurement of the Elastic Properties and Intrinsic Strength of Monolayer Graphene. *Science* **321**, 385-388 (2008).

7 Forman, R. A., Piermarini, G. J., Dean Barnett, J. & Block, S. Pressure measurement made by the utilization of ruby sharp-line luminescence. *Science* **176**, 284-285 (1972).

8 Zhuravlev, K. K. & McCluskey, M. D. Flattening of organic molecules under pressure. *Journal of Chemical Physics* **114**, 5465-5467 (2001).

9 Li, X. *et al.* Large-area synthesis of high-quality and uniform graphene films on copper foils. *Science* **324**, 1312-1314 (2009).

10 Ruckenstein, E. & Churaev, N. A possible hydrodynamic origin of the forces of hydrophobic attraction. *Journal of Colloid and Interface Science* **147**, 535-538 (1991).

11 Pomeranz, Y. & Meloan, C. E. *Food Analysis: Theory and Practice*. (Springer, 2000).

12 Charles, S. J. *et al.* Characterization of nitrogen doped chemical vapor deposited single crystal diamond before and after high pressure, high temperature annealing. *Physica Status Solidi (A) Applied Research* **201**, 2473-2485 (2004).

13 Cremer, D. Pros and cons of σ -aromaticity. *Tetrahedron* **44**, 7427-7454 (1988).

14 Fischer-Hjalmars, I. Conjugation and non-bonded interaction. *Tetrahedron* **19**, 1805-1815 (1963).

15 Zhuravlev, K. K. & McCluskey, M. D. Infrared spectroscopy of biphenyl under hydrostatic pressure. *Journal of Chemical Physics* **117**, 3748-3752 (2002).

16 Machavariani, G. Y., Pasternak, M. P., Hearne, G. R. & Rozenberg, G. K. A multipurpose miniature piston-cylinder diamond-anvil cell for pressures beyond 100 GPa. *Review of Scientific Instruments* **69**, 1423-1425 (1998).

17 Lemée-Cailleau, M. H., Girard, A., Cailleau, H. & Délugeard, Y. Raman-scattering study of the n=4 incommensurate phase of biphenyl under hydrostatic pressure. *Physical Review B* **45**, 12682-12690 (1992).

18 Baer, B. J. & Chronister, E. L. Pressure induced phase transitions in pentacene doped para-terphenyl probed by changes in the impurity absorption spectrum. *The Journal of Chemical Physics* **99**, 3137-3138 (1993).

19 Aoki, K. *et al.* High pressure FT-IR study of solid carbon molecule (C60). *The Journal of Physical Chemistry* **95**, 9037-9039 (1991).

20 Rao, A. M. *et al.* Photoinduced polymerization of solid C60 films. *Science* **259**, 955-957 (1993).

21 Rao, A. M. *et al.* Photoinduced polymerization of solid C70 films. *Chemical Physics Letters* **224**, 106-112 (1994).

22 Zhou, P., Dong, Z.-H., Rao, A. M. & Eklund, P. C. Reaction mechanism for the photopolymerization of solid fullerene C_{60}. *Chemical Physics Letters* **211**, 337-340 (1993).

23 Sundqvist, B. in *Fullerene-Based Materials* Vol. 109 *Structure and Bonding* (ed Kosmas Prassides) Ch. 4, 85-126 (Springer Berlin Heidelberg, 2004).

24 Stephens, P. W. *et al.* Polymeric fullerene chains in RbC_{60} and KC_{60}. *Nature* **370**, 636-639 (1994).

25 Renker, B., Schober, H. & Braden, M. Alignment of polymer chains in RbC_{60} by uniaxial pressure. *Solid State Communications* **109**, 423-426 (1999).

26 Wang, G. W., Komatsu, K., Murata, Y. & Shiro, M. Synthesis and X-ray structure of dumb-bell-shaped C_{120}. *Nature* **387**, 583-586 (1997).

27 Liu, Z. G., Ohi, H., Tsuchiya, K., Umemoto, M. & Masuyama, K. Structural evolution of fullerene during mechanical milling. *Journal of Materials Science and Technology* **15**, 405-409 (1999).

28 Krätschmer, W., Fostiropoulos, K. & Huffman, D. R. The infrared and ultraviolet absorption spectra of laboratory-produced carbon dust: evidence for the presence of the C_{60} molecule. *Chemical Physics Letters* **170**, 167-170 (1990).

29 Dresselhaus, M. S., Dresselhaus, G. & Eklund, P. C. *Science of fullerenes and carbon nanotubes [electronic resource]*. (Academic Press, 1996).

30 Iwasa, Y. *et al.* New phases of C_{60} synthesized at high pressure. *Science* **264**, 1570-1572 (1994).

31 Davydov, V. A. *et al.* Spectroscopic study of pressure-polymerized phases of C_{60}. *Physical Review B - Condensed Matter and Materials Physics* **61**, 11936-11945 (2000).

32 Martin, M. C., Koller, D., Du, X., Stephens, P. W. & Mihaly, L. Insulating and conducting phases of RbC_{60}. *Physical Review B* **49**, 10818-10821 (1994).

33 Xu, C. H. & Scuseria, G. E. Theoretical Predictions for a Two-Dimensional Rhombohedral Phase of Solid C_{60}. *Physical Review Letters* **74**, 274-277 (1995).

34 Komatsu, K. *et al.* Mechanochemical synthesis and characterization of the fullerene dimer C_{120}. *Journal of Organic Chemistry* **63**, 9358-9366 (1998).

35 Lebedkin, S. *et al.* Raman scattering study of C120, a C60 dimer. *Chemical Physics Letters* **285**, 210-215 (1998).

36 Núñez-Regueiro, M., Marques, L. & Hodeau, J. L. in *The Physics of Fullerene-Based and Fullerene-Related Materials* Vol. 23 *Physics and Chemistry of Materials with Low-Dimensional Structures* (ed Wanda Andreoni) Ch. 11, 409-442 (Springer Netherlands, 2000).

37 Glazov, A. G. *et al.* Anisotropy of the elastic properties and the microhardness of disordered superhard carbon obtained from C_{60} fullerite under high pressures. *JETP Letters* **73**, 552-556 (2001).

Chapter 7

Diamond and graphene as biocompatible scaffolds for tissue engineering

Abstract:

The culture of bone marrow derived mesenchymal stem cells (MSCs), as well as the control of its differentiation toward different tissue lineage, is a very important part of tissue engineering, where cells are combined with artificial scaffold to regenerate tissues. MSCs can be induced to differentiate into desired cell types applicable in tissue engineering by the the manipulation of its supporting scaffold. By using nanocrystalline diamond (NCD) and graphene (G) we demonstrate electrical and chemical effects on MSCs. Electrically charged surfaces have been reported to enhance growth and differentiation of cells. Here, boron was introduced to NCD films to impart electrical conductivity and we studied the effects on the growth and differentiation of MSCs. While the healthy proliferation of stem cells on various carbon platforms has been demonstrated, the chemical role of graphene (G) and graphene oxide (GO), if any, in guiding uncommitted stem cells toward differentiated cells is not known. Herein, we report that the strong noncovalent binding abilities of G allow it to act as a preconcentration platform for osteogenic inducers, which accelerate MSCs growing on it toward the osteogenic lineage. The molecular origin of accelerated differentiation is investigated by studying the binding abilities of G and GO

toward different growth agents. Interestingly, differentiation to adipocytes is greatly suppressed on G because insulin, which is a key regulator for the synthesis of fatty acids, is denatured upon π-π adsorption on G; in contrast, GO does not interfere with adipogenesis due to electrostatic binding with insulin. The different binding interactions and their subsequent influence on stem cell growth and differentiation are ascribed to different degrees of π- π stacking and electrostatic and hydrogen bonding mediated by G and GO.

7.1 Introduction

Mesenchymal stem cells (MSCs) isolated from adult bone marrow are multipotent progenitor cells noted for their potential to differentiate into cell lineages such as adipocytes, osteoblasts, and chondrocytes[1]. By manipulating material mechanics[2], substrate topography[3], and applied growth factor inducers[4], MSCs can be induced to differentiate into desired cell types applicable in tissue engineering and regenerative medicine. Many biochemists and molecular biologists employ electrical stimulation and chemical factors to induce differentiate *in vitro*, but guided differentiation of stem cells using these strategies is not efficient and often require weeks to months of cell culture for maturation into distinct lineages[5]. This has limited the widespread use of stem cell therapy. Therefore, there is a need to develop efficient methods for enhancing MSC differentiation.

There is a drive to search for biocompatible and mechanically stable scaffolds for *in vivo* implant technology for delivering stem cells[6,7]. Certain

nanomaterials were found to be able to enhance stem cell proliferation and lineage specification, although the chemical origins of these can be complex[8,9]. Aqueous suspensions of carbon nanotubes[10], and gold nanoparticles[11] have been demonstrated to enhance osteogenesis. A stress mechanism was suggested to be operational, brought about by the interaction of these nanomaterials with the cell membrane as well as binding with proteins in the cytoplasm, which activated the p38 mitogen-activated protein kinase (MAPK) signalling pathway responsible for regulating the expression of genes inducing osteogenic transcription[11]. Glass substrates coated with bionanoparticles such as turnip yellow mosaic (TYMV) and tobacco mosaic virus (TMV) have also been shown to stimulate MSC osteogenic differentiation and bone matrix mineralization, and factors such as the nanoscale topography, serum protein adsorption by virsus, or interaction with certain cellular receptors have been proposed.

Among all carbon materials studied, only nanocrystalline diamond (NCD) has shown excellent biocompatibility and no cytotoxicity in both *in vitro* and *in vivo* studies and have been proposed as a promising material for tissue engineering and regenerative medicine[12]. Unlike single crystalline diamond, NCD can be prepared on diverse substrates with tunable roughness[13-15]. Moreover due to the general chemical stability of diamond, it can be used as the starting point for covalent attachment of functionalities such as DNA[16,17], proteins[18,19] or multi-layered molecules[20,21] for the tailoring of bio-interfaces. In addition, NCD films could be a suitable coating for medical implants, for coating the heads and cups of artificial joint replacements, e.g. metallic and polymeric prostheses of hip or temporomandibular joints[22,23].

This beneficial action of NCD can be anticipated not only due to its excellent mechanical and chemical resistance but also due to their surface nanoroughness (i.e. irregularities less than 100 nm). The surface nanotopography has been reported to stimulate adhesion, growth and maturation of osteoblasts, as well as differentiation of bone progenitor cells towards the osteogenic lineage[24,25]. To date, most of the reported work focused on using NCD as electrically passive substrates. Dopants, such as boron can be introduced into NCD bestowing electrical conductivity, making it an excellent electrode for collection of electrical signals[26]. Even without active stimulation of the cells with an electric current and an electromagnetic field, it has been reported that vascular endothelial cells, vascular smooth muscle cells and bone marrow stromal cells grew better on positively charged surfaces than on electro-neutral polymeric surfaces[27-29]. A negative charge has also been reported to have increased in the production of collagen II in rabbit chondrocytes[30]. It is well known that p-type conductivity can be imparted to NCD by boron doping[31]. Yet, little is known about the direct influence of boron-doped NCD on adhesion, viability and differentiation of MSCs. In the first part of this chapter, we present the impact of boron doping of NCD film on the effect of cell growth and differentiation and assess intrinsic and boron-doped NCD films as supporting platform for the cultivation of MSCs.

Unlike diamond surface that can be used for covalent attachment of different functionalities, atomically thin graphene (G) and its oxidized derivative graphene oxides (GO) sheets are biocompatible platforms that offer open surfaces for non-covalent interactions with biomolecules. G is characterized by a purely carbon, aromatic network, whereas GO has epoxide,

carboxyl and hydroxyl groups present on the basal planes and edges. It is envisaged that G and GO have the potential to mediate stem cell lineage specification for tissue regeneration through their enhanced interactions with proteins through non- covalent, electrostatic and hydrogen bonding. The ability of chemical vapor deposited grown G to promote the adhesion and proliferation of MSCs and osteoblasts has been demonstrated[32]. In the presence of osteogenic chemical inducers, MSCs cultured on G substrates exhibited early maturation and mineralization[33]. Although the ability of G in modulating osteogenic differentiation is evident, the origin of how it can accelerate stem cell renewal and differentiation is not known. To investigate if this is correlated to the chemical properties of G, in the second part of this chapter, we investigate the effects of G and GO substrates on the adipogenic and osteogenic differentiation of MSCs. Of central interest in this study is whether G and GO, through molecular binding interactions, can act as preconcentrating platforms for soluble factors required for stem cell growth and differentiation. If so, G and GO could become ideal substrates for the effective specification of stem cell fate in the presence of multiple chemical stimuli.

7.2 Materials and methods

7.2.1 Surface preparation of diamond

NCD substrates were fabricated by the PECVD in the form of a thin layer of boron-doped diamond film on quartz (160-nm-thick, boron concentration 3×10^{-21} cm^{-3}) according to published procedures[34,35]. The undoped NCD films were grown to the same thickness in another reaction chamber to ensure that there is no inclusion of dopants from contamination. Acid cleaning and oxygen plasma cleaning of diamond were used for all diamond samples. Metallic impurities were first dissolved in hot aqua regia (HNO_3/HCl 1:3), followed by removing organic impurities from the diamond samples by hot "piranha" solution (H_2O_2/H_2SO_4 1:3) at 90 ^oC for 1 h. O-termination of diamond was obtained by oxygen plasma treatment using a radio frequency plasma etching system (Diener electronic-Femto). The oxygen gas flow was maintained at 5 sccm at 30 W for 1 min.

7.2.2 G and GO film preparation

The transfer technique employed in this study to transfer G or GO films to poly-dimethylsiloxane (PDMS) (Dow Corning) is similar to previously reported methods[36]. GO film was prepared through the use of a Langmuir-Blodgett (LB) trough (Nima Technologies). GO was dispersed in water-methanol (1:5) solution at a concentration of 1 mg/mL. The surface of

the water-filled LB trough was cleaned several times by aspiration. Then 100 μL of the GO solution was deposited on the water-filled LB trough. After 30 min of equilibration, the film was compressed to a surface pressure value of 20 mN/m. The GO film was formed by dip-coating the PDMS substrate several times.

7.2.3 Characterization

Raman spectra of G and GO film were obtained with a WITEC CRM200 Raman spectrometer at room temperature, with an excitation laser source of 532 nm. The laser power was kept below 0.1 mW to prevent heating of the sample. The hydrophicility of the samples was investigated using contact angle measurements (VCA Optima, AST Products Inc.). XPS was performed using an unmonochromated Al Kα X-ray source at 1486.6 eV (Thermo VG Scientific, UK) with a Phobios 100 electron analyzer (SPECS GmbH, Germany) equipped with 5 channeltrons. The pass energy of the analyzer was fixed at 50 eV for wide scan and 20 eV for narrow scan, and the takeoff angle was normal to the sample.

7.2.4 Spectrophotometry for determination of loading capacities

Dexamethasone, β-glycerolphosphate, ascorbic acid, and insulin (obtained from Sigma-Aldrich and used without further purification) with

concentrations ranging from 10^{-4} to 10^{-1} M were prepared in phosphate buffer. Fetal bovine serum (Gibco) was reconstituted in DMEM at 1, 2, 5 and 10% (v/v) for spectrophotometric measurement. PDMS, G and GO (1mg/ml) in phosphaste-buffered saline (PBS) were sonicated for 1 h prior to usage, to ensure the formation of a homogeneous dispersion. The chemical agents (0.5 mL) were mixed with PDMS, G or GO (0.5 mL) and vortexed in a shaker for equilibration. After which, the mixture was centrifudged (14,000 rpm, 10 min), the supernatant was collected, and spectrophotometric measurements were conducted on day 1 and 3. The adsorption isotherm of the respective chemical agent was obtained using UV-vis spectroscopy. The amount of chemical agent adsorbed was determined from the change in protein adsorption before and after the addition of PDMS, G and GO using a UV-vis spectrophotometer (NanoDrop 2000, Thermo Scientific).

7.2.5 Circular dichroism spectroscopy

Each circular dichroism (CD) spectrum and its corresponding high tension voltage curve were recorded on a Jasco J-810 spectropolarimeter using a quartz cell with an optical path length of 1 mm. The scanning speed was set at 50 nm/min, and the wavelength range was set at 190-260 nm. All samples were prepared in PBS adjusted to ~pH 7.4. By considering the specific areas of G and GO to be 2630 m^2/g [ref 37,38], 0.3125 mg/mL of insulin and 0.025 mg/mL of G and GO were used to simulate the conditions of the cell culture

environment. All spectra collected were obtained from an average of three consecutive scans.

7.2.6 Cell culture

Human bone marrow derive MSCs were obtained from commercial sources (Lonza). Cells were cultured in a humidity-controlled environment under 5% CO_2 and fed every 3 days with Dulbecco's modified Eagle's medium (Gibco), supplemented with 10% fetal bovine serum (Invitrogen) and 1% penicillin/streptomycin (Invitrogen). Cells were received at passage 1, expanded at ~5,000 cells/cm^2, and subcultured at 70-80% confluence. Passage 4 cells were used in the experiments. MSCs were applied at 1,000 cells per cm^2 for time course study of cell morphology. Cells were fixed in 4% paraformaldehyde (Sigma-Aldrich), stained with rhodamin phalloidin (Invitrogen), costained with 4',6-diamidino-2-phenylindole (DAPI) (Sigma-Aldrich), and imaged under an epi-fluorescence microscope (Olympus IX81, Olympus Inc.) at day 1,4,7,10.

7.2.7 Osteogenic differentiation on NCD

MSCs were cultured for 18 days in cell growth media with no foreign chemical inducers added. The cell growth media composed of DMEM with 10% FBS and 1% penicillin/streptomycin. The cells were cultured in a 5% CO_2

incubator at 37 ^{o}C. After 18 days of cell culture, the cells were fixed in 4% paraformaldehyde. The samples were then incubated at room temperature for 1 h in 1% BSA/1 X PBS followed by the addition of the antiosteopontin (OPN) antibody (1:100 AKm2A1, Santa Cruz Biotechnology), and incubated for overnight at 4 ^{o}C. Cells were then washed 3 times for 5 min each with 1 X buffer. Goast mouse IgG-FITC (1:100, Santa Cruz Biotechnology) and TRITC-conjugated phalloidin (1:40, Invitrogen) in 1 X PBS was added for double staining and the cells were again incubated for 1 h at room temperature. Following, the cells were washed 3 times with 1 X buffer and were costained with DAPI.

7.2.8 Osteogenic differentiation on G and GO

MSCs were seeded at 2,500 cells/cm^2 and cultured for two weeks in DMEM with 10% FBS, 10 mM β-glycerophosphate, 10^{-8} M dexamethasone, and 0.2 mM ascorbate and with the medium changed every 3 days. Non-induced control MSCs were fed only basal medium with 10% FBS and 1% penicillin/streptomycin on the same schedule. After 12 days of induction, cells were stained with Alizarin Red (Sigma-Aldrich) and extracted with 20% methanol and 10% acetic acid for spectrophotometric quantification at 450 nm using a Nanodrop UV-vis spectrophotometer.

7.2.9 Adipogenic differentiation on G and GO

MSCs were plated at 2 X 10^4 cells/ cm^2 and induced to differentiate for 14 days.in DMEM with 10% FBS, 10^{-6} M dexamethasone, 5 μg/mL insulin (Sigma-Aldrich) and 0.6 X 10^{-4} M indomethacin (Sigma-Aldrich). Non-induced control MSCs were fed only basal medium with 10% FBS and 1% penicillin/streptomycin on the same schedule. After 14 days of incubation, cells were rinsed with PBS, fixed in 4% methanol-free formaldehyde (Sigma-Aldrich), then stained with Oil Red O (Sigma-Aldrich), and costained with DAPI for 30 min. The stained cells were then observed under an epi-fluorescence microscope (Olympus IX81, Olympus Inc.). Quantification of adipogenic differentiation by MetaMorph 6.3v3 was based on measuring the total number of Oil Red O red pixels, then normalizaing to nuclei count based on detected DAPI fluorescence. The end data correspond to the total area of lipid droplets present per cell (μm^2). The area meausrements were imported into Microsoft Excel, and the mean ±SD of the areas was calculated.

7.2.10 AFM imaging and indentation

All data were acquired using NanoWizard II AFM (JPK Instruments) coupled with an inverted microscopy (Olympus). NCDs were imaged after the surface preparation process and G, GO and PDMS samples were acquired in PBS at room temperature. For images captured in contact mode, HYDRA2R-100NG probes (Applied Nanostructures) were used. HSC 20 probes with a

defined hemispherical tip shape of ~20 nm in radius (~0.4 N/m) (Nanoscience Instruments) were used for indentation experiments. Indentation was carried out at the clean spots immediately after scanning the same area using the same probe. The ramp size in this study was 1 μm, and the loading speed was 1μm/s. An indentation force of 3 to 30 nN was applied during the tests in order to ensure that the indentation depth is less than 20 nm. The Young's modulus was subsequently determined using Hertz's contact mode using JPK Data Processing software (JPK Instruments).

7.2.11 Statistical analysis

The statistical differences were analysed (n=4) by a paired Student's t test; p values less than 0.05 were considered to indicate statistical differences (95% confidence interval).

7.3 Results and discussion

7.3.1 NCD for MSCs growth and differentiation

7.3.1.1 Surface characterization of NCD

The surface morphology of the NCD grown on quartz substrates, as evaluated by the AFM, is illustrated in Fig 7.1. The morphology of the undoped NCD film (i.e. 0 ppm boron doping) and doped NCD (160 nm thick, boron concentration 3×10^{21} cm^{-3}) is similar, in spite of slight variations in crystal sizes, shapes and surface roughness. The structural features of the NCDs are on the scale of tens of nanometers. The substrate elasticity was also determined by AFM and our measurements showed that the Young's modulus values of both undoped and doped NCD are 500 and 480 GPa respectively. The apparent similar Young's modulus values of these substrates imply that hardness does not play an important role in undermining the differences observed for differentiation of the MSCs. Contact angle measurement revealed the highly hydrophilic nature of these NCDs as they are oxidized by strong acids and exposed to O-plasma prior to the seeding of cells (see Table 7.1).

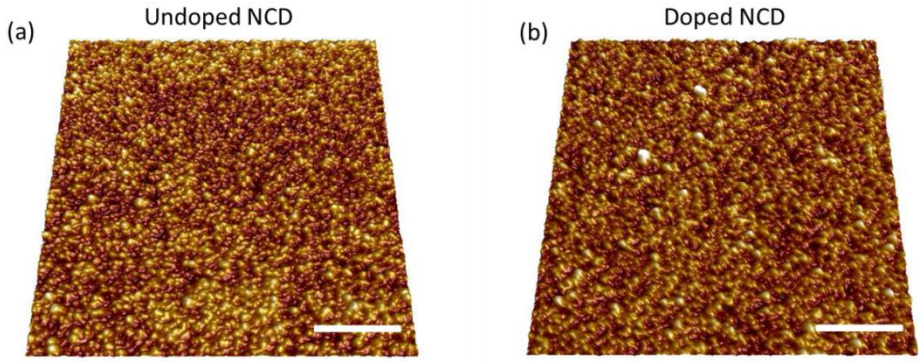

Figure 7.1 Mapping of surface morphology of NCD samples with AFM (a) undoped and (b) doped. Scale bar shown correspond to 2 μm.

Table 7.1 Surface parameters of the NCD substrates.

NCD	Boron concentration (cm^{-3})	Rs (Ω sq^{-1})	Contact angle (^{o})	Young's modulus (GPa)	RMS (nm)
Undoped	0	$>10^6$	15	500	~20
Doped	3×10^{21}	310.5	12	480	~25

7.3.1.2 Effects of surface roughness on cell growth and differentiation

The enhanced growth and osteogenic differentiation of MSCs brought about by both intrinsic and doped NCDs, as compared to cells on standard polystyrene culture dishes, can be attributed to their surface nanoroughness. Since cell adhesion is mediated by extra cellular matrix (ECM) molecules, such as vitronectin, fibronectin, collegen and laminim, adsorbed to the surface of the material deposited by the cells or in biological fluids, the high

roughness of the NCD films increases the surface area that is available for the adsorption of these substances, necessary for subsequent anchoring of the cell. In addition, nanostructured substrates have been reported to have a preferential adsorption of vitronectin, which is mainly recognized by osteoblasts[24,39,40]. Moreover, the positive effect of the surface nanostructure on cell colonization was probably due to the oxygen-functionalities on the surface of NCDs, which brought about a high hydrophilicity (contact angle 12-15^{o}). Surfaces possessing these terminations were reported to promote adsorption of cell adhesion-mediating molecules in a flexible conformation which is accessible by cell adhesion receptors, can act synergistically with surface nanoroughness[27,41-44].

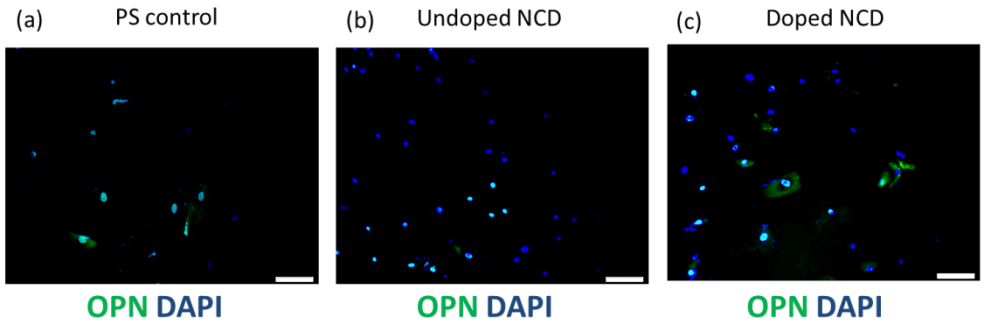

Figure 7.2 Merged immunofluorescent images of OPN (green) and DAPI (blue) after 18 days of culture on (a) polystyrene tissue culture dishes, (b)undoped NCD and (c) doped NCD.

7.3.1.3 Electroactivity on cell growth and differentiation

Another factor in affecting cell adhesion, growth and differentiation of MSCs is the electrical activity of the supporting substrate. In other words, the

electrical charge, potential and the electrical conductivity of the underlying platform plays an important role in affecting the cells. It has been previously reported that conductivity of the substrates has a positive effect on cell proliferation and differentiation even without additional electrical stimulation of the cells[45]. It is noteworthy to mention that a study conducted previously, cultured Schwann cells on electrically conductive melanin films, and accelerated proliferation rate was observed[46]. Similarly, in another study, composite nanofibers made of electrically conductive polyaniline blended with poly (L-lactide-co-epsilon-caprolactone) enhanced the adhesion and proliferation of C2C12 murine skeletal muscle myoblasts, as well as their differentiation to myotubes[47,48]. Generally, it has been agreed that electrically conductive materials has a stimulatory effect on the adhesion, growth and phenotypic maturation of even non-excitable cells, such as vascular endothelial cells[48,49], fibroblasts[48,50] as well as osteoblast[51]. Differentiation of the MSCs towards the osteogenic phenotype was enhanced on NCD film in our study. It is illustrated in Fig. 7.2 that there were higher concentrations of osteocalcin in cells on these films as compared to the cells on standard polystyrene culture dishes. In addition, we arrived at a higher degree of osteocalcin staining for doped NCD films as compared to the intrinsic NCDs. It should be noted that osteocalcin is osteoblast specific. Thus, doped NCD can enhance the differentiation of MSCs to the osteogenic lineage[45]. According to the surface topography mapped out using AFM, no significant differences in its rms surface roughness was found between the undoped and doped NCDs, thus direct effect of boron on the MSCs metabolism is less likely as boron atoms are deeply bound in the NCD lattice or the grain

boundaries. Moreover, even at elevated temperatures and high vacuum, release of these boron atoms are very limited[44]. Hence, it is expected that the release of boron atoms is unlikely to occur in biological environments.

The electrical properties of boron-doped NCD in our study, manifested by the changes in electrical resistance (undoped ~ > 10 MΩ sq^{-1}, doped ~300 Ω sq^{-1}), may account for its enhanced adhesion of films and more pronounced osteogenic differentiation of these cells. Although the mechanisms of the positive effects of electroactive materials (effect which can probably can be enhanced by additional electrical stimulation) on cell proliferation and differentiation have not yet been fully elucidated and systemized, there are some generally accepted explanations. These mechanisms include enhanced adsorption of cell adhesion-mediating ECM proteins from biological environments, a more advantageous geometrical conformation of these proteins for their accessibility by cell adhesion receptors, redistribution of cell membrane growth factors and adhesion receptors or cytoskeletal proteins, movement of charged molecules in the interior and exterior of the cell, up-regulated mitochondrial activity and enhanced protein synthesis[52-55].

7.3.2 G and GO for MSC growth and differentiation

7.3.2.1 Characterization of substrates

The G films employed in this study were grown by CVD using a reported procedure[56] and GO was synthesized by Hummer's method[37,57].

PDMS was used as the reference material as well as the support for G and GO. Raman spectroscopy was used to verify the quality of CVD graphene film.

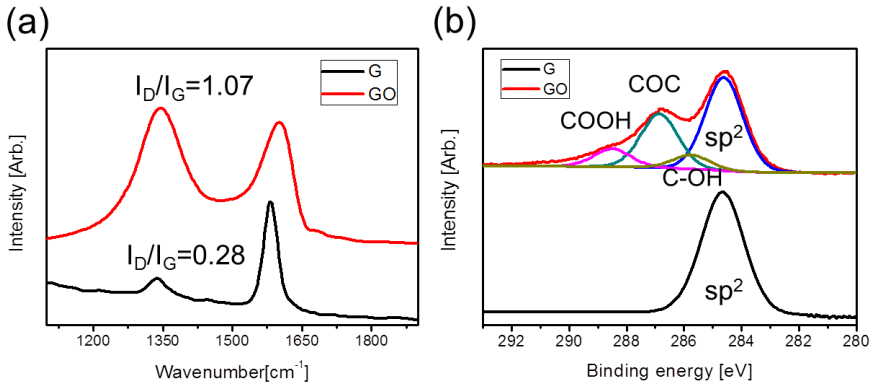

Figure 7.3 Surface characterizations of G and GO. (a) Raman spectra and (b) XPS spectra.

The negative defect-related peak at around 1,350 cm^{-1} indicates the high crystallinity of the G film. However, the oxygen functionalities on GO disrupt the extensive sp^2 conjugation, giving rise to and $I_D/.I_G$ ratio of 1.07. The chemical environments of G and GO were also analysed by X-ray photoelectron spectroscopy (XPS), illustrated in Fig. 7.3b. The symmetrical C1s peak collected from G is situated at 284.6 eV and corresponds to emission from the sp^2-hybridized carbon. On the other hand, the C1s peak collected from GO was found to be highly asymmetrical. It shows chemically up-shifted components at 1.2, 2.3 and 3.9 eV relative to the bulk peak, which can be assigned to the hydroxyl, ether, and carboxylic groups, respectively. A tapping mode atomic force microscopy (AFM) image of CVD G on PDMS revealed the typical wrinkled topography, while GO films on PDMS exhibited a more planar surface.

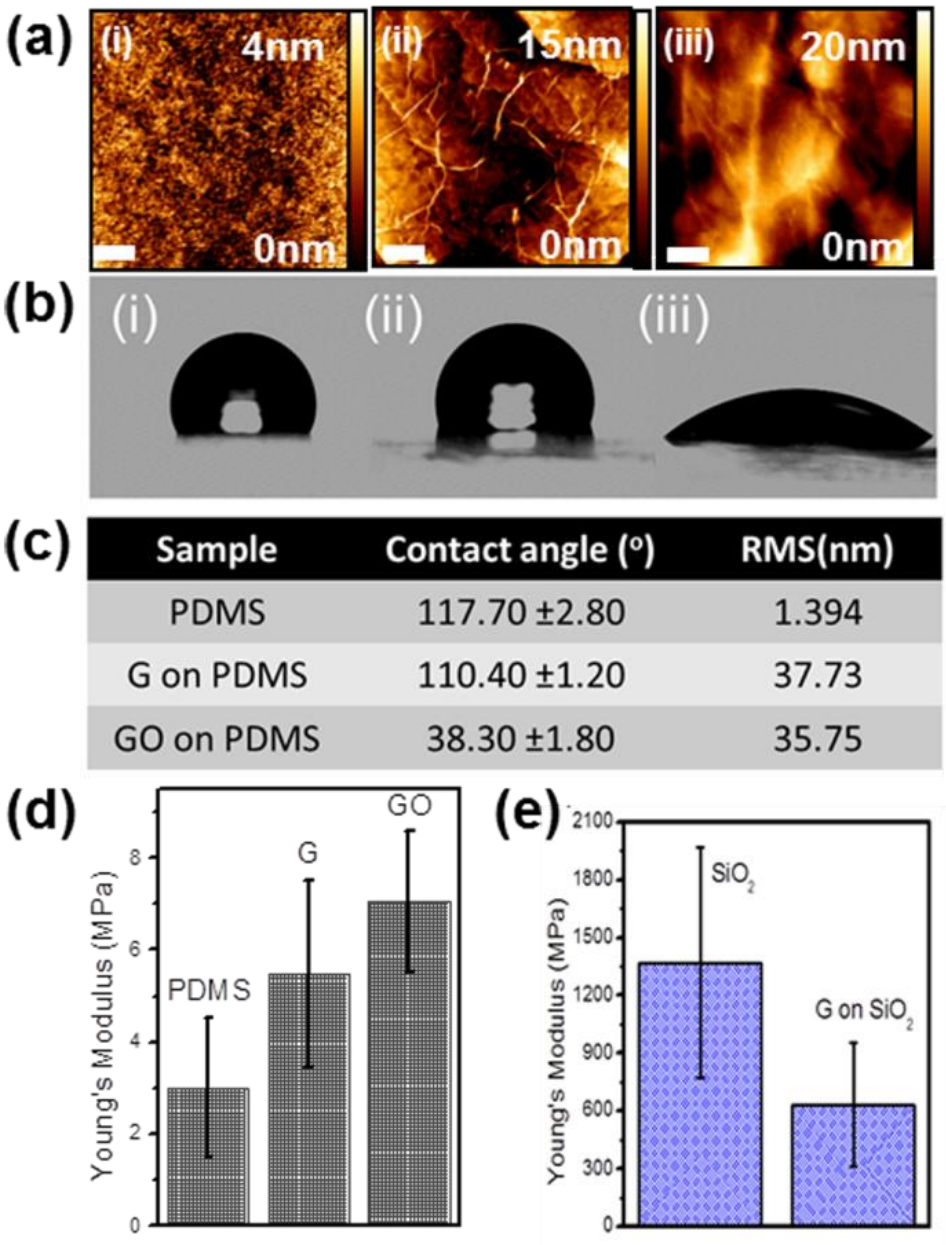

Figure 7.4 Surface characterization of substrates. (a) AFM topography images of (i) PDMS, (ii) G on PDMS, and (iii) GO on PDMS. (b) Contact angle images of (i) PDMS, (ii) G, and (iii) GO. (c) Table summarizing the contact angle and roughness (rms) of PDMS, G and GO. (d) Young's modulus bar chart of PDMS, G and GO. (e) Young's modulus bar chart of SiO_2 and G on SiO_2. Inset white scale bar indicates 1 μm length.

The substrate elasticity of G and GO films was also measured by AFM (see Fig. 7.4). Our measurement showed that the Young's modulus values of G and

GO were ~5 and 7 MPa, respectively, which were higher than that of the PDMS (~ 3 MPa). The apparently higher Young's modulus value of GO compared to G is due to the stacking of multiple layers of GO. In addition, G and GO have higher surface roughness (37.73 and 35.75 nm, respectively) than PDMS (1.39 nm). Contact angle measurement revealed the highly hydrophobic nature of G and PDMS, while, in contrast, GO is hydrophilic (see Fig 7.4 b).

7.3.2.2 Cell proliferation

In order to determine how G and GO would play a role in the cellular response and differentiation, we plated human bone marrow derived MSCs on G and GO film and used PDMS as the control substrate. Cellular morphology was evaluated by staining the F-actin fibers with phalloidin. Fluorescent images of MSCs showed that the shapes of MSCs cultured on G, GO and PDMS were distinctively different (Fig. 7.5). At day 1, MSCs on PDMS appeared rounder and lacked the filopodia extensions and cellular protrusions observed for cells cultured on G and GO. It can also be concluded from the number of blue-stained nuclei that there is a higher density of cells on G and GO than on the PDMS substrate. MSCs cultured on G films on homogenously dispersed on the surface and showed spindle-shape morphology, whereas those cultivated on GO films were larger and more widespread (Fig 7.5). However, the differences in cell morphology became less pronounced from day 7 onward.

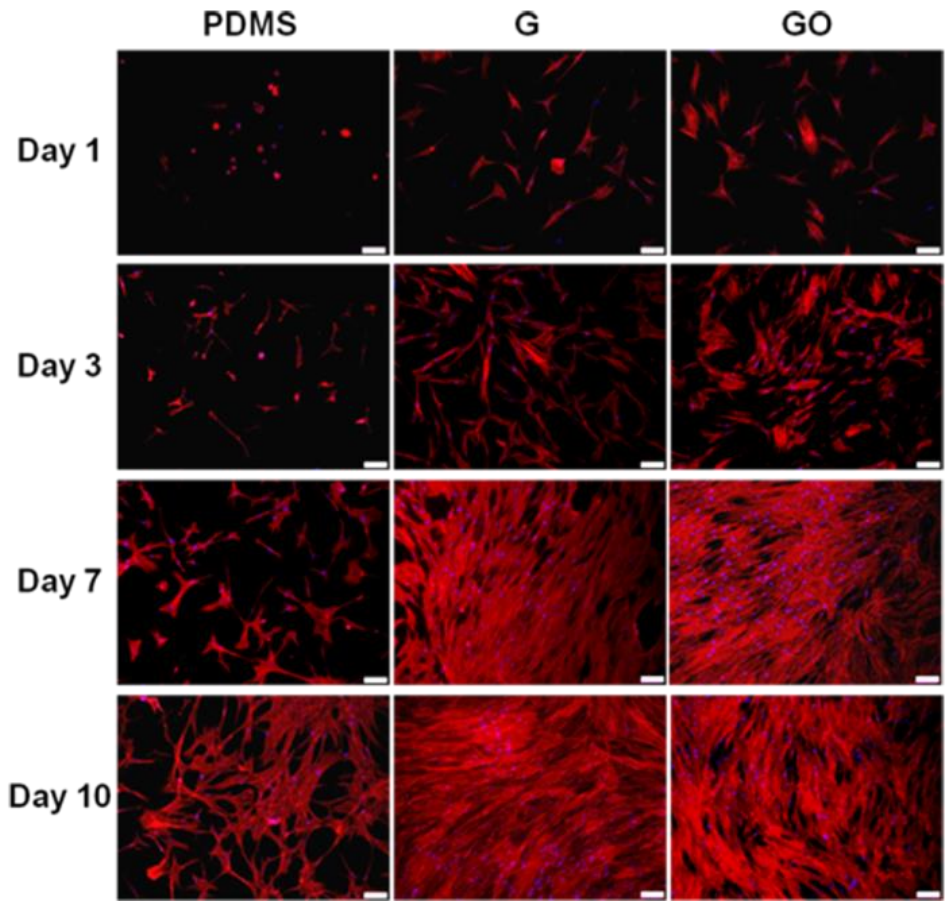

Figure 7.5 Fluorescent images of actin cytoskeleton of MSCs. MSCs cultured on PDMS, G and GO stained with rhodamine-phalloidin at dat 1,3,7 and 10. Scale bars are 100 μm.

Since serum proteins directly mediate cellular adhesion and morphology, there is a direct correlation between the adsorption capacity of the substrate for serum proteins and the subsequent cell growth. It was found that G and GO adsorbed up to 8% and 25% of the serum proteins, respectively, compared to only <1% adsorption on PDMS on day 1. It has been reported in previous studies that G and GO have remarkable loading capacities for DNA and cytochrome c *via* intermolecular interactions[58]. Serum is known to contain many ECM globular proteins and glycoproteins such as albumin and fibronectin[59]. Fibronectin is frequently used to coat polymeric substrates for

cell culture, as it plays a major role in facilitating cell adhesion. The higher adsorption capacity of G and GO (mg/g) for serum proteins resulted in a higher density of adhesion molecules available for cell attachment and growth (Fig 7.6). The MSCs seeded on PDMS were round and poorly attached as compared to G and GO (Fig 7.5). It is known that hydrophobic substrates such as PDMS exhibit poor aqueous sample loading[60] and high resistance to protein adsorption[61]. Although G and PDMS have similar hydrophobicity, as judged from contact angle measurements (Fig. 7.4), the π-electron cloud in G is capable of interacting with the inner hydrophobic core of proteins. Due to the presence of oxygenated groups, the hydrophilic GO can bind to serum proteins via electrostatic interactions.

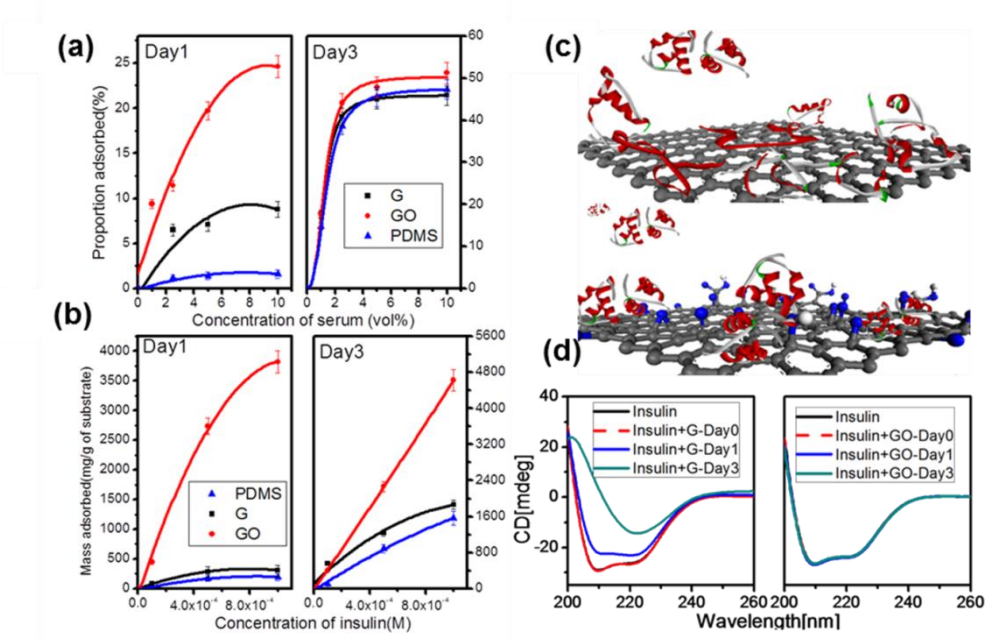

Figure 7.6 Loading capacity of (a) serum and (b) insulin on PDMS, G, GO at day 1 and 3. (c) Schematic illustration of insulin adsorption on G (top panel) and GO (bottom panel). (d) Far UV absorption CD spectra of insulin in PBS with G and GO.

7.3.2.3 Osteogenic differentiation

MSCs can be induced to differentiate to osteoblasts at low density of cells of *ca.* 3,000 cells per cm^3 in media supplemented with dexamethasone (10^{-8} M), ascorbate (0.2 mM), and β-glycerolphosphate (10 mM). After 12 days of osteogenic induction, the extent of mineralization of MSCs cultured on G, as assessed via Alizarin Red S staining was found to be greater than that cultured on GO and the PDMS control (Fig. 7.7)

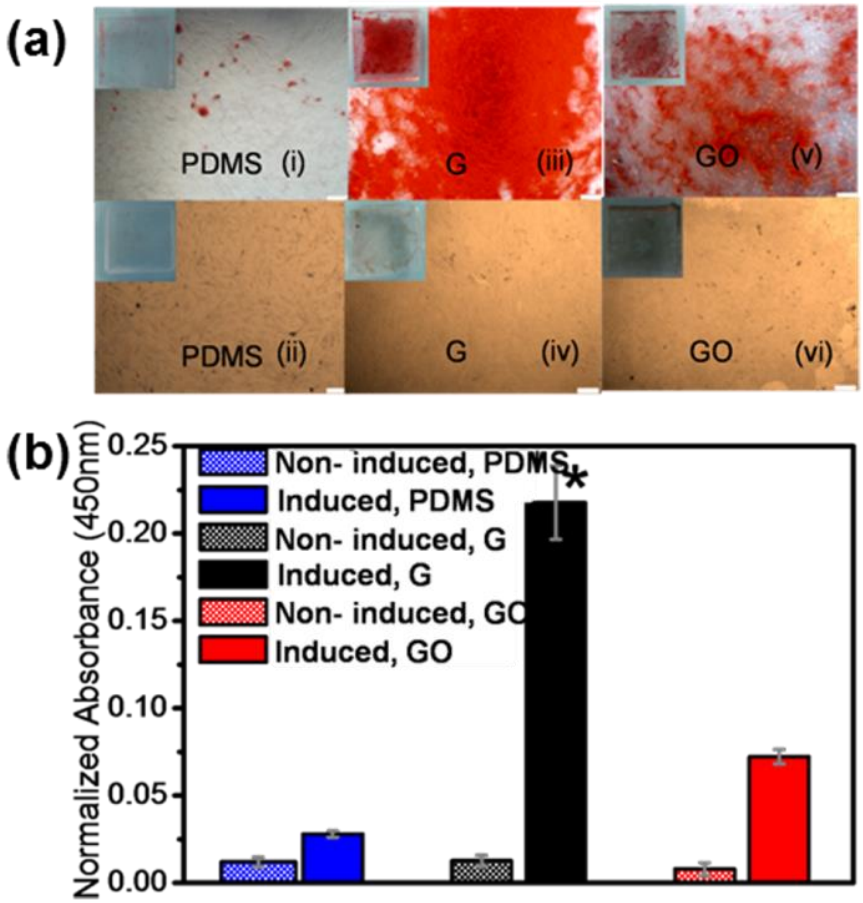

Figure 7.7 (a) Osteogenic differentiation visualized by Alizarin Red staining after 12 days of incubation, on PDMS (i) with induction and (ii) without induction, on G (iii) with induction and (iv) without induction, and on GO (v) with induction and (vi) without induction. Scale bars are 200 μm. (b) Quantification demonstrated a significantly higher amount of Alizarin Red staining in the MSCs differentiated on G (*p<0.05; n=4 for each group).

Spectrophotometric quantification confirmed these observations, with significantly higher absorbance at 450 nm (λ_{max}) for MSCs on G as compared to that on GO and PDMS (p<0.05). This represents a 7-fold increase in the extent of mineralization in the MSCs cultured on G compared to the identical culture conditions for those cultured on PDMS. Using ultraviolet spectrophotometry, the loading capacities of the G, GO, and PDMS for the various osteogenic chemical inducers were determined. From the adsorption isotherms obtained (Fig. 7.8), it was found that G adsorbed the highest amount of dexamethasone (400 mg) and β-glyverolphosphate (8g) per gram of G after 1 day of incubation.

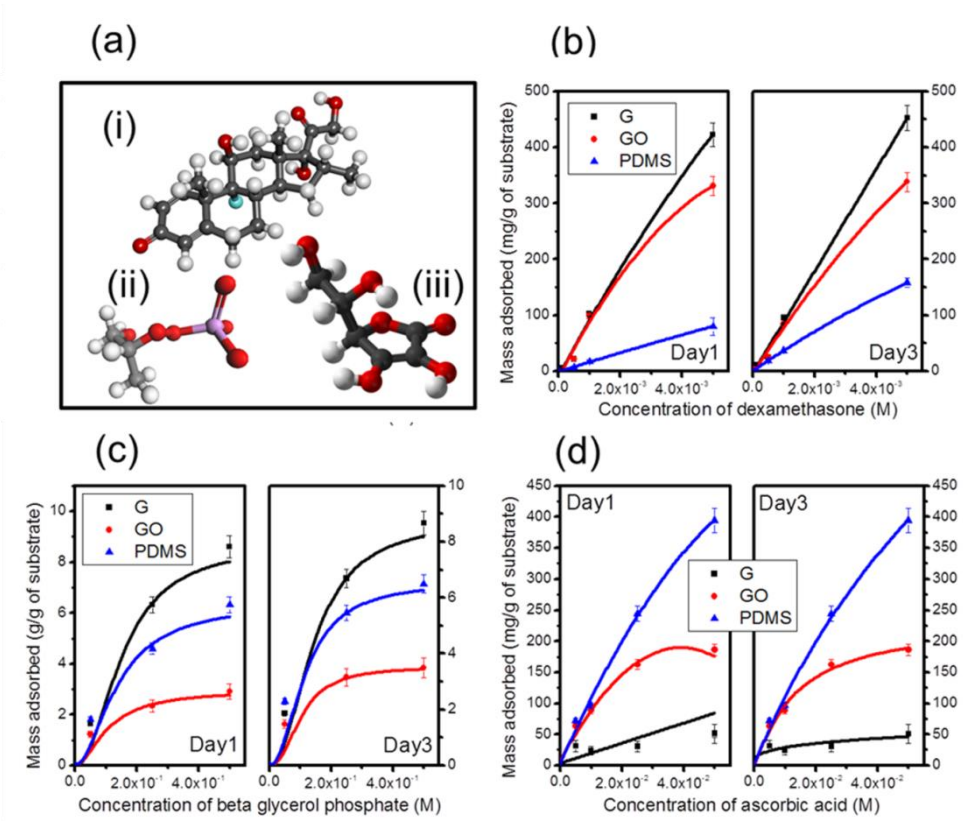

Figure 7.8 (a) Three-dimensional chemical structure of (i) dexamethasone, (ii) beta-glycerol phosphate and (iii) ascorbic acid and loading capacity of (i), (ii), and (iii) in (b), (c), and (d), respectively, in osteogenic induction media on PDMS, G and GO.

Our experimental results indicated that MSCs cultured on G were more osteogenic and deposited more minerals under chemical induction compared to other subtrates. We found that G has the ability to preconcentrate dexamethasone and β-glyerolphosphate, which are typical osteogenic inducers. The exceptionally high adsorption capacity of G for dexamethasone can be attributed to π-π stacking between the aromatic rings in the biomolecules and the G basal plane. Dexamethasone is a synthetic glucocorticoid that is known to alter the expression levels of many proteins and enzymes required during bone differentiation[62-64]. Elevated levels of dexamethasone have been found to increase mineral deposition[65]. Therefore, the enhanced osteogenic differentiation of MSCs on G can be attributed to the increased local concentration of adsorbed dexamethasone. This echoes a previous study showing the extent of osteogenic differentiation is enhanced with increasing concentration of dexamethasone in solution, with a saturation limit on 1,000 nM, beyond which cell layers start to delaminate[65]. It is also worth noting that dexamethasone is not the sole chemical that is responsible for directing MSCs to osteogenic lineages. It has to act synergistically with β-glyerolphosphate along with intracellular alkaline phosphatase enzyme to synthesize new mineralized bone matrices. From the adsorption isotherms of β-glyerolphosphate obtained, G also has the highest loading capacity followed by PDMS and GO. GO, which possesses a high density of oxygen functionalities, will experience larger electrostatic repulsion from the phosphate ions compared to G and PDMS. On the other hand, the differential adsorption of ascorbic acid on these platforms (Fig. 7.8d) can be rationalized by the degree of hydrogen bonding that is formed between the –OH moieties

of the acid and the substrates. Since G has no available groups to participate in H-bonding, it adsorbs the least amount of ascorbic acid compared to GO and PDMS. PDMS has more polar groups than GO and shows a greater degree of H-binding with ascorbic acid. Although the adsorption of ascorbic acid on G is not as high compared to GO and PDMS, it has been reported that ascorbic acid was found to affect mainly postdifferentiated, mature osteoblasts[66].

It is noteworthy that G affords accelerated differentiation of MSCs towards osteogenic differentiation. Typically, chemically induced osteogenic differentiation on polystyrene tissue culture dishes takes 21 days to complete[4]. In this case, by day 12, the MSCs on G already exhibited extensive mineralization, which points to the unique capability of G to act as a preconcentrating platform for accelerated bone differentiation. Besides considering the chemical interactions between the substrates and soluble factors involved in osteogenic specification, we consider whether the mechanical properties of the substrates have a significant role in influencing the fate of the stem cell. It has been reported by Engler *et al.* that stiff substrates (>100 kPa) promote bone differentiation[2]. However, since the elasticity of G, GO, and PDMS (1:10) were found to be in the same order of magnitude (~3-7 MPa), this suggests that the differences in cell differentiation were unlikely to be due to substrate stiffness. For example, the elastic modulus of G measured on silicon is approximately 600 MPa, which is 2 orders higher than on PDMS (refer to Fig. 7.4e). Therefore, stiffness is not a differentiating factor in this case since the stiffness is dominated by the substrate supporting G.

It is well-established that when stem cells are subjected to physical stresses exerted by topographic features on the substrate, stem cell differentiation into specific cell lineages can be enhanced[2,67-69]. Dalby *et al*[3] reported that MSCs cultured on randomized poly(methylmethacrylate) nanopatterns exhibited MSC osteoblastic morphologies after 21 days of incubation in standard cell culture media in the absence of chemical inducers. Although we cannot rule out the possibility that the corrugated structure of G, arising from its surface ripples and folds, can have some role in mediating osteogenesis, the fact that extensive mineralization was observed only on MSCs cultured in osteogenic induction media suggests that the chemical binding effect of G toward the growth agent is the key in accelerating MSC bone differentiation.

7.3.2.4 Adipogenic differentiation

Adipogenic differentiation is usually observed at a high density of *ca.* 20,000 cells per cm^3 with supplements of dexamethasone (10^{-6} M), indomethacin (0.6×10^{-4} M) and insulin (4 μg/mL). The adipogenic differentiation rate of MSCs was determined specifically staining introcytoplasmic lipids with Oil Red O[70] and its amount quantified *in situ* (see methods). Figure 7.9 shows adipogenic differentiation of MSCs cultured on the different substrates investigated in this study.

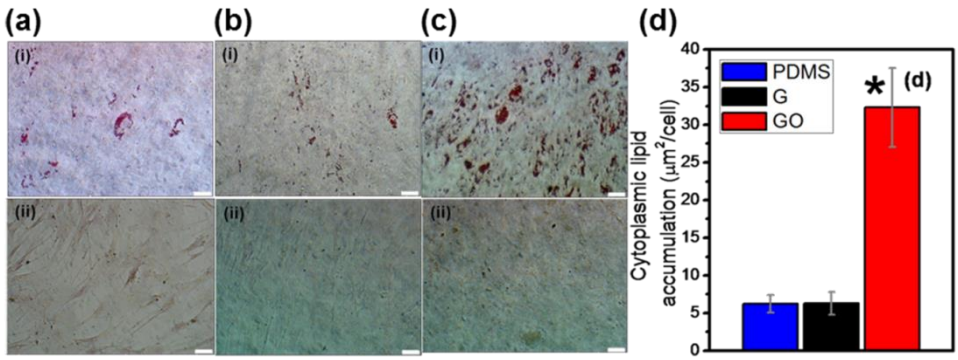

Figure 7.9 Extent of cytoplasmic lipid accumulation assessed by Oil Red O staining after 14 days of induction on (a) PDMS (i) with induction and (ii) without induction, on (b) G (i) with induction and (ii) without induction, and on (c) GO (i) with induction and (ii) without induction. Scale bars are 50 μm. (d) A higher propensity for adipogenic differentiation was observed for the MSCs differentiated on GO, with significantly larger amount of fat accumulation than the MSCs differentiation on G (b(i) and PDMS (a(i)) (*p<0.05; n=4 for each group). In negative controls without any adipogenic induction chemicals, no lipid deposits were observed.

Interestingly, the situation is reversed when MSCs were chemically induced to differentiate into adipocytes on G and GO. The results indicated that G suppressed adipogenesis with 6.29 μm^2/cell of lipid accumulation. While GO strongly enhanced adipogenesis with 32.3 μm^2/cell relative to MSCs differentiated on PDMS. It was noted that no lipid globules were detected on all three control, non-induced substrates. As insulin is the main mediator for fatty acid synthesis[71], we measured the adsorption isotherms of insulin on G and GO. Figure 7.6 shows that GO exhibited the highest adsorption capacity of ca. 4,800 mg of insulin per gram of GO as compared to 1,900 mg of insulin per gram of G and 1,580 mg of insulin per gram of PDMS. Since any alteration to the configuration of adsorbed insulin might interfere with its function to regulate fatty acid synthesis, the 3D conformation of the adsorbed insulin was investigated *via* circular dichroism (CD). Our measurements

revealed that the immobilized insulin on G was denatured, which can be judged from the attenuated negative absorption peaks at 209.0 and 222.0 nm, corresponding to the α-helix and β-pleated sheets, respectively at day 1 and 3 (see Fig 7.6d). To ascertain that any discrepancy observed in the absorption profile is not due to self-aggregation of insulin, its high tension voltage curves were recorded (Fig. 7.10).

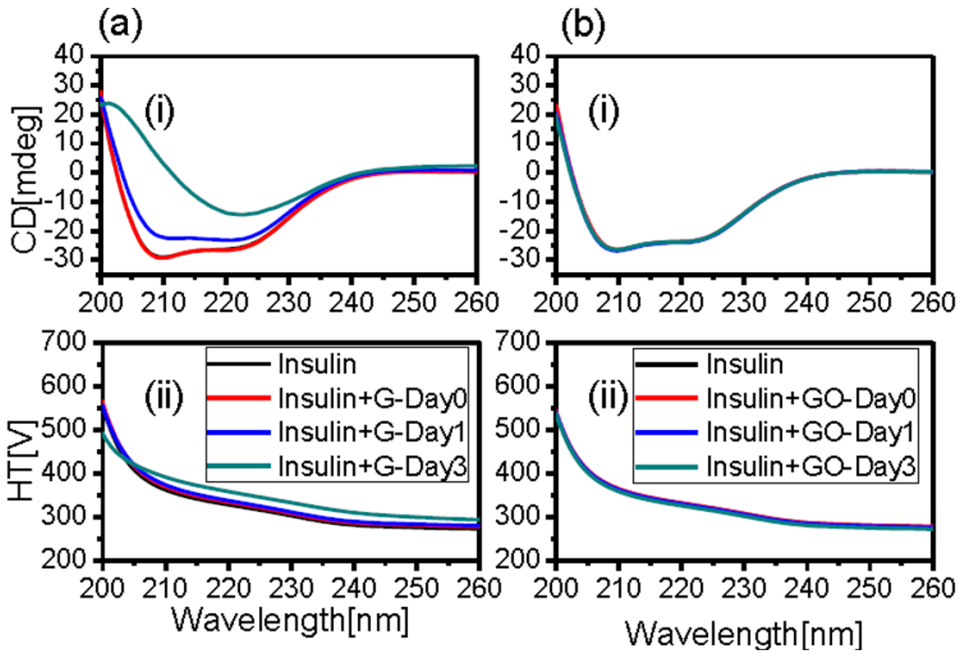

Figure 7.10 (a) Far UV absorption CD spectra of PBS (black), G in PBS (red), GO in PBS (blue) and Insulin in PBS (green) and (b) Far UV absorption CD spectra of (i) Insulin in PBS- Day 0 (black), Day1 (red) and Day3 (blue) and (ii) its corresponding high tension voltage spectra.

Upon incubation with G for one day, the peak representative of α-helix diminished by 13.4% and is unobservable by day 3, while the β-pleated sheets peak was found to decrease merely by 17.0%. From these data obtained, it can be concluded that denaturation of insulin occurs due to the unraveling of its α-

helix domains, while the effect on the β-pleated sheet component was less pronounced.

Adipogenesis is enhanced on GO due to its high affinity for insulin, which is the main mediator for fatty acid synthesis. The ability of GO to undergo H-bonding and electrostatic interactions enhances its binding capacity for insulin by more than twice compared to G on day3. This explains the occurrence of higher lipid accumulation for the MSCs differentiated on GO. Despite the higher affinity of GO for insulin, the electrostatic binding interaction with the protein allows the latter to maintain its three-dimensional conformation thereby enhancing adipogenic differentiation on GO. Since no fat globules were observed on the non-induced GO substrate, it is unlikely that adipogenesis is mediated by the substrate nanotopography alone. Although the adsorption of insulin on G is higher than on PDMS, less globules were observed (Fig. 7.9). This can be attributed to the denaturation of insulin brought about by strong π-π stacking on G. Our CD measurements revealed that the immobilized insulin on G was denatured, which is evident from changes in the negative absorption peaks of the α-helix at 209.0 nm and β-pleated sheets at 222.0 nm. Essentially, the different chemical structure of G and GO differentiates their binding interactions with biomolecules in terms of immobilization with or without denaturation.

7.4 Conclusion

This chapter demonstrates the potential of using diamond, graphene and its derivatives as supporting platforms for the enhanced growth and differentiation of human mesenchymal stem cells. Both intrinsic NCD and boron-doped NCD films enhanced the proliferation of human mesenchymal stem cells, increased their numbers relative to cells cultured on standard polystyrene dishes. The nanoroughness of the NCD films is believed to be responsible for these beneficial effects. In addition, the doped NCD substrate was found to enhance their differentiation towards the osteogenic cell phenotype, manifested by the increased concentration of osteocalcin, despite the absence of active electrical stimulation. It is believed that the electroactivity and surface electrical potential of these boron-doped NCD films are responsible for the above observation. It can be anticipated that the enhancement of differentiation of MSCs can be further enhanced by electrical stimulation through the electrically-conductive boron-doped films. In the later part of this chapter, we elucidated the origin of accelerated mesenchymal stem cell adhesion, proliferation, and differentiation on G and GO substrates. The origin of the osteogenic differentiation is traced to the ability of G to act as a preconcentration platform for osteogenic inducers, namely, dexamethasone and β-glycerolphosphate. We also demonstrate that insulin, which is a main mediator for fatty acid synthesis, is denatured upon adsorption on G through strong π-π interaction and unraveling of its three-dimensional configuration. Conversely, insulin is not denatured on GO, and its high affinity for insulin greatly enhances adipogenic differentiation. Therefore, besides the specific

binding interactions, the denaturation, or not, of the inducers is an important factor in determining the fate of the stem cell. It is highly possible that interactions with various chemical inducers could facilitate stem cell differentiation toward other lineages. The ability of NCD, G and GO to accelerate stem cell differentiate should find diverse applications in tissue engineering and regenerative medicine.

7.5 References

1 Meirelles, L., Chagastelles, P. C. & Nardi, N. B. Mesenchymal stem cells reside in virtually all post-natal organs and tissues. *Journal of Cell Science* **119**, 2204-2213 (2006).

2 Engler, A. J., Sen, S., Sweeney, H. L. & Discher, D. E. Matrix Elasticity Directs Stem Cell Lineage Specification. *Cell* **126**, 677-689 (2006).

3 Dalby, M. J. *et al.* The control of human mesenchymal cell differentiation using nanoscale symmetry and disorder. *Nature Materials* **6**, 997-1003 (2007).

4 Pittenger, M. F. *et al.* Multilineage potential of adult human mesenchymal stem cells. *Science* **284**, 143-147 (1999).

5 Treiser, M. D. *et al.* Cytoskeleton-based forecasting of stem cell lineage fates. *Proceedings of the National Academy of Sciences of the United States of America* **107**, 610-615 (2010).

6 Jung, D. R. *et al.* Topographical and physicochemical modification of material surface to enable patterning of living cells. *Critical Reviews in Biotechnology* **21**, 111-154 (2001).

7 Mahdavi, A. *et al.* A biodegradable and biocompatible gecko-inspired tissue adhesive. *Proceedings of the National Academy of Sciences of the United States of America* **105**, 2307-2312 (2008).

8 Li, W. J., Tuli, R., Huang, X., Laquerriere, P. & Tuan, R. S. Multilineage differentiation of human mesenchymal stem cells in a three-dimensional nanofibrous scaffold. *Biomaterials* **26**, 5158-5166 (2005).

9 Xin, X., Hussain, M. & Mao, J. J. Continuing differentiation of human mesenchymal stem cells and induced chondrogenic and osteogenic lineages in electrospun PLGA nanofiber scaffold. *Biomaterials* **28**, 316-325 (2007).

10 Mooney, E., Dockery, P., Greiser, U., Murphy, M. & Barron, V. Carbon nanotubes and mesenchymal stem cells: Biocompatibility, proliferation and differentiation. *Nano Letters* **8**, 2137-2143 (2008).

11 Yi, C., Liu, D., Fong, C. C., Zhang, J. & Yang, M. Gold nanoparticles promote osteogenic differentiation of mesenchymal stem cells through p38 MAPK pathway. *ACS Nano* **4**, 6439-6448 (2010).

12 Grausova, L. *et al.* Bone and vascular endothelial cells in cultures on nanocrystalline diamond films. *Diamond and Related Materials* **17**, 1405-1409 (2008).

13 Kromka, A. *et al.* Formation of continuous nanocrystalline diamond layers on glass and silicon at low temperatures. *Chemical Vapor Deposition* **14**, 181-186 (2008).

14 Narayan, R. J. *et al.* Microstructural and biological properties of nanocrystalline diamond coatings. *Diamond and Related Materials* **15**, 1935-1940 (2006).

15 Amaral, M., Abreu, C. S., Oliveira, F. J., Gomes, J. R. & Silva, R. F. Biotribological performance of NCD coated Si_3N_4-bioglass composites. *Diamond and Related Materials* **16**, 790-795 (2007).

16 Yang, W. *et al.* DNA-modified nanocrystalline diamond thin-films as stable, biologically active substrates. *Nature Materials* **1**, 253-257 (2002).

17 Wenmackers, S. *et al.* DNA attachment to nanocrystalline diamond films. *Physica Status Solidi (A) Applications and Materials Science* **202**, 2212-2216 (2005).

18 Härtl, A. *et al.* Protein-modified nanocrystalline diamond thin films for biosensor applications. *Nature Materials* **3**, 736-742 (2004).

19 Kloss, F. R. *et al.* The role of oxygen termination of nanocrystalline diamond on immobilisation of BMP-2 and subsequent bone formation. *Biomaterials* **29**, 2433-2442 (2008).

20 Ang, P. K., Loh, K. P., Wohland, T., Nesladek, M. & Van Hove, E. Supported lipid bilayer on nanocrystalline diamond: Dual optical and field-effect sensor for membrane disruption. *Advanced Functional Materials* **19**, 109-116 (2009).

21 Huang, H., Pierstorff, E., Osawa, E. & Ho, D. Protein-mediated assembly of nanodiamond hydrogels into a biocompatible and biofunctional multilayer nanofilm. *ACS Nano* **2**, 203-212 (2008).

22 Papo, M. J., Catledge, S. A., Vohra, Y. K. & Machado, C. Mechanical wear behavior of nanocrystalline and multilayer diamond coatings on temporomandibular joint implants. *Journal of Materials Science: Materials in Medicine* **15**, 773-777 (2004).

23 Lappalainen, R., Selenius, M., Anttila, A., Konttinen, Y. T. & Santavirta, S. S. Reduction of Wear in Total Hip Replacement Prostheses by Amorphous Diamond Coatings. *Journal of Biomedical Materials Research - Part B Applied Biomaterials* **66**, 410-413 (2003).

24 Price, R. L., Ellison, K., Haberstroh, K. M. & Webster, T. J. Nanometer surface roughness increases select osteoblast adhesion on carbon nanofiber compacts. *Journal of Biomedical Materials Research - Part A* **70**, 129-138 (2004).

25 Specht, C. G., Williams, O. A., Jackman, R. B. & Schoepfer, R. Ordered growth of neurons on diamond. *Biomaterials* **25**, 4073-4078 (2004).

26 Liu, H., Slamovich, E. B. & Webster, T. J. Increased osteoblast functions among nanophase titania/poly(lactide-co- glycolide) composites of the highest nanometer surface roughness. *Journal of Biomedical Materials Research - Part A* **78**, 798-807 (2006).

27 Heitz, J. *et al.* Cell Adhesion on polytetrafluoroethylene modified by UV-irradiation in an ammonia atmosphere. *Journal of Biomedical Materials Research - Part A* **67**, 130-137 (2003).

28 Liu, L., Chen, S., Giachelli, C. M., Ratner, B. D. & Jiang, S. Controlling osteopontin orientation on surfaces to modulate endothelial cell adhesion. *Journal of Biomedical Materials Research - Part A* **74**, 23-31 (2005).

29 Lesný, P. *et al.* Macroporous hydrogels based on 2-hydroxyethyl methacrylate. Part 4: Growth of rat bone marrow stromal cells in three-dimensional hydrogels with positive and negative surface charges and in polyelectrolyte complexes. *Journal of Materials Science: Materials in Medicine* **17**, 829-833 (2006).

30 Dadsetan, M. *et al.* The effects of fixed electrical charge on chondrocyte behavior. *Acta Biomaterialia* **7**, 2080-2090 (2011).

31 Gajewski, W. *et al.* Electronic and optical properties of boron-doped nanocrystalline diamond films. *Physical Review B - Condensed Matter and Materials Physics* **79** (2009).

32 Kalbacova, M., Broz, A., Kong, J. & Kalbac, M. Graphene substrates promote adherence of human osteoblasts and mesenchymal stromal cells. *Carbon* **48**, 4323-4329 (2010).

33 Nayak, T. R. *et al.* Graphene for controlled and accelerated osteogenic differentiation of human mesenchymal stem cells. *ACS Nano* **5**, 4670-4678 (2011).

34 Williams, O. A., Nesládek, M., Mareš, J. J. & Hubík, P. in *Physics and Applications of CVD Diamond* 13-27 (Wiley-VCH Verlag GmbH & Co. KGaA, 2008).

35 Nesládek, M. *et al.* Superconductive B-doped nanocrystalline diamond thin films: Electrical transport and Raman spectra. *Applied Physics Letters* **88** 232111 (2006).

36 Wang, Y., Tong, S. W., Xu, X. F., Özyilmaz, B. & Loh, K. P. Interface engineering of layer-by-layer stacked graphene anodes for high-performance organic solar cells. *Advanced Materials* **23**, 1514-1518 (2011).

37 Hummers Jr, W. S. & Offeman, R. E. Preparation of graphitic oxide. *Journal of the American Chemical Society* **80**, 1339 (1958).

38 Liu, Z., Robinson, J. T., Sun, X. & Dai, H. PEGylated nanographene oxide for delivery of water-insoluble cancer drugs. *Journal of the American Chemical Society* **130**, 10876-10877 (2008).

39 Miller, D. C., Thapa, A., Haberstroh, K. M. & Webster, T. J. Endothelial and vascular smooth muscle cell function on poly(lactic-co-glycolic acid) with nano-structured surface features. *Biomaterials* **25**, 53-61 (2004).

40 Webster, T. J. & Ejiofor, J. U. Increased osteoblast adhesion on nanophase metals: Ti, Ti6Al4V, and CoCrMo. *Biomaterials* **25**, 4731-4739 (2004).

41 Švorčík, V. *et al.* Cytocompatibility of Ar+ plasma treated and Au nanoparticle-grafted PE. *Nuclear Instruments and Methods in Physics Research, Section B: Beam Interactions with Materials and Atoms* **267**, 1904-1910 (2009).

42 Grinevich, A. *et al.* Nanocomposite Ti/hydrocarbon plasma polymer films from reactive magnetron sputtering as growth support for

osteoblast-like and endothelial cells. *Journal of Biomedical Materials Research - Part A* **88**, 952-966 (2009).

43 Švorčík, V. *et al.* Surface properties and biocompatibility of ion-implanted polymers. *Journal of Materials Chemistry* **5**, 27-30 (1995).

44 Kopecek, M. *et al.* Improved adhesion, growth and maturation of human bone-derived cells on nanocrystalline diamond films. *Physica Status Solidi (A) Applications and Materials Science* **205**, 2146-2153 (2008).

45 Grausova, L. *et al.* Enhanced growth and osteogenic differentiation of human osteoblast-like cells on boron-doped nanocrystalline diamond thin films. *PLoS ONE* **6** (2011).

46 Bettinger, C. J., Bruggeman, J. P., Misra, A., Borenstein, J. T. & Langer, R. Biocompatibility of biodegradable semiconducting melanin films for nerve tissue engineering. *Biomaterials* **30**, 3050-3057 (2009).

47 Jeong, S. I. *et al.* Development of electroactive and elastic nanofibers that contain polyaniline and poly(L-lactide-co-ε-caprolactone) for the control of cell adhesion. *Macromolecular Bioscience* **8**, 627-637 (2008).

48 Jun, I., Jeong, S. & Shin, H. The stimulation of myoblast differentiation by electrically conductive sub-micron fibers. *Biomaterials* **30**, 2038-2047 (2009).

49 Mihardja, S. S., Sievers, R. E. & Lee, R. J. The effect of polypyrrole on arteriogenesis in an acute rat infarct model. *Biomaterials* **29**, 4205-4210 (2008).

50 Shi, G., Zhang, Z. & Rouabhia, M. The regulation of cell functions electrically using biodegradable polypyrrole-polylactide conductors. *Biomaterials* **29**, 3792-3798 (2008).

51 Verdejo, R. *et al.* Reactive polyurethane carbon nanotube foams and their interactions with osteoblasts. *Journal of Biomedical Materials Research - Part A* **88**, 65-73 (2009).

52 Schmidt, C. E., Shastri, V. R., Vacanti, J. P. & Langer, R. Stimulation of neurite outgrowth using an electrically conducting polymer. *Proceedings of the National Academy of Sciences of the United States of America* **94**, 8948-8953 (1997).

53 Gomez, N. & Schmidt, C. E. Nerve growth factor-immobilized polypyrrole: Bioactive electrically conducting polymer for enhanced neurite extension. *Journal of Biomedical Materials Research - Part A* **81**, 135-149 (2007).

54 Khang, D., Park, G. E. & Webster, T. J. Enhanced chondrocyte densities on carbon nanotube composites: The combined role of nanosurface roughness and electrical stimulation. *Journal of Biomedical Materials Research - Part A* **86**, 253-260 (2008).

55 Shi, G., Rouabhia, M., Meng, S. & Zhang, Z. Electrical stimulation enhances viability of human cutaneous fibroblasts on conductive biodegradable substrates. *Journal of Biomedical Materials Research - Part A* **84**, 1026-1037 (2008).

56 Li, X. *et al.* Large-area synthesis of high-quality and uniform graphene films on copper foils. *Science* **324**, 1312-1314 (2009).

57 Stankovich, S. *et al.* Synthesis of graphene-based nanosheets via chemical reduction of exfoliated graphite oxide. *Carbon* **45**, 1558-1565 (2007).

58 Tang, L. A. L., Wang, J. & Loh, K. P. Graphene-based SELDI probe with ultrahigh extraction and sensitivity for DNA oligomer. *Journal of the American Chemical Society* **132**, 10976-10977 (2010).

59 Oh, S. *et al.* Stem cell fate dictated solely by altered nanotube dimension. *Proceedings of the National Academy of Sciences of the United States of America* **106**, 2130-2135 (2009).

60 Phillips, K. S. & Cheng, Q. Assembly and characterization of protein resistant planar bilayers in PDMS microfluidic devices. *Material Research Society Symposium Proceedings* **774**, O7.2.1-O7.2.8 (2003).

61 Sapsford, K. E. & Ligler, F. S. Real-time analysis of protein adsorption to a variety of thin films. *Biosensors and Bioelectronics* **19**, 1045-1055 (2004).

62 Haynesworth, S. E., Goshima, J., Goldberg, V. M. & Caplan, A. I. Characterization of cells with osteogenic potential from human marrow. *Bone* **13**, 81-88 (1992).

63 Oshina, H. *et al.* Effects of continuous dexamethasone treatment on differentiation capabilities of bone marrow-derived mesenchymal cells. *Bone* **41**, 575-583 (2007).

64 Scutt, A., Bertram, P. & Bräutigam, M. The role of glucocorticoids and prostaglandin E2 in the recruitment of bone marrow mesenchymal cells to the osteoblastic lineage: Positive and negative effects. *Calcified Tissue International* **59**, 154-162 (1996).

65 Jaiswal, N., Haynesworth, S. E., Caplan, A. I. & Bruder, S. P. Osteogenic differentiation of purified, culture-expanded human mesenchymal stem cells in vitro. *Journal of Cellular Biochemistry* **64**, 295-312 (1997).

66 Quarles, L. D., Yohay, D. A., Lever, L. W., Caton, R. & Wenstrup, R. J. Distinct Proliferative and Differentiated Stages of Murine MC3T3-El Cells in Culture: An In Vitro Model of Osteoblast Development. *Journal of Bone and Mineral Research* **7**, 683-692 (1992).

67 Altman, G. H. *et al.* Cell differentiation by mechanical stress. *The FASEB journal : official publication of the Federation of American Societies for Experimental Biology* **16**, 270-272 (2002).

68 Dalby, M. J. *et al.* Osteoprogenitor response to semi-ordered and random nanotopographies. *Biomaterials* **27**, 2980-2987 (2006).

69 Yamamoto, K. *et al.* Fluid shear stress induces differentiation of Flk-1-positive embryonic stem cells into vascular endothelial cells in vitro. *American Journal of Physiology - Heart and Circulatory Physiology* **288**, H1915-H1924 (2005).

70 Liu, D., Yi, C., Zhang, D., Zhang, J. & Yang, M. Inhibition of proliferation and differentiation of mesenchymal stem cells by carboxylated carbon nanotubes. *ACS Nano* **4**, 2185-2195 (2010).

71 Hauner, H., Schmid, P. & Pfeiffer, E. F. Glucocorticoids and insulin promote the differentiation of human adipocyte precursor cells into fat cells. *Journal of Clinical Endocrinology and Metabolism* **64**, 832-835 (1987).

Chapter 8

Conclusions

8.1 Uniqueness of the graphene-diamond interface

Owing to their unique properties, both graphene and diamond are attractive materials in various technological applications. By fusing the metallic-sp^2 and dielectric-sp^3 graphene-diamond interface, new functionalities are created. This graphene-diamond hybrid material has potential in a wide range of applications spanning from electronics to energy conversion and regenerative medicine.

8.2 Summary and outlook

Motivated by the superlative properties of graphene and diamond, this thesis has explored and demonstrated novel chemistry and physics by interfacing two different carbon phases.

Firstly, charge transport in graphene was observed to be modulated by a change in the surface termination of diamond. Diamond was used as a novel substrate to evaluate the importance of charged impurities in influencing the carrier mobility of CVD graphene. We observed a weaker high temperature

metallic behavior ($d\rho/dT > 0$) of graphene on oxygen-terminated devices relative to devices built on conventional SiO_x, which can be attributed to the higher surface phonon energy of diamond (155 meV relative to 59 meV of SiO_x). This work highlights the importance of underlying substrate in affecting the charge transport property of graphene. By changing the surface terminations of diamond, large modulation of the carrier mobilities of graphene was observed. In Chapter 4 of the thesis, a graphene-diamond electrode was constructed by coupling exfoliated graphene to boron-doped diamond (BDD) via a molecular wire to enable efficient charge transfer. Due to the improved conductivity and well-matched energetics of the hybrid electrode with the photoactive layer, a 5 times increase in the photocurrent density was observed. The results pave the way for using graphene to modify surface and optimize CVD diamond electrodes for optoelectronic applications.

Chemical hybridization of graphene and diamond by high temperature annealing was performed to fuse graphene bubbles on diamond, such that strong interfacial bonding and impermeability of graphene enabled the construction of a hydrothermal graphene-diamond anvil cell. We demonstrated the first example of using an impermeable atomic membrane for trapping fluids at supercritical conditions, where the power of superheated water in corroding diamond was observed. The technological implication of the present work extends to supercritical fluid assisted etching of solid surfaces as well as new types of high pressure anvil cell using graphene membrane. Due to the transparency and high thermal conductivity of graphene, it can serve as an optical window for laser-assisted etching where exponential increase in etch rates can be brought about by the synergistic effects of photo-excitation and

ultrahigh pressure. Finally, the encapsulation of fluids between graphene bubbles and diamond allow fluids to be probed spectroscopically using a wide range of radiation from X-ray, to infrared light to gamma rays. To test the applicability of graphene nanobubbles grown on diamond as high pressure anvil cells, we encapsulated pressure-sensitive molecules in the bubbles in order to observe high pressure (GPa)-induced conformational changes and cycloaddition reactions in Chapter 6. The nanobubbles that form as a result of thermally induced bonding of graphene and diamond at the interface are highly impermeable and function well as optically transparent, pressurized nanoreactors, which allow high-pressure and high-temperature chemical reactions in fluids to be probed dynamically using vibrational spectroscopy. By monitoring the conformational changes of pressure-sensitive molecules, the pressure within the nanobubble could be tracked as a function of temperature. The polymerization of buckministerfullerene (C_{60}), which is symmetrically forbidden under ambient conditions, was observed to proceed in well-defined stages in the pressurized nanobubble.

Finally, owing to the biocompatibility of these carbon materials, they were explored as biomimetic platforms for cell growth and differentiation. The potential of using nanocrystalline diamond and graphene as supporting platforms for enhanced growth and differentiation of human mesenchymal stem cells were demonstrated. Enhanced stem cell growth and differentiation were observed on these carbon materials, thus showing their potential in tissue engineering and regenerative medicine.